Alma Mater Studiorum · Università di Bologna

SCUOLA DI SCIENZE

Astrofisica e Cosmologia

Simulating Mock Observations for Weak Lensing Analysis and Galaxy Clusters Mass Estimates

TESI di LAUREA MAGISTRALE

Relatore:
Chiar.mo Prof.
Massimo Meneghetti

Presentata da:
Riccardo Seppi

Settembre
2018-2019

A mia sorella Federica,
ai miei genitori Rosella e Angelo,
ai miei nonni Angelina e Adriano,
Marisa e Roberto che controllano da lassù
grazie infinite per il continuo supporto nella vita

ALMA MATER STUDIORUM - UNIVERSITÀ DI BOLOGNA

Scuola di Scienze

Corso di Laurea Magistrale in Astrofisica e Cosmologia

Simulating Mock Observations for Weak Lensing Analysis and Galaxy Clusters Mass Estimates

Seppi Riccardo

ABSTRACT

The purpose of this thesis is learning how to accomplish a weak lensing analysis and estimate the mass of a galaxy cluster. For this task, I performed simulations in order to obtain mock observations with the Subaru Telescope of galaxies distorted by a massive galaxy cluster. Their distortion was quantified according to the Kaiser-Squires-Broadhurst (KSB) method.

Chapter 1 is an introduction to crucial concepts regarding this thesis, in the fields of cosmology, galaxy clusters and gravitational lensing.

Chapter 2 discusses the process of the simulation, its inputs and outputs and the analysis of the distortion of galaxy shapes.

Chapter 3 regards the results of the analysis on the real galaxy cluster MACS J1206, the comparison with its model and how to get its mass by means of a fit with a Navarro-Frenk-White (NFW) mass distribution.

Chapter 4 reports the application of the same analysis to MACS J1206 observed in different filters and two simulated clusters: Ares and Hera.

Chapter 5 sums up the key points of the whole work.

Acknowledgements

I would like to use these lines to thank my supervisor Massimo Meneghetti, whose help has simply been fundamental throughout these months and without whom this work would not have been possible. I also want to thank Mario Radovich (INAF - Astronomical Observatory of Padova), who kindly helped me with the KSB algorithm with long explanations and emails, and Lauro Moscardini, who advised me in the preparation of the first chapter.

Contents

Contents **5**

1 Introduction **7**

1.1 Describing the Universe 7

1.1.1 Expanding Universe 8

1.1.2 Measure distances 9

1.2 Structure Formation 10

1.2.1 Inflation 11

1.2.2 Jeans theory 13

1.2.3 Growth of Perturbations 16

1.3 Galaxy clusters 21

1.3.1 Clusters in Cosmology 23

1.3.2 Sunyaev – Zel'dovich Effect 26

1.4 Gravitational Lensing 27

1.4.1 Deflection angle 27

1.4.2 Basics of Lensing 31

1.4.3 Distortion and Magnification 33

1.4.4 Power Law Lenses 37

1.4.5 Microlensing 39

1.4.6 Lensing by galaxy clusters 40

2 Methodology of the analysis **49**

2.1 Simulations with Skylens 49

2.1.1 Input file 52

2.1.2 Deflector 54

2.1.3 Simulation 54

2.2 KSB method 57

2.2.1 Object selection 61

2.3 Code testing 63

3 Data Elaboration **67**
3.1 MACS J1206 67
3.1.1 MACS J1206 in the R_C band 72
3.2 KSB implementation 76
3.2.1 Sextractor 76
3.2.2 Ellipticity analysis 79
3.3 Catalog analysis 79
3.3.1 Lenstool Model 84
3.4 Cluster Mass Estimate 88
3.4.1 Theoretic approach 88
3.4.2 Mass values 93

4 Additional clusters **97**
4.1 MACS J1206 - Z and I_C bands 97
4.2 Simulated Clusters 99
4.2.1 Ares 99
4.2.2 Hera 104
4.2.3 ICL 107

5 Conclusions **111**

Bibliography **115**

Bibliografy **115**

Chapter 1

Introduction

This chapter is meant as an introduction to crucial astrophysical fields closely related to the work involved in this thesis.

1.1 Describing the Universe

The best theory we have to understand the universe on its biggest scales is the theory of General Relativity, formulated by Einstein in 1915 [1]. It is based on the geometrical concept that mass and energy bend space-time and space-time tells matter and energy how to move and behave. This idea is reflected by Einstein's field equation

$$R_{\mu\nu} - \frac{1}{2}Rg_{\mu\nu} = \frac{8\pi G}{c^4}T_{\mu\nu} + \Lambda g_{\mu\nu} \tag{1.1}$$

where the Ricci tensor $R_{\mu\nu}$ and scalar R are basically a measure of the curvature of space-time, $g_{\mu\nu}$ is the metric that describes it, $T_{\mu\nu}$ is the mass-energy tensor and Λ is the cosmological constant. Note that in a modern view, on the left hand side of equation 1.1 there are only geometrical factors, which describe space-time configuration, while on the right hand side there are the sources: mass, energy and the cosmological constant, nowadays viewed as Dark Energy. In an alternative approach of modified gravity this last term would be on the left side of the equation. Solving this equation means finding the metric $g_{\mu\nu}$, which tells how the four space-time coordinates are related.
On large scales, let's say hundreds of Mega-Parsecs, the Universe seems to be homogeneous and isotropic: this is known as the *Cosmological Principle*. Under this assumption, the metric can be written as

$$dS^2 \;=\; c^2dt^2 - a^2(t)\Big[\frac{dr^2}{1-Kr^2} + r^2(d\theta^2 + sin^2(\theta)d\phi^2)\Big] \tag{1.2}$$

which is known as the Friedmann Roberson Walker (FRW) metric [2], $a(t)$ is the scale factor of the universe: the scaling of space coordinates is a function of this time dependent scale factor; k is a factor that describes the geometry of the universe and can assume three values: +1, 0, -1, which are associated respectively with a spherical, flat and hyperbolic geometry. These values translate to different types of spaces respectively: closed, flat and open, depending on the overall mass density of the universe. Recent measures of the *Cosmic Microwave Background* **CMB** from the Planck Collaboration confirm that our universe is flat.

1.1.1 Expanding Universe

One of the most interesting known facts about the universe is that it is expanding. The first evidence was brought to light by Edwin Hubble in 1929 [3], when he observed that spectra from distant galaxies were redshifted, meaning that known spectral lines were found found at redder wavelengths. This is quantified by the quantity

$$z \;=\; \frac{\lambda_o - \lambda_e}{\lambda_e} \tag{1.3}$$

where λ_e is the wavelength of a photon when it is emitted and λ_o is the observed wavelength. In the context of a universe described by the FRW metric, it is possible to link redshift to the expansion factor, as

$$1 \;+\; z \;=\; \frac{\lambda_o}{\lambda_e} \;=\; \frac{a(t_o)}{a(t_e)} \tag{1.4}$$

Hubble observed longer wavelengths with respect to the emitted ones, which means that $a(t_o) > a(t_e)$, i.e. the universe is expanding. He linked this phenomenon to a relative velocity of far sources, which increases with their distance from the observer. This is expressed by the famous *Hubble-Lemaitre* law

$$v_r \;=\; H(t)d_{pr}(t) \tag{1.5}$$

where $H(t) = \frac{\dot{a}}{a}$ is called Hubble's parameter and $d_{pr} = \int_0^r a(t)\frac{dr'}{(1-kr'^2)^{1/2}}$ is the proper distance.
So redshift is a crucial feature of our universe and yields that it is expanding. Moreover, nowadays we know that not only it is expanding, but the expansion is accelerated. In fact, it is possible to write the scale factor as a series expansion

$$a(t) = a_0\Big[1 + H_0(t-t_0) - \frac{q_0}{2}H_0^2(t-t_0)^2\Big] \tag{1.6}$$

where $q = -\frac{\ddot{a}a}{\dot{a}^2}$ is called the *deceleration parameter*. The magnitude of distant exploding Supernovae Ia depends on this parameter and observations of this type of stars yields $q < 0$ [4], meaning that the universe is expanding and is also accelerating while doing so.

1.1.2 Measure distances

There are different approaches to measure distances in cosmology. The most intuitive in this context, is the **proper distance**, introduced in the Hubble's law 1.5. It derives directly from the FRW metric, since it is basically the space distance between two points at a fixed time, it is the result of integrating 1.2 with $dt = d\theta = d\phi = 0$. Note that the integral does not depend on time, so that it is possible to write

$$\begin{aligned} d_{pr} &= a(t)f(r) \\ f(r) &= \int_0^r \frac{dr'}{\sqrt{1-kr'^2}} \end{aligned} \tag{1.7}$$

Similarly, it is possible to consider the so called **comoving distance**, which is the proper distance measured today, which is simply the proper distance at a certain time multiplied by the variation of the scale factor from that instant to today.

$$\begin{aligned} d_c &= a(t_0)f(r) \\ d_c &= \frac{a_0}{a(t)}d_{pr}(t) \end{aligned} \tag{1.8}$$

The problem is that this type of distances are not directly measurable: it would be necessary to have a picture of the universe containing the

points between which we want to measure the distance at a specific time. This is not doable. Nonetheless, it possible to define other types of measurable distances.

- *Luminosity distance*: this definition aims at conserving the typical definitions of luminosity and flux, so that $f = \frac{L}{4\pi d_L^2}$. But there are different factors to consider between the emission of a photon and its detection: the universe is expanding, so photons are redshifted and there is time dilation between their emission interval and their detection interval. Moreover, they will be seen under a bigger surface, because of expansion. There factors imply the definition of luminosity distance for photons that propagate in a FRW metric of

$$\begin{aligned} f &= \frac{\delta t_1}{\delta t_0}\frac{a(t_1)}{a(t_0)}\frac{L}{4\pi a_0^2 r_1^2} \\ d_L &= a_0 r_1 (1+z) \end{aligned} \tag{1.9}$$

- *Angular Diameter Distance*: this definition of distance is based on the quotient between a dimension D of a certain object and the angle $\Delta\theta$ under which it is seen, so that $d_A = \frac{D}{\Delta\theta}$. Simply looking at the FRW metric and aligning the coordinates $dt = dr = d\phi = 0$, it is straightforward $dS = ard\theta$ and the definition of angular diameter distance becomes

$$d_A = ar \tag{1.10}$$

Note that these two distances are linked by the relation $d_A = \frac{d_L}{(1+z)^2}$, they are different and depend on the type of cosmology.

1.2 Structure Formation

The theory of structure formation is based on gravitational instabilities, that are the fundamental cornerstone of our description of today's universe. If there were no instabilities, the universe would still be homogeneous and isotropic, without any collapsed structure, and would be simply described by a Friedmann type evolution, according to Friedmann's equations, elaborated from the theory of General Relativity (GR) [5]

$$\ddot{a} = -\frac{4}{3}\pi G(\rho + \frac{3P}{c^2})a$$
$$\dot{a}^2 + Kc^2 = \frac{8}{3}\pi G\rho a^2 \tag{1.11}$$

which describe the behaviour of the scale factor in a universe where the cosmological principle holds.
Moreover, elaborating these equations leads to understand the relation between the mass density of the universe and its geometry. In fact, dividing the second equation for a_0 and considering the critical density parameter $\rho_c = \frac{3H^2(z)}{8\pi G}$, where $H(z)$ is the Hubble parameter at a certain redshift and G is Newton's gravitational constant, one obtains

$$H_0^2\left[1 - \frac{\rho_0}{\rho_{0,c}}\right] = -\frac{Kc^2}{a_0^2} \tag{1.12}$$

The critical density is equal to $\rho_c \sim 10^{-26}\frac{kg}{m^3} \sim 1.5 \times 10^{11}\frac{M_\odot}{Mpc^3}$.
From equation 1.12 three geometry scenarios are evident:

- $\rho_0 = \rho_{0,c}$: the universe if flat, $K = 0$
- $\rho_0 > \rho_{0,c}$: the universe if closed, $K = +1$
- $\rho_0 < \rho_{0,c}$: the universe if open, $K = -1$

Under these conditions the universe would have kept evolving according to its geometry, but without perturbations, which clearly is not what happened, since nowadays we see plenty of collapsed structures, resulting from the growth of initial instabilities.

1.2.1 Inflation

These instabilities are a direct consequence of inflation [6], a period of accelerated growth of the universe in its early stages. A complete description of the theory of inflation is beyond the scope of this thesis, the focal point is that it produces initial perturbations of the mean density in the universe.
The whole inflation solves different problems that arise from simple Friedmann evolution. The following analysis is based on P. Coles (2002) [7].

- Magnetic Monopolies: GUT transition theory predicts the existence of magnetic monopolies, but their density should be overwhelming, according to $\Omega_{MM} \geq \frac{m_{MM}}{m_p}\Omega_B$, where Ω indicates the density parameter, m_{MM} the mass linked to magnetic monopolies and m_p the mass of a proton. The final result is $\Omega_{MM} \geq 10^{16}\Omega_B$, meaning that the universe would be closed. However, CMB observations yield that the universe is flat.
  This is solved by inflation, that stretches space-time so much that the universe becomes flat and magnetic monopolies are diluted by such an amount that it is very hard to detect them.

- Cosmological horizon: nowadays the CMB emphasizes areas at the same temperature, which are so distant from one another to the point that causal connection exists on scales that are bigger than the horizon scale. In particular $R_H \sim 0.1 R_{LS}$ .This is clearly a paradox. Inflation solves this problem by considering the Hubble's comoving sphere, defined as $R_{H,C} = \frac{a_0}{a}R_H$, where a refers to the scale factor.
  Inflation works in such a way that $\frac{a_0}{a}$ drops faster than the growth of the Hubble sphere, as Figure 1.1.

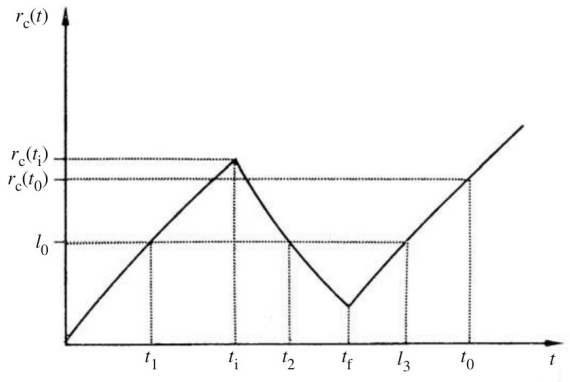

Figure 1.1: Hubble comoving sphere $R_{H,C}$ as a function of time

Inflation begins at t_i and ends at t_f. Note that horizon problem is simply solved if $R_{H,C}(t_i) \geq R_{H,C}(t_0)$, which means that there was a time when the comoving horizon was bigger than today, which explains the causal connection paradox.

- Flat Universe: geometry of the universe can be linked to its total

density parameter Ω. According to

$$\Omega^{-1}(z) - 1 = \frac{1}{(1+z)^{1+3w}} \left[\Omega_0^{-1} - 1\right]$$

if the universe has a certain type of geometry, either flat, closed or open, it keeps that geometry throughout its evolution.
In particular, if $\Omega = 1$, the universe is flat, if $\Omega \geq 1$ it is closed, while if $\Omega \leq 1$ it is open. It seems to be very strange that only one value gives a flat universe, which is what is observed! It is a fine tuning problem.
Inflation brings Ω towards 1 between t_i and t_f and after that the expansion goes back to Friedmann evolution, as Figure 1.2 shows.

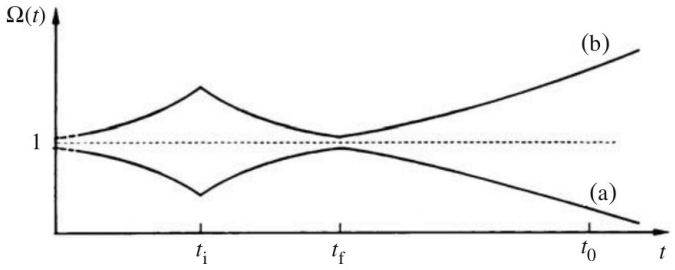

Figure 1.2: Evolution of the density parameter

However, inflation stretches the universe so much that it gets flat even if it was closed or open before, so that every initial geometric condition is brought towards flatness.

There are multiple inflation models, but most of them are based on the decay of a scalar field, called inflaton. This decay signals the end of the inflationary era and produces the actual initial perturbations of the density field, whose order of magnitude is $\frac{\Delta\rho}{\rho} \sim 10^{-5}$. These perturbations have to grow to $\frac{\Delta\rho}{\rho} \sim 10^2 - 10^3$, which are the values measured at the present day.

1.2.2 Jeans theory

The simplest way of treating gravitational collapse is using Jeans theory (1902) [8]. An easy introduction of this concept is calculating the scale which distinguishes between expansion and collapse of a spherical

structure of mass M and radius R, by considering its energetic balance. Elaborating equation

$$\frac{Mv^2}{2} \propto \frac{GM^2}{R}$$

where v is a typical speed of the particles contained in the structure, it is possible to obtain

$$R_J \propto v\sqrt{\frac{1}{G\rho}}$$

where ρ is the mass density. This is the so called Jeans scale: if a typical scale is bigger than this limit, the gravitational energy term will overpower the kinetic term, which leads to a collapse. On the other hand, if a scale is below this limit, the structure will flake of.
It is possible to deduce R_J formally, from a mathematical standpoint. Let's consider the universe as a collisional gas in a static background at first. Under this assumption, it is described by typical fluid equations of motion.

$$\begin{aligned} \frac{\partial \rho}{\partial t} + \nabla \cdot \rho \mathbf{v} &= 0 \\ \frac{\partial \mathbf{v}}{\partial t} + (\mathbf{v} \cdot \nabla)\mathbf{v} + \frac{1}{\rho}\nabla P + \nabla \Phi &= 0 \\ \nabla^2 \Phi - 4\pi G\rho &= 0 \end{aligned} \tag{1.13}$$

which are the continuity equation, the Euler equation and the Poisson equation.
It is also necessary to consider an equation of state $P = P(\rho, S)$ and a function describing entropy $f = \frac{\partial S}{\partial t}$. In the case of adiabatic perturbations, entropy is constant, so that $P = P(\rho)$ and $f = 0$.
A static background yields a specific set of initial conditions for density, pressure, gravitational potential and velocity fields: $\rho = \rho_b,\ P = P_b,\ \Phi = \Phi_b,\ \mathbf{v} = 0$. Note that this is not a suitable solution of system 1.13, in fact if both density and potential are constant, the Poisson equation is not solved. This is an incongruity that will be solved considering an expanding universe.
Let's look for a solution involving initial perturbations, so that the initial conditions become: $\rho = \rho_b + \delta\rho,\ P = P_b + \delta P,\ \Phi = \Phi_b + \delta\Phi,\ \mathbf{v} = \delta\mathbf{v}$.
Substituting these fields in system 1.13 and considering only first order

terms of perturbations, it is possible to obtain a set of equations that these small quantities have to solve.

$$\begin{aligned} &\frac{\partial \delta\rho}{\partial t} + \rho_b \nabla \cdot \delta\mathbf{v} = 0 \\ &\frac{\partial \delta\mathbf{v}}{\partial t} = -\frac{v_s^2}{\rho_b}\nabla\delta\rho - \nabla\delta\Phi \\ &\nabla^2\delta\Phi - 4\pi G\delta\rho = 0 \end{aligned} \tag{1.14}$$

where $v_s^2 = \dfrac{\partial P}{\partial \rho}$ is the speed of sound, which allows to hide the pressure term and reduce the system to three variables. It is possible to find a solution of system 1.14 in waves form $f(r,t) = f_k\ exp[ikr + i\omega t]$. Writing ρ, Φ and $\mathbf{v}$ in this form and substituting, one can obtain

$$\begin{aligned} &\omega\delta\rho_k + \rho_b k\delta v_k = 0 \\ &\omega\delta v_k = -k(v_s^2\delta_k + \delta\Phi_k) \\ &\delta\Phi_k = -\frac{4\pi G\rho_b\delta_k}{k^2} \end{aligned} \tag{1.15}$$

where $\delta_k = \dfrac{\delta\rho_k}{\rho_b}$. In order to obtain independent solutions, it is necessary to consider the matrix associated to 1.15: its determinant has to be equal to zero. Applying this condition, the outcome is basically a dispersion relation: $\omega^2 = v_s^2k^2 - 4\pi G\rho_b$. There are two different possible cases that have to be taken into account, distinguished by a specific value of the Jeans scale, which enters the equations as $R_J = \dfrac{2\pi}{K_J} = v_s\dfrac{\pi}{G\rho_b}$.

- $\omega^2 > 0, R < R_J$: $\omega = \pm kv_s\sqrt{1 - (\dfrac{R}{R_J})^2}$
  if ω is real, the wave $\delta = \delta_k\ exp[ikr + i\omega t]$ keeps propagating as a wave.
- $\omega^2 < 0, R > R_J$: $\omega = \pm i\sqrt{4\pi G\rho_b}[1 - (\dfrac{R}{R_J})^2]^{\frac{1}{2}}$
  if ω is imaginary, the initial wave becomes $\delta = \delta_k\ e^{ikr}exp[\pm|\omega|t]$. The positive, increasing solution is a density field perturbation that grows exponentially in a static universe.

These two solutions are discriminated by the Jeans scale $R_J = v_s\sqrt{\frac{\pi}{G\rho_b}}$, which is very similar to the expression obtained at the beginning of this section. This length is exactly the one which separates scales which can collapse from the ones that can not. In order to form a collapsed structure, it is necessary to start from a bigger scale than R_J.

1.2.3 Growth of Perturbations

In order to analyze perturbations growth deeper, it is necessary to point out two different cases: over and under the horizon R_H.

- $R > R_H$: Gravity dominates this scales, so it is possible to consider the perturbation as a closed universe in a flat one; both described by Friedmann's equations 1.11. Elaborating this concept, one gets $\delta \propto a^{1+3w}$, where w is a parameter that specifies the equation of state $P = w\rho c^2$ for different components.
  This means that perturbations always grow outside the cosmological horizon, since the scale factor increases.

- $R < R_H$: Radiation starts to become significant on this scales, so the description of the universe is less obvious. It is possible to reconsider equations of motion 1.14 and write them as a single one, as a function of the density perturbation:

$$\ddot{\delta_k} + 2\frac{\dot{a}}{a}\dot{\delta_k} + [k^2 v_s^2 - 4\pi G\rho_b]\delta_k = 0 \tag{1.16}$$

  Similarly to what was previously done, one can find solutions in a power law form $\delta_k \propto t^\alpha$. The mathematical analysis is basically analog to the previous one, with scales larger $R_J = \frac{v_s}{5}\sqrt{\frac{24\pi}{G\rho_b}}$ that can collapse. Perturbations grow following a power law in an expanding universe.

Here comes the interesting part. Note that an Einstein - de Sitter universe (flat, single component) is a good description for the majority of the history of the universe. In this context, perturbations grow according to $\delta \propto a$. Remember that the whole analysis is true in a linear approximation. Today values of $\delta \sim 10^2 - 10^3$ are measured. Let's consider that for $\delta > 1$ non linear regime allows a big, fast increment in density contrast; so

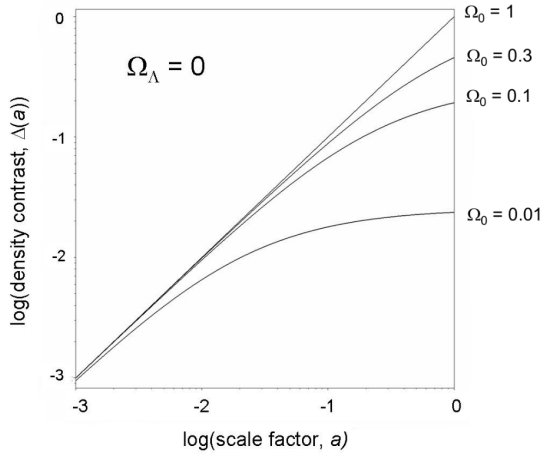

Figure 1.3: Different growth rates in four types of universes without cosmological constant: one of them is flat ($\Omega_0 = 1$), while the others are open ($\Omega_0 < 1$)

the linear regime has to get to $\delta \sim 1$. Moreover, baryonic matter had the chance to collapse after matter-radiation decoupling, around $z \sim 1000$. Putting all these aspects together, it is clear that at $z \sim 1000$, it is necessary to measure at least $\delta \sim 10^{-3}$.
However, CMB measurements estimate $\delta \sim 10^{-5}$, which is contradictory. In order to investigate deeper into this problem, one can consider a different form of Friedmann equations 1.11, deriving the second one and substituting the first one into the result, which gives:

$$\ddot{H} + 2H\dot{H} - 4\pi G\rho_b H = 0 \tag{1.17}$$

This equation has the same structure of 1.16, which allows to obtain the solution:

$$\delta_+(z) = -H(z)\int_\infty^z \frac{1+z'}{a_0^2 H^3(z')}dz' \tag{1.18}$$

This result allows to understand different growth rates in distinct types of universe, as shown in Figure 1.3.

Perturbation grow slower in an open universe (and also faster in a closed one), with respect to a flat, EdS universe. Clearly, an open universe would not solve the problem. A close one might solve it, but there are too many evidences in favor of a flat universe, including the CMB power spectrum.
A crucial aspect that has not been taken into account yet is dark matter.

This concept was introduced in the early 30s by F.Zwicky [9], who observed high galaxies velocity dispersion in the Coma cluster, indicating that the total mass of the cluster is much higher than that inferred from luminous matter alone.
Dark matter can behave differently than baryons, since its cross section with radiation is much smaller, so that there is only weak interaction. Elaborating equation 1.16 only for dark matter, in the radiation era, i.e. before decoupling, one gets the solution

$$\delta_{k,DM}(x) = 1 + \frac{3}{2}x$$

where $x = \dfrac{a}{a_{eq}}$. The biggest enhancement happens if the perturbation crosses the horizon at the big bang, which translates into a growth of

$$\frac{\delta_{a_{eq}}}{\delta_{a_{hor}}} = \frac{1 + \frac{3}{2}\frac{a_{eq}}{a_{eq}}}{1 + \frac{3}{2}\frac{a_{hor}}{a_{eq}}} = \frac{5}{2}$$

A scale of dark matter that enters the horizon at the big bang increases only by a factor 5/2 until the equivalence. This is called the *Meszaros Effect*: dark matter perturbations inside the horizon do not grow during the radiation era.
Moreover, the presence of dark matter changes baryon evolution dramatically. In fact, as soon as ordinary matter is able to evolve freely, decoupled from radiation, it will find gravitational potential wells already formed by dark matter. This translates in a faster enhancement regarding baryons. Furthermore, the solution of equation 1.16 for baryons in presence of dark matter is

$$\delta_{k,B} = \delta_{k,DM}(1 - \frac{a_{DEC}}{a})$$

Baryons perturbations begin to collapse after decoupling and then recover their delay on dark matter. This effect is called *baryon catch up*, which solves the initial growth problem: at first dark matter halos are formed and then, after decoupling, baryons can dive into them and perturbations can grow from $\delta \sim 10^{-5}$ to $\delta \sim 1$ and finally, by means of non linear regime, to values measured nowadays $\delta \sim 10^2 - 10^3$. The whole process is shown in Figure 1.4.

In particular, here is what happens in this specific case: the perturbation crosses the horizon at the equivalence, after that baryons are still

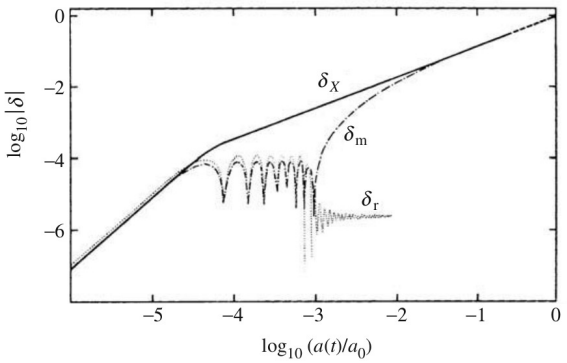

Figure 1.4: Baryon catch up effect: δ_X refers to dark matter, δ_m to baryons and δ_r to radiation

coupled to radiation and begin to oscillate with it. On the other hand, dark matter can grow. The latter does not notice decoupling and keeps growing as it was doing before. However, radiation loses the baryons support and keeps oscillating, but on lower density contrast values. Baryonic matter, instead, follows halos gravitation potential, according to the baryon catch up effect.
In conclusion, dark matter plays a crucial role in structure formation, it would not be possible to describe the universe as it seen nowadays without it. In addition, recent observations of the universe can give information about dark matter [10]. In particular, it is possible to classify it in two categories: hot dark matter (HDM) and cold dark matter (CDM). The difference resides in when the dark matter particle stops being relativistic: if this happens after decoupling we talk about HDM, while if it becomes non relativistic before decoupling we speak about CDM. This means that CDM particle candidates are in general much more massive than HDM ones, according to $K_B T_{NR} \sim m_x c^2$, where K_B is the Boltzmann constant, T_{NR} is the temperature at which the particle becomes non relativistic and m_x is its mass. A detailed analysis of the two, involving R_J linked to the Jeans mass M_J (lower limit of a spherical structure for it to collapse), predicts two much different types of structure evolution. A critical result is the Jeans mass evolution with time, shown in Figure 1.5.

Note that every structure with mass bigger than $M_J(eq)$ will always collapse. But this value is much different between HDM and CDM.

- HDM: $M_J(eq) \sim 10^{16} M_\odot$, greater than $10^{15} M_\odot$, the typical mass of a galaxy cluster.

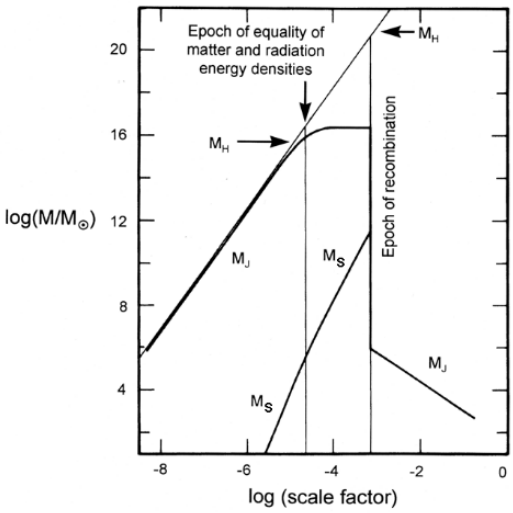

Figure 1.5: Jeans Mass M_J as a function of the scale factor a. M_H is the mass inside the horizon at a certain a, while M_S is the Silk mass, which is the mass inside the Silk scale, a typical length of a damping process caused by the interaction between photons and baryons. Note that M_J peaks at the equivalence, before dropping significantly, because of the loss of radiation support

- CDM: $M_J(eq) \sim 10^5 M_\odot$, around the typical mass of a globular cluster.

This translates into two different evolutions:

- HDM: massive structures are the first to form, while smaller ones will shape by fragmentation of the former ones. This scenario is called **TOP DOWN**: massive structures should be old.

- CDM: light structures form at first, bigger ones derive from aggregation. This is referenced as **BOTTOM UP** scenario: massive structures should be young.

In this context it is clear the importance of observations: we can see galaxies up to $z \sim 8$, while clusters are found around $z \sim 1$. This is a direct evidence in favor of CDM, which is an important base of the current model of the universe (Λ_{CDM}).

1.3 Galaxy clusters

Galaxy clusters are a concentration of 100-1000 galaxies and are the biggest virialized structures in the universe. Their typical size is $1 - 5Mpc$, with mass $10^{13} - 10^{15} M_{\odot}$. The first real galaxy cluster catalog was produced by George Abell in 1958 [13], thanks to the first Palomar Sky Survey (NGS-POSS) with the Schmidt telescope on mount Palomar. The original catalog contains 2712 clusters, selected according to a visual analysis of the photographic plates. Nowadays, clusters are usually analyzed using X-ray emission due to Bremsstrahlung radiation from hot gas. In fact, a peculiar aspect of galaxy clusters is the **Intracluster medium** (ICM), hot gas at $\sim 10^7 - 10^8 K$, with density $n_{gas} \sim 10^{-3} \frac{atoms}{cm^3}$.

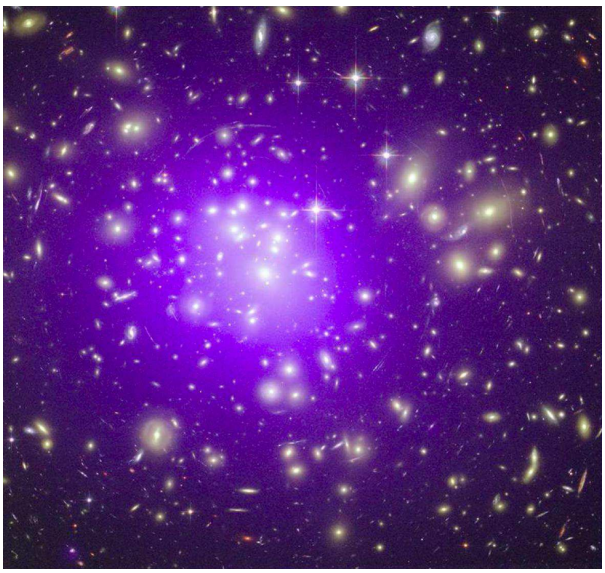

Figure 1.6: Galaxy cluster Abell 1689 at redshift z=0.18. The purple haze shows X-ray emission obtained by *Chandra X-ray Observatory*, while yellow galaxies are obtained from *Hubble Space Telescope* observation [11]

The ICM accounts for most of the baryonic mass, which represent $\sim 15\%$ of the total mass, as the remaining $\sim 85\%$ is in dark matter. The typical galaxy velocity dispersion is $\sigma_{vel} \sim 10^3\ km/s$, so that the crossing time of a cluster is $t_{cross} \sim \dfrac{R_{cluster}}{\sigma_{vel}} \sim 10^9\ yr$, which means that galaxies have had time to travel a couple of orbits in the cluster potential: these are virialized systems and there has been enough time for interactions and phenomena such as collisions and mergers. In fact, galaxies near the cluster center have less HI than other ones.
It is possible to use X-ray emission in order to estimate the cluster mass,

under the assumption of hydrostatic equilibrium. For an ideal gas $P = \frac{\rho}{\mu m_p} K_B T$ and the equation of hydrostatic equilibrium is $\frac{dP}{dr} = -\frac{GM}{r^2}\rho$. Combining these two, it is possible to obtain the mass of the cluster:

$$M(r) = -\frac{K_B T}{\mu m_p}\frac{r}{G}\left(\frac{dln\rho}{dlnr} + \frac{dlnT}{dlnr}\right) \tag{1.19}$$

It is possible to measure the gas temperature fitting X-ray observations with different models at various temperatures, while density can be obtained considering the surface brightness $S_x(R) = S_0\left(1 + \frac{R^2}{r_c^2}\right)^{-3\beta+1/2}$ (where $\beta = \frac{\mu m_p \sigma^2}{K_B T}$), assuming a given distribution of the ICM. In particular, one can obtain the parameters r_c and β from S_x and use them to compute $\rho_{gas} = \rho_0\left[1 + \left(\frac{r}{r_c}\right)^2\right]^{-\frac{3\beta}{2}}$.
Moreover, it is possible to extrapolate different scaling relations, in order to link the mass of a galaxy cluster to an observable which is easier to obtain. X-ray luminosity is typically used for this scope, according to Reiprich et al. (2012) [12].

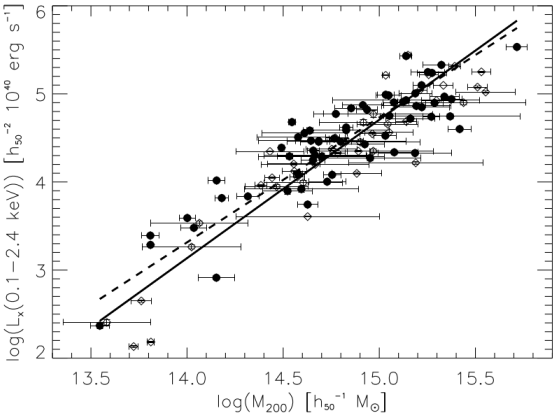

Figure 1.7: Scaling relation between X luminosity and cluster mass

One can simply measure X-ray luminosity and link it to the galaxy cluster mass.
A notable feature of galaxy clusters is the **Intra Cluster Light** (ICL). Its first qualitative report was provided by Zwicky in 1951 [16]. It is constituted by stars that are gravitationally bound to the cluster potential, but are not associated to a specific galaxy. They were stripped from their original galaxy due to encounters with mainly the Brightest Central Galaxy (BCG) or another member galaxy. The fact that it is usually aligned with the position angle of the BCG supports the first hypothesis,

but that is not always the case. It can extend to several hundreds of Kpc away from the cluster center and it is not easy to detect, since its brightness can be around a fraction of 1% of the night sky brightness. Moreover, it is difficult to distinguish light coming from the outer parts of the BCG from the ICL and the redshift dependent dimming, which is proportional to $(1+z)^4$ makes it tougher to detect it at high redshifts. It can be seen as an excess of the surface brightness profile with respect to a typical de Vaucouleur profile (de Vaucouleur 1953 [17])

$$I(R) \;=\; I_e exp\left[-b\left(\frac{R}{R_e}\right)^{\frac{1}{4}}\right] \tag{1.20}$$

where R_e is the effective radius, containing 50% of the total light.
The ICL is a crucial component in order to understand the baryonic composition if a galaxy cluster, as well as its assembly history, as reported by Guennou et al. (2012) [18] and Presotto et al. (2014) [19].

1.3.1 Clusters in Cosmology

Galaxy clusters are highly used in cosmology, mainly because they provide a way of measuring density perturbations and their redshift distribution is strongly dependent on cosmological parameters.
Generally speaking, the cosmic field density field is treated statistically, a complete summary can be found in Borgani (2006) [14] and references within. Note that if δ has a gaussian distribution, as inflation predicts it to be, the ergodic principle allows to analyze different volumes of a single universe as different universes. In this sense, it is possible to consider the Fourier transform of the density contrast

$$\widetilde{\delta}(\mathbf{k}) = \frac{1}{(2\pi)^{3/2}}\int \delta(\mathbf{x}) e^{i\mathbf{k}\cdot\mathbf{x}} dx$$

It is possible to define the two point correlation function as

$$\xi(r) = <\delta(\mathbf{x}_1)\delta(\mathbf{x}_2)>$$

where $r = |\mathbf{x}_1 - \mathbf{x}_2|$. This has to be intended as a double average: starting from a single point x_1 inside a certain volume, where $\delta(\mathbf{x}_1)$ is calculated, there will be a sphere centered in this point with radius $\mathbf{x}_2$. It is necessary

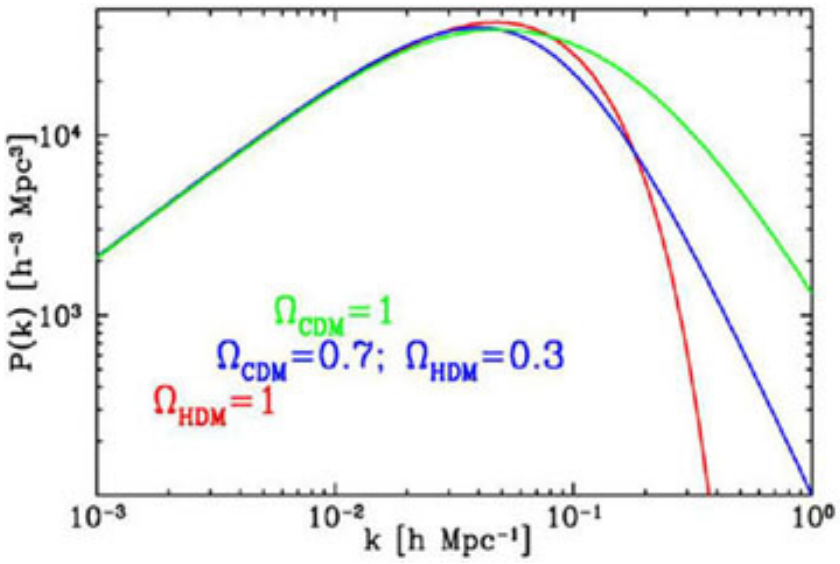

Figure 1.8: Power Spectrum of three different types of flat universes: one with only HDM (red), one with only CDM (green) and one with a combination of the two (blue)

to average the density product over the whole surface of this sphere and on every point of the volume considered.
The power spectrum $P(k) = < |\tilde{\delta}(\mathbf{k})|^2 >$ can be shown to be the Fourier analogous of the correlation function

$$\xi(\mathbf{r}) = \frac{1}{(2\pi)^3} \int P(\mathbf{k}) e^{i\mathbf{k}\cdot\mathbf{r}} d^3k \tag{1.21}$$

The power spectrum can give crucial cosmological information.

- *Inflation*: its slope at small values of $\mathbf{k}$ strictly depends on inflation, which produces scale-independent perturbations, so that $P(\mathbf{k}) \propto \mathbf{k}$

- $\Omega_{0,M}$: The power spectrum peak corresponds to the last scale which crossed the horizon without experiencing the Meszaros effect, so it depends on the cosmological horizon at the matter-radiation equivalence. The latter is closely related to total matter density by $1 + z_{eq} = \frac{\Omega_{0,M}}{\Omega_{0,R}}$.

- *Dark matter*: the scale at which the power spectrum goes to 0 is the one with no perturbations: this corresponds to the dark matter free streaming scale (K_{FS}), the one under which perturbations are canceled. K_{FS} is dramatically different between HDM and CDM, so the point where the power spectrum nullifies gives information

about dark matter.

All these aspects of the power spectrum can be derived from its Fourier analog, the correlation function, according to equation 1.21. Galaxy clusters are suitable for this task, measuring the density contrast in different volumes, in order to reconstruct the power spectrum.
Another really appropriate manner of employing clusters in cosmology is using them to reconstruct the halo mass function. According to Press-Schechter theory [15], which considers spherical collapse, it is possible to consider the probability of having a certain density contrast value as a gaussian function and integrate it considering critical values of δ given by linear theory, in order to obtain the number density of structures with mass included between M and M + dM. The result is

$$n(M)dM = \sqrt{\frac{2}{\pi}} \frac{\overline{\rho_M}}{M^2} \frac{\delta_c}{\sigma_M} \left| \frac{dln\sigma_M}{dlnM} \right| exp\Big[- \frac{\delta_c^2}{2\sigma_M^2} \Big] \tag{1.22}$$

Equation 1.22 has cosmology dependence in σ_M, linked to the integrated power spectrum, and in $\overline{\rho_M}$, linked to Ω_M. The halo mass function also depends on redshift, as can be seen in Figure 1.9.

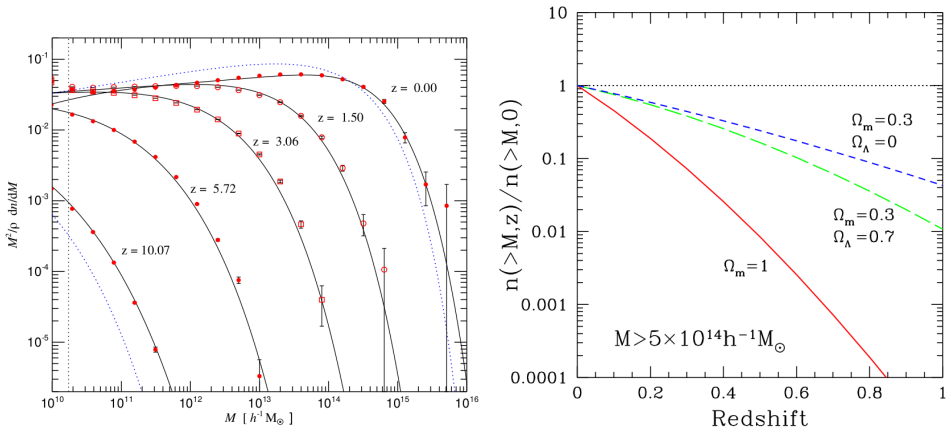

Figure 1.9: Left panel: halo mass function and its redshift dependence. Note how massive structure form recently, compatibly with a BOTTOM UP scenario. Right panel: redshift evolution of the halo mass function in different cosmologies [14]

In this context, the importance of observing clusters redshift distribution is prominent: counting clusters at different redshift allows the reconstruction of the halo mass function and the consequent possibility to constrain cosmological parameters.
Moreover, remember that perturbations grow in different ways according

to universe geometry (Figure 1.3). So, if counting clusters today unfolds values of the couple (σ_M, Ω_M), counting them at different z allows to break the degeneracy between these two parameters. This is the strength of doing cosmology with clusters.

1.3.2 Sunyaev – Zel'dovich Effect

The **Sunyaev – Zel'dovich** effect [20] provides a powerful tool to identify galaxy clusters. It is a distortion of the *Cosmic Microwave Background* (CMB) spectrum, photons released after the matter radiation decoupling permeating the universe. They were in thermal equilibrium with matter, so that it is possible to describe CMB as a black body radiation of temperature $\sim 2.73K$. These photons interact with hot gas of a cluster, where they are scattered at higher energies by hot electrons in an Inverse Compton process. This will cause a shift of the spectra as Figure 1.10 shows. The process is known as thermal SZE.

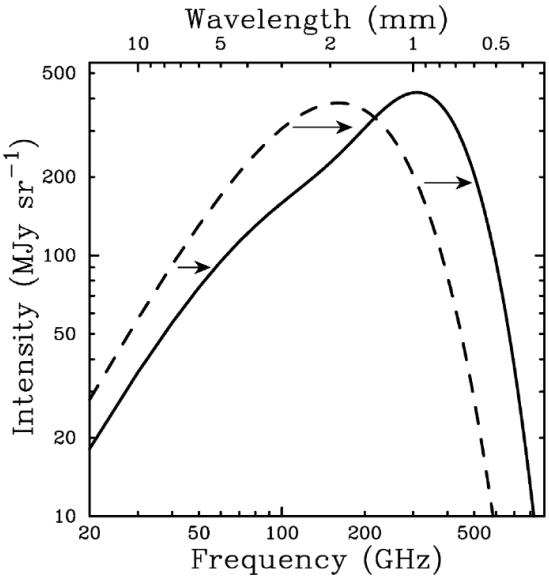

Figure 1.10: The dashed line represents the original CMB spectrum, while the solid line shows the spectrum distorted by SZ effect. In particular, there is a decrease at frequencies lower than 218 GHz and an increment at higher values [21]

The distortion of the intensity spectrum is described by

$$\frac{\partial I_\nu}{I_\nu} = -Y \frac{xe^x}{e^x - 1}\Big[4 - xcotan\big(\frac{x}{2}\big)\Big] \tag{1.23}$$

where $x = \frac{h\nu}{K_B T}$ and $Y = \int_{los} \sigma_T n_e \frac{K_B T}{m_e c^2}$ is the Compton parameter, with h being the Planck constant, K_B the Boltzmann constant, σ_T the Thomson cross-section, n_e the electron number density, T the electrons temperature and $m_e c^2$ the electron rest mass energy.
Typical relative distortion values are around $\frac{\partial I_\nu}{I_\nu} \sim 10^{-4}$, for hot clusters, with $T_{ICM} \sim 10^7 K$. This helps clusters search significantly, especially at high redshift, where X-ray radiation becomes more difficult to detect.
An eventual movement of the cluster respect to the CMB rest frame causes an an additional spectral distortion due to Doppler effect caused by this relative velocity, also known as peculiar velocity v_{pec}, along the line of sight. This is called *Kinetic SZE*. In non relativistic limit $\frac{\Delta T}{T_{CMB}} = -\tau_e \frac{v_{pec}}{c} \sim 10^{-5}$, which is negligible compared to the preponderant thermal SZE.

1.4 Gravitational Lensing

The phenomenon of gravitational lensing is the deflection of light caused by massive objects between the source and the observer (A. Einstein 1936 [22]). This section is inspired by M.Meneghetti (2017) [23].

1.4.1 Deflection angle

Gravitational lensing is a direct consequence of Einstein's general relativity, but the idea that light could be bent was already mentioned in the 18^{th} century by Newton [24] and Von Soldner [25], in the field of *Corpuscolar Theory*. A simple way to understand it was proposed by Victor J. Stenger (2013). This example allows to quantify how much light is bent by gravity; it is based on Newton's laws of gravity, Einstein's equivalence principle and the theory of special relativity (SR).
Consider a photon with momentum $\vec{p}$ grazing the surface of the sun, as shown in Figure 1.11.

Einstein's SR gives the inertial mass of the photon $m = \frac{E}{c^2}$. The distance between the Sun center and the photon is $r = \sqrt{x^2 + (a-y)^2}$. From Newton's law of motion $F_x = \frac{dp}{dt} cos\theta$ and $F_y = \frac{dp}{dt} sin\theta$, combining

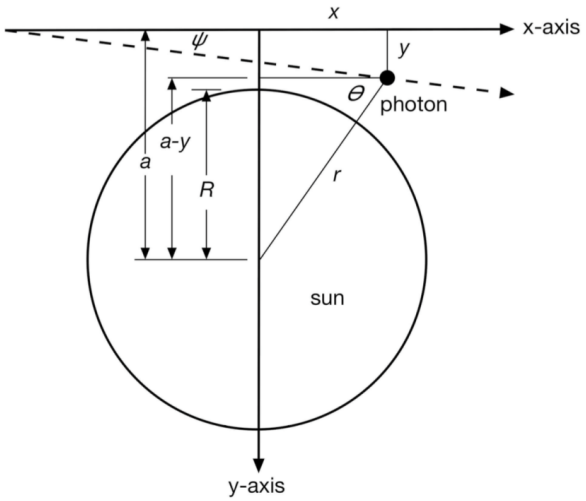

Figure 1.11: Deflection of a photon caused by the sun, which has mass M and radius R, while a is the impact parameter of the photon

them with $dx = cdt$, it is possible to obtain

$$\frac{dp_x}{dx} = \frac{GMp}{c^2}\frac{x}{[x^2+(a-y)^2]^{3/2}} \tag{1.24}$$

$$\frac{dp_y}{dx} = \frac{GMp}{c^2}\frac{a-y}{[x^2+(a-y)^2]^{3/2}} \tag{1.25}$$

Integrating equations 1.25 gives the total momentum variation along the photon trajectory.

$$\Delta p_x = \frac{GMp}{c^2}\int_{-\infty}^{+\infty}\frac{x}{[x^2+(a-y)^2]^{3/2}}dx = 0 \tag{1.26}$$

$$\Delta p_y = \frac{GMp}{c^2}\int_{-\infty}^{+\infty}\frac{a-y}{[x^2+(a-y)^2]^{3/2}}dx = \frac{2GMp}{c^2}\frac{1}{a-y} \tag{1.27}$$

It is finally possible to calculate the deflection angle as $\Psi = \frac{\Delta p_y}{p} = \frac{2GM}{c^2}\frac{1}{a-y}$, if the photon grazes the sun, it means that $a - y = R_\odot$, which gives

$$\Psi = \frac{2GM_\odot}{c^2 R_\odot} \sim 0.875'' \tag{1.28}$$

However, a more accurate approach involves general relativity.
Let's consider the Schwarzschild solution of Einstein's field equation, a good approximation of the sun gravitational field. It is described by the

line element

$$dS^2 = g_{\mu\nu}dx^\mu dx^\nu = \Big(1+\frac{2\Phi}{c^2}\Big)c^2dt^2 - \Big(1-\frac{2\Phi}{c^2}\Big)dx^2 \tag{1.29}$$

where Φ is the gravitational potential. Photons follow light-like paths, so that $dS^2 = 0$. Rearranging equation 1.29 gives the speed of light in the gravitational field $c' = \frac{dx}{dt} = c\sqrt{\frac{1+\frac{2\Phi}{c^2}}{1-\frac{2\Phi}{c^2}}} \sim c\Big(1+\frac{2\Phi}{c^2}\Big)$, so that it is possible to describe space-time as a medium with refractive index

$$n = \frac{c}{c'} \sim 1 - \frac{2\Phi}{c^2} \tag{1.30}$$

where $\Phi < 0$, so that $n > 1$. This is valid in a weak field approximation $\frac{\Phi}{c^2} << 1$. The travel time of a light path between two points A,B $\vec{x}(l)$ is $t_{travel} \propto \int_A^B n[\vec{x}(l)]dl$ and the light path is given by $\delta\int_A^B n[\vec{x}(l)]dl$, which is a standard variational problem. Describing the path with a parameter λ gives

$$\delta\int_{-\infty}^{+\infty} L(x,\dot{x},\lambda)d\lambda = 0 \tag{1.31}$$

$$L(x,\dot{x},\lambda) = n[\vec{x}(\lambda)]\Big|\frac{d\vec{x}}{d\lambda}\Big| \tag{1.32}$$

with $\dot{x} = \frac{d\vec{x}}{d\lambda}$. The light path is the solution of the Euler equation

$$\frac{d}{d\lambda}\frac{\partial L}{\partial\dot{\vec{x}}} - \frac{\partial L}{\partial\vec{x}} = 0$$

Since $\frac{\partial L}{\partial\vec{x}} = \nabla n|\dot{\vec{x}}|$ and $\frac{\partial L}{\partial\dot{\vec{x}}} = n\frac{\dot{\vec{x}}}{|\dot{\vec{x}}|}$, it is possible to rewrite it as

$$\frac{d}{d\lambda}(n\vec{e}) - \vec{\nabla}n = 0 \tag{1.33}$$

where it has been assumed that $|\dot{\vec{x}}| = 1$ and $\vec{e} = \dot{\vec{x}}$. The elaboration of equation 1.33 gives

$$n\dot{\vec{e}} = \vec{\nabla}n - \vec{e}(\vec{\nabla}n\cdot\vec{e})$$

Note that the last term is a derivative just along the light ray path, so that the whole right side is the perpendicular component of the gradient

along the light path. This consideration yields

$$\dot{\vec{e}} = \vec{\nabla}_{\perp} l n n \tag{1.34}$$

Remembering equation 1.30, we obtain

$$\dot{\vec{e}} \sim -\frac{2}{c^2}\vec{\nabla}_{\perp}\Phi$$

from which it is possible to calculate the total deflection angle as

$$\hat{\vec{\alpha}} = \vec{e}_{in} - \vec{e}_{out} = \frac{2}{c^2}\int_{\lambda_A}^{\lambda_B} \vec{\nabla}_{\perp}\Phi d\lambda \tag{1.35}$$

the problem is that the integral should be done along the light path, which in principle is not known! It is possible to consider a **Born approximation**, integrating along the unperturbed path, since weak field regime holds. Consider a light ray moving along the z-axis in a 3D space, the result will be

$$\hat{\vec{\alpha}}(b) = \frac{2}{c^2}\int_{-\infty}^{+\infty} \vec{\nabla}_{\perp}\Phi dz \tag{1.36}$$

where b is the impact parameter. In a point mass case $\Phi = -\dfrac{GM}{r}$, $b = \sqrt{x^2 + y^2}$ and $r = \sqrt{b^2 + z^2}$. Solving equation 1.36 under this assumption gives

$$\hat{\vec{\alpha}}(b) = \frac{4GM}{c^2}\begin{bmatrix} x \\ y \end{bmatrix}\left[\frac{z}{b^2(b^2+z^2)^{1/2}}\right]_0^{\infty} \tag{1.37}$$

$$|\hat{\vec{\alpha}}| = \frac{4GM}{c^2 b} \tag{1.38}$$

which is twice the classical value in equation 1.28. This result was confirmed by A.S. Eddington in 1919 [26], when he took advantage of a solar eclipse in order to analyze light deflection close to the sun surface. This attestation is considered one of the classical tests of General relativity, alongside the precession of Mercury perihelion and gravitational redshift. Note from equation 1.38 that the deflection angle scales linearly with mass: it is possible to apply the superposition principle. This is very useful for calculating the deflection angle of multiple point masses and by

an extended mass, with surface density $\Sigma(\vec{\xi}) = \int \rho(\vec{\xi}, z)dz$.

$$\hat{\vec{\alpha}}(\vec{\xi}) = \frac{4G}{c^2}\sum_i M_i \frac{\vec{\xi} - \vec{\xi}_i}{|\vec{\xi} - \vec{\xi}_i|^2}$$
$$\hat{\vec{\alpha}}(\vec{\xi}) = \frac{4G}{c^2}\int \Sigma(\vec{\xi}')\frac{\vec{\xi} - \vec{\xi}'}{|\vec{\xi} - \vec{\xi}'|^2}d^2\xi' \tag{1.39}$$

1.4.2 Basics of Lensing

Lensing phenomena depend on the relative positions of the observer, the lens and the source.

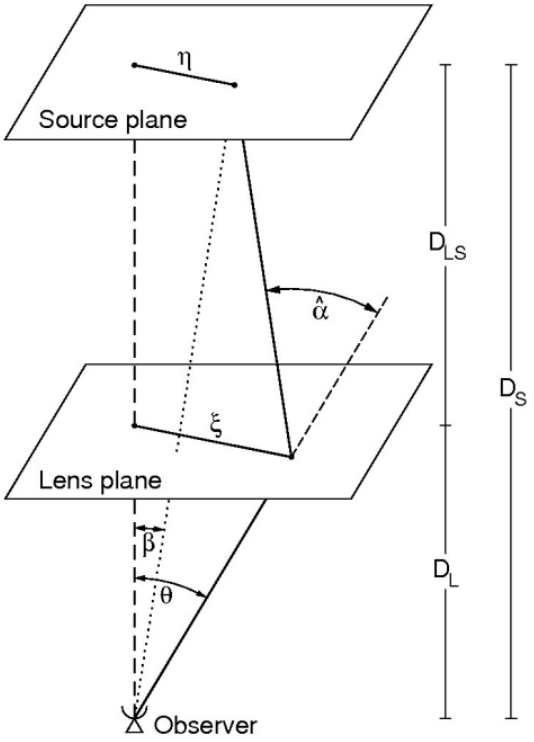

Figure 1.12: Gravitational lensing system, according to M. Bartelmann and P. Schneider (2001) [27]

Figure 1.12 shows a typical lensing scheme: photons of a source at distance D_S from the observer are bent by the lens at distance D_L from the watcher. So light that actually comes from an angle β is observed under an angle θ: the difference is basically given by the deflection angle. It is possible to relate all these angles and distances, in particular from Figure 1.12 it is clear that

$$\vec{\theta}D_S = \vec{\beta}D_S + \hat{\vec{\alpha}}D_{LS} \tag{1.40}$$

which is the **lens equation**. Moreover, considering the reduced deflection angle

$$\vec{\alpha}(\vec{\theta}) = \frac{D_{LS}}{D_S}\hat{\vec{\alpha}}(\vec{\theta})$$

equation 1.40 simply becomes

$$\vec{\beta} = \vec{\theta} - \vec{\alpha}(\vec{\theta}) \tag{1.41}$$

It is usually written in dimensionless form, considering a scale length ξ_0 on the lens plane, which translates in $\eta_0 = \xi_0 \frac{D_S}{D_L}$ on the source plane. This allows to define $\vec{x} = \frac{\vec{\xi}}{\xi_0}$ and $\vec{y} = \frac{\vec{\eta}}{\eta_0}$ and the lens equation becomes

$$\vec{y} = \vec{x} - \vec{\alpha}(\vec{x}) \tag{1.42}$$

The solutions of this simple equation depend on how complicated the deflection angle is, i.e. on the mass distribution of the lens, according to 1.35.
A very useful quantity is the projection of the 3D Newtonian potential of the lens on the lens plane.

$$\hat{\Psi}(\vec{\theta}) = \frac{D_{LS}}{D_L D_S}\frac{2}{c^2}\int \Phi(D_L\vec{\theta}, z)dz \tag{1.43}$$

In fact, it is true that the gradient of the lensing potential is the reduced deflection angle, while it Laplacian is linked to the lens surface density.

$$\begin{aligned}\vec{\nabla}_\theta\hat{\Psi}(\vec{\theta}) &= \vec{\alpha}(\vec{\theta})\\ \triangle_\theta\hat{\Psi}(\vec{\theta}) &= 2\kappa(\vec{\theta})\end{aligned} \tag{1.44}$$

where κ is called convergence and is defined as

$$\kappa(\vec{\theta}) = \frac{\Sigma(\vec{\theta})}{\Sigma_{cr}} \qquad \Sigma_{cr} = \frac{c^2}{4\pi G}\frac{D_S}{D_L D_{LS}} \tag{1.45}$$

An alternative way of reconstructing the image positions is using the so called *time delay surface*. Gravitational lensing causes a travel-time delay of light between the source and the observer. A first component is given by the gravitational field of the lens, a phenomenon known as

Shapiro delay. The second component is purely geometrical: light is bent and does not follow a straight path.
The first one can be obtained linking the gravitational field to a refractive index, going back to equation 1.30. It can be computed as the difference in time travel between an empty space case and a case with refractive index. The expression can be simplified using the lensing potential.

$$t_{grav} = \int \frac{dz}{c'} - \int \frac{dz}{c} = -\frac{D_L D_S}{D_{LS}} \frac{1}{c^2} \hat{\Psi} \tag{1.46}$$

The geometrical component can be deduced considering the longer path that light has to travel in order to reach the observer in Figure 1.12. The result is

$$t_{geom} = \frac{1}{2c} (\vec{\theta} - \vec{\beta})^2 \frac{D_L D_S}{D_{LS}} \tag{1.47}$$

Adding the expansion of the universe and combining equations 1.46 and 1.47, the total time delay surface equation is

$$t(\vec{\theta}) = \frac{1 + z_L}{c} \frac{D_L D_S}{D_{LS}} \Big[\frac{1}{2} (\vec{\theta} - \vec{\beta})^2 - \hat{\Psi}(\vec{\theta}) \Big] \tag{1.48}$$

Remembering that the deflection angle is the gradient of the lensing potential, it is possible to rewrite the lens equation as

$$(\vec{\theta} - \vec{\beta}) - \nabla \hat{\Psi}(\vec{\theta}) = \nabla \Big[\frac{1}{2} (\vec{\theta} - \vec{\beta})^2 - \hat{\Psi}(\vec{\theta}) \Big] = 0$$

which means that solving the lens equation corresponds to searching stationary points of the time delay surface.

1.4.3 Distortion and Magnification

Gravitational lensing causes distorted images of background sources: it is one of its main effects. This distortion can be described by the variation of the angle under which the source is actually located respect to the observer, as a function of the angle under which the observer sees it.

$$A = \frac{\partial \vec{\beta}}{\partial \vec{\theta}} = \delta_{ij} - \frac{\partial^2 \hat{\Psi}(\vec{\theta})}{\partial \theta_i \theta_j} \tag{1.49}$$

where i and j refer to the two angle components on the lens plane. This is the lensing Jacobian matrix. Its traceless part is linked to the

shear tensor

$$\Gamma = \begin{bmatrix} \gamma_1 & \gamma_2 \\ \gamma_2 & -\gamma_1 \end{bmatrix}$$

which is the opposite of the anisotropic part of the Jacobian matrix. The components are a function of the lensing potential

$$\begin{aligned} \gamma_1 &= \frac{1}{2}(\hat{\Psi}_{11} - \hat{\Psi}_{22}) \\ \gamma_2 &= \hat{\Psi}_{12} = \hat{\Psi}_{21} \end{aligned} \tag{1.50}$$

The Jacobian matrix can be written as a function of both convergence and shear.

$$A = \begin{bmatrix} 1 - \kappa - \gamma_1 & -\gamma_2 \\ -\gamma_2 & 1 - \kappa + \gamma_1 \end{bmatrix} \tag{1.51}$$

The lensing Jacobian basically explains how images are distorted (1.49). The convergence is thus responsible for an isotropic scaling of the image by a factor $(1-\kappa)^{-1}$, while the shear describes a specific distortion along a certain direction, according to the combination of γ_1 and γ_2 and the fact that Γ is a spin-2 tensor, invariant under rotations of π.
Given these aspects, it is immediate to understand how a circular source is modified by first order lensing effects, which means that the source is small enough to not be sensible to large variations of the deflection angle, so that moving from $\vec{\theta}$ to $\vec{\theta} + d\vec{\theta}$, the deflection angle varies according to $\vec{\alpha}' = \vec{\alpha} + \dfrac{d\vec{\alpha}}{d\vec{\theta}} d\vec{\theta}$. The source isophotes are described by $\beta_1^2 + \beta_2^2 = r^2$ and it is possible to choose a reference system where the Jacobian matrix is diagonal, so that the lens equation for this type of source is

$$\begin{aligned} \beta_1 &= (1 - \kappa - \gamma)\theta_1 \\ \beta_2 &= (1 - \kappa + \gamma)\theta_2 \end{aligned} \tag{1.52}$$

Substituting these values in the isophotes equations, yields $r^2 = (1-\kappa-\gamma)^2\theta_1^2 + (1-\kappa+\gamma)^2\theta_2^2$, which is the equation of an ellipse. A circular source is mapped onto the lens plane as an elliptical image, as long as the first order approximation holds, as shown in Figure 1.13.

Moreover, the fact that the shear tensor has spin 2 translates in different distortions according to its components:

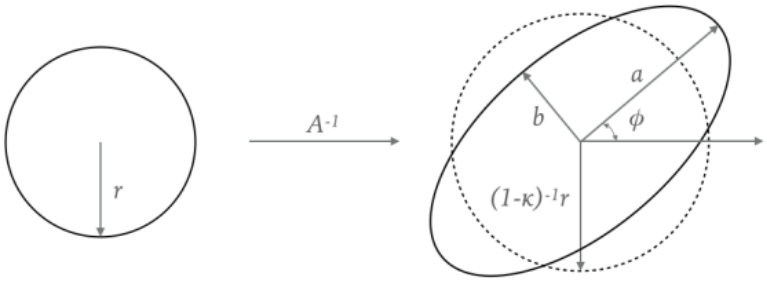

Figure 1.13: First order lensing effects on a circular source: it is mapped as an ellipse

- $\gamma_1 > 0$, $\gamma_2 = 0$: major axis of the ellipse is along θ_1;
- $\gamma_1 = 0$, $\gamma_2 > 0$: major axis of the ellipse forms an angle of $\pi/4$ with θ_1;
- $\gamma_1 < 0$, $\gamma_2 = 0$: major axis of the ellipse is perpendicular to θ_1;
- $\gamma_1 = 0$, $\gamma_2 < 0$: major axis of the ellipse forms an angle of $3\pi/4$ with θ_1

Figure 1.14 shows these cases and also additional combinations.

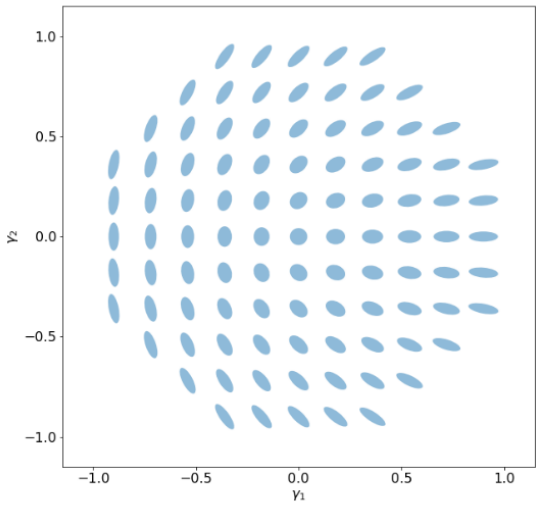

Figure 1.14: Images orientations according to different combinations of γ_1 and γ_2

An other crucial aspect of lensing is image **magnification**. Light is deflected, but there is no creation or destruction of photons: the surface brightness of the source is conserved. In addition, light deflection causes

a variation of the solid angle under which the image is observed, so that the source flux can be amplified. Intuitively, if the source is lensed in a smaller angular image, its observed flux will be greater. This information is basically the inverse of the nature of the Jacobian matrix, in fact

$$\mu = \frac{1}{detA} = \frac{1}{(1-\kappa)^2 - \gamma^2} \tag{1.53}$$

The inverse of the eigenvalues of the Jacobian matrix quantify the amplification of the image. It is possible to consider tangential and radial magnification factors

$$\begin{aligned} \mu_t &= \frac{1}{\lambda_t} = \frac{1}{1-\kappa-\gamma} \\ \mu_r &= \frac{1}{\lambda_r} = \frac{1}{1-\kappa+\gamma} \end{aligned} \tag{1.54}$$

This means that the magnification is potentially infinite where the eigenvalues are null. The curves along which $\lambda_t = 0$ and $\lambda_r = 0$ are respectively the tangential and the radial *critical lines*. If an image forms close to the tangential critical line, it will be strongly distorted parallel to this line, while if the image is close to the radial critical line it will be distorted perpendicularly to it. These can be mapped onto the source plane using the lens equation 1.40, obtaining the tangential and radial *caustic lines*.

Magnification can also be linked to the time delay surface (see equation 1.48). In fact, its Hessian matrix corresponds to Jacobian matrix.

$$T = \frac{\partial^2 t(\vec{\theta})}{\partial\theta_i \partial\theta_j} \propto \delta_{ij} - \hat{\Psi}_{ij} = A \tag{1.55}$$

The curvature of the time delay surface is inversely proportional to the magnification. In this context, it is possible to distinguish three separate cases:

- **Positive** eigenvalues
  $detA > 0 \;\; trA > 0$, minimum of $t(\vec{\theta})$, *positive* magnification;

- **Opposite** eigenvalues
  $detA < 0$, saddle point of $t(\vec{\theta})$, *negative* magnification;

- **Negative** eigenvalues
  $detA > 0 \;\; trA < 0$, maximum of $t(\vec{\theta})$, *positive* magnification;

Note that negative magnification does not mean demagnification, which happens when $|\mu| < 1$, while the sign of the amplification factor refers to the image orientation.

1.4.4 Power Law Lenses

This section presents a specific case where the lens equation 1.42 can be solved analytically: a power law lens. For a general lens with spherical symmetry, it is possible to rewrite the lens equation as

$$\begin{aligned} y &= x - \frac{m(x)}{x} \\ m(x) &= 2\int_0^x x'\kappa(x')dx' \end{aligned} \tag{1.56}$$

where $m(x)$ is called dimensionless mass. A power law lens is described by $m(x) = x^{3-n}$, so that $\alpha(x) = x^{2-n}$. Moreover, it is possible to compute the convergence as

$$\begin{aligned} \kappa(\theta) &= \frac{1}{2}\left[\hat{\Psi}'' + \frac{\hat{\Psi}'}{\theta}\right] \\ \kappa(x) &= \frac{1}{2}\frac{m'(x)}{x} = \frac{3-n}{2}x^{1-n} \end{aligned} \tag{1.57}$$

the lens will act accordingly to the value of the exponent n:

- $n < 1$: the convergence grows with x, which is non physical;
- $n = 1$: the convergence is constant, every point is mapped into $y = 0$, this is a completely convergent lens;
- $1 < n < 2$: the convergence falls with x, which is physical, and the deflection angle is null at the origin;
- $n = 2$: the deflection angle is constant
- $2 < n < 3$: the deflection angle diverges at the origin
- $n = 3$: $m(x) = 1$, this is the case of a point lens;

- $n > 3$: $m(x)$ falls with x, which has no physical sense

The easiest way to understand what happens to images of sources processed by these types of lenses is exploiting the *image diagram*. It compares the two functions $f(x) = x - y$ and $\alpha(x)$. The images will be formed where these two functions overlap, i.e. where the lens equation is solved. Figure 1.15 [23] shows some examples for different values of n.

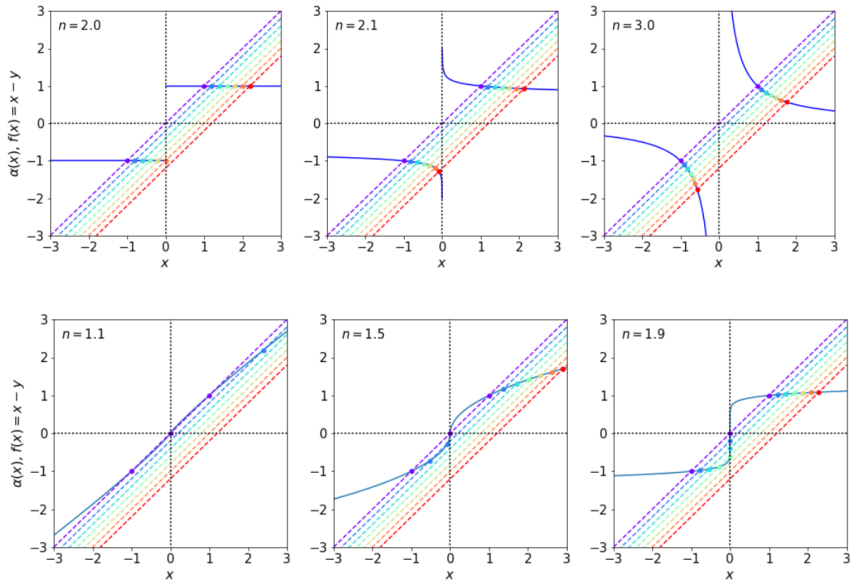

Figure 1.15: Image diagrams for different values of n. The solid curve indicates the deflection angle $\alpha(x)$, while the dashed lines show the function $f(x) = x - y$ for different values of y, in the range $[0, 1.2]$

The number of intersections in each diagram corresponds to the number of multiple images produced by the system and the x value of the intersection is the point on the lens plane where the image is actually formed. Moreover, it is also possible to compute the eigenvalues of the Jacobian matrix according to equation 1.54, obtaining

$$\begin{aligned} \lambda_t &= 1 - x^{1-n} \\ \lambda_r &= 1 - (2-n)x^{1-n} \end{aligned} \tag{1.58}$$

The critical lines are individuated where λ_t and λ_r are null. The tangential critical line is given by $x = 1$ and is called *Einstein ring*, it is independent of x and is mapped into a point caustic in $y = 0$. On the other hand, the radial critical line does depend on x and will be located in $x_r = (2-n)^{-\frac{1}{1-n}}$.

1.4.5 Microlensing

The term *microlensing* refers to lensing effects generated by small lenses, such as stars and planets, so that the lens can be approximated to a point mass. It is not really related to this thesis, but a quick overview is important to present different gravitational lensing aspects. In this context, an important quantity is the *Einstein radius*

$$\theta_E = \sqrt{\frac{4GM}{c^2}\frac{D_{LS}}{D_L D_S}} \tag{1.59}$$

which allows to rewrite the lens equation 1.40 as

$$\begin{aligned} \beta &= \theta - \frac{\theta_E^2}{\theta} \\ y &= x - \frac{1}{x} \end{aligned} \tag{1.60}$$

as every angle can be scaled by θ_E. This is a quadratic equation, with two solutions: a single source can have multiple images. In particular, the solution of equation 1.60 is

$$x_\pm = \frac{1}{2}\left[y \pm \sqrt{y^2+4}\right]$$

A source placed behind the center of the lens, at $y = 0$, produces images in $x_\pm = \pm 1$: it is lensed in θ_E. This configuration is called *Einstein ring*, an example is shown in Figure 1.16.

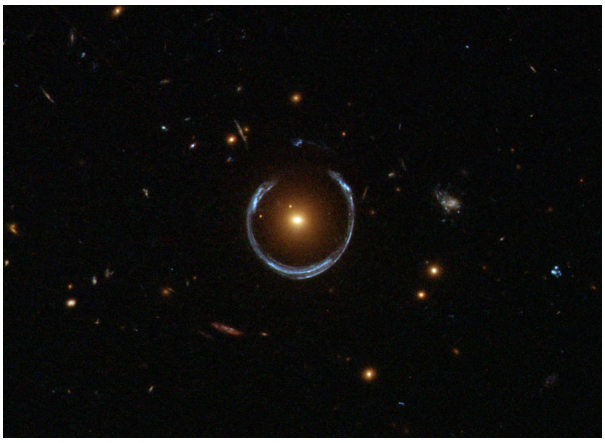

Figure 1.16: Horse-shoe Einstein ring. Image credit: ESA/HUBBLE and NASA. Astronomy Picture of the Day 21/12/2011

Generally speaking, the size of an Einstein radius caused by a massive

galaxy at a typical distance of the order of Gpc is around $1''$, while for a star inside the Milky Way it is around $(10^{-3})''$: multiple images are separated by this tiny angle, which does not allow to resolve them. This case can be analyzed using the *microlensing light curve*: the light curve of the source is distorted by the relative motion between the source and the lens. An example given by Lee et al. (2009) [28]. Moreover, the light curve is distorted by the specific line of sight under which the microlensing event is seen: making multiple observations from different point of views helps reconstructing the lens features. There are three possible ways of seeing different relative positions of the lens and the source, exploiting the so called microlensing parallax:

- *Orbital Parallax*: the light curve is distorted by the Earth motion around the sun;
- *Satellite Parallax*: simultaneous ground and space based observations allow the measurement of the same light curve with different distortions;
- *Terrestrial Parallax*: uses the same concept of satellite usage, but combining multiple ground based telescopes

An expansion of these aspects can be found in [29], focused on the Spitzer telescope.
Microlensing studies allowed the detection of around 2000 events per year from 2011 to 2017 in the galactic bulge and the detection of 75 exoplanets (April, 2019).

1.4.6 Lensing by galaxy clusters

Overall, gravitational lensing offers a powerful tool to recover mass profiles of galaxy clusters that act as a lens, helping, for example, the construction of the halo mass function (1.9), explained in previous sections. It is possible to distinguish between two main lensing regimes

- **Strong Lensing**: it is characterized by elongated arcs and multiple images, usually in the central part of the cluster, where the surface density exceeds the critical surface density

- **Weak Lensing**: it does not highlight evident distortions, but it rather shows a stretch of the images of background sources perpendicular to the direction individuated by the image and the lens.

The most immediate way of exploiting strong lensing features is building a lens model and fit it with observations.
This allows to inquire the core distribution of the cluster, its dark matter distribution. Moreover, magnification of distant and faint sources permits the observations of objects at redshift $z > 8$, going back to the Reionization epoch.
Strong Lensing models are usually based on three main constrains

- Position of the images, linked to deflection angle, i.e. to the first derivate of the lensing potential (1.43);
- Magnification (1.53), which depends on convergence and shear (second derivate of lensing potential);
- time delay, directly proportional to the lensing potential (1.48), very useful in case of multiple images of variable sources.

Obviously, a cluster lens is really complicated, it can have multiple substructures, which means a lot of free parameters in the lens model. A possible way of reducing them is modeling these substructures with scaling relations, like the Faber-Jackson relation between luminosity and velocity dispersion [30]. A complete example of the model reconstruction is given by Caminha et al. (2016) [31].
In general, the lens model can be obtained as a parametric model. This means that the lens is described by a certain set of parameters and the goal is to find a combination of these parameters that can describe the observation of lensing features. The following example describes this process using the positional constrain: the starting point to consider is the positions of the lensed images.
At this point, **ray tracing** is performed: a set of light rays is propagated from the observer, through the lens plane, to the source plane, making use of the deflection angle which describes the lens taken into consideration. This is done exploiting the lens equation 1.41. An example is shown in Figure 1.17

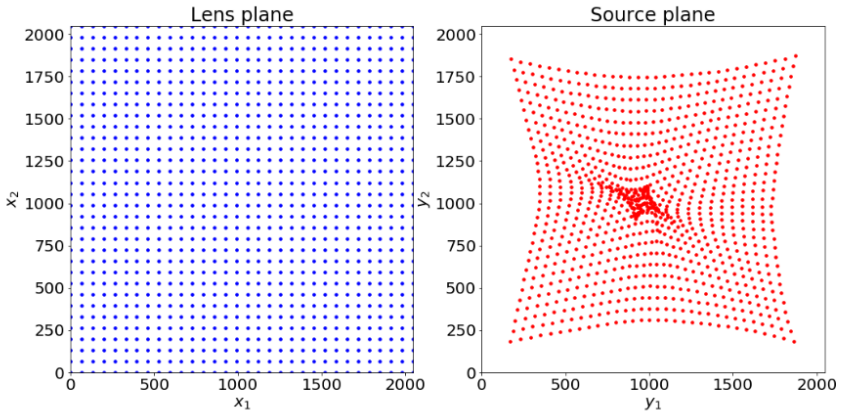

Figure 1.17: Left panel: regular grid of light rays on the lens plane. Right panel: grid of the same light rays mapped onto the source plane

The grid on the source plan is not regular because the deflection angle varies across the field. Moreover, note how light rays are denser in the central part of the source plane: this is linked to magnification. Small areas on the source plan are mapped onto bigger ares in the lens plane. So, starting from the image positions, ray tracing allows to reconstruct the source positions. For example, if the model perfectly describes the real lens, the source position of multiple images will be the same. This positions are then mapped back on to the image plane: it is useful to do this dividing the grid in triangles, which remain convex figures through the ray tracing process. This gives a set of image positions predicted by the model. The goal is to minimize the χ^2 between observed and predicted positions and maximize the likelyhood for the parameters that describe the lens:

$$\begin{aligned} \chi_i^2 &= \sum_{j=1}^{n_i} \frac{(\theta_{obs}^j - \theta_p^j)}{\sigma_{ij}^2} \\ \mathcal{L} &= \prod_{i=1}^{N} \frac{1}{\prod_{j=1}^{n_i} \sigma_{ij}\sqrt{2\pi}} exp\left[-\frac{\chi_i^2}{2}\right] \end{aligned} \tag{1.61}$$

where the index i refers to a single source and the index j refers to multiple images of that source, θ_{obs}^j is the observed position of an image, θ_p^j is the position of the image obtained considering the lens described by a set of parameters p, σ_{ij} is the uncertainty on the image position, n_i is the total number of multiple images of a single source and N is the

total number of sources that present multiple images. Minimizing χ_i^2 and maximizing $\mathcal{L}$ gives the set of best fit parameters that describe the lens.

Clusters are usually observed as part of specific programs and surveys, which allow to build galaxy clusters catalogs through deep observations of large areas of the sky, aiming at finding this type of objects. Obviously, significant progress has been done since the first Abell catalog, so here follows a list of the most notable surveys related to this thesis up to date.

- SDSS (*Sloan Digital Sky Survey*, York et al. [32]) is an imaging and spectroscopic survey in different bands, performed with a wide angle optical telescope at Apache Point Observatory in New Mexico. Data collection began in 2000, while the last data release is scheduled for 2020. Overall, around 100 million stars, 1 million galaxies and 100000 quasars have been cataloged, around 23000 of those present strong lensing features;

- SLACS (*Sloan Lens ACS Survey*, Bolton [33]) combines SDSS observations with follow ups by the Hubble Space Telescope, in order to build a larger sample of strong gravitationally lensed systems;

- CLASH (*Cluster Lensing and Supernova survey with Hubble*, Postman et al. (2012) [34]) focused on 25 galaxy clusters, observing them in 16 different filters. The first goal was clusters imaging, followed by Supernovae and galaxies detection. The cluster sample spans from redshift $z = 0.15$ to $z = 0.9$ and was observed until 2013;

- MACS (*MAssive Cluster Survey*, Ebeling et al. (2001) [35]) observed 124 spectroscopically confirmed clusters, selected from the ROSAT all sky survey, at redshift between $z = 0.3$ and $z = 0.7$. The most distant lensed galaxy based on photometric redshift has been found as part of this survey, at $z = 10.7$ (MACS0647-JD);

- CLASS (*Cosmic Lens All-Sky Survey*, S.T. Myers et al. (2002) [36]) aims at finding radio loud gravitationally lensed systems. Data were taken between 1995 and 2005 by the main radio telescopes on Earth, such VLA (Very Large Array) or VLBI (Very Long Baseline

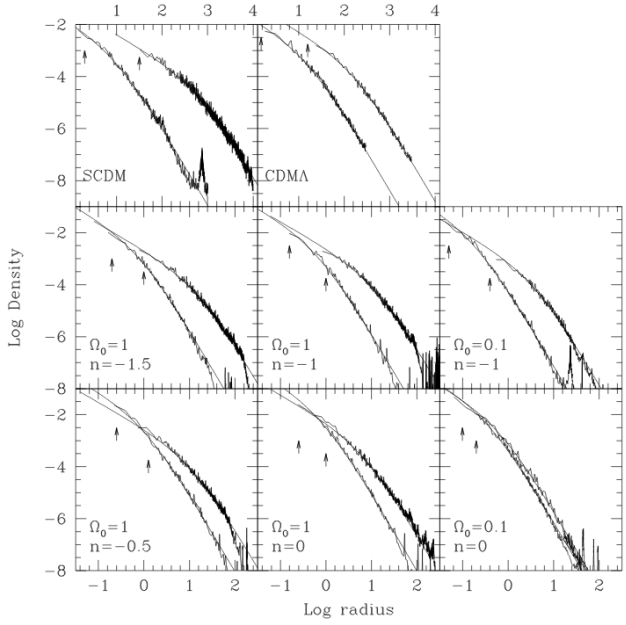

Figure 1.18: Density profiles of different DM halos produced with N-Body simulations in different cosmologies (Λ_{CDM} and S_{CDM}, standing for Standard Cold Dark Matter, which does not include the cosmological constant). The parameter n is the initial density power spectrum index.

Interferometry). More than 10000 radio sources have been analyzed, finding different multiple images systems;

- HFF (*Hubble Frontier Field*, Johnson et al. (2014) [37]) is a program based on the observation of six strong lensing galaxy clusters, selected from Abell and MACS catalogs, aiming at obtaining new and improved constrains on dark matter and strong lensing. Both Hubble and Spitzer telescopes have been used.

The mass density profile of a galaxy cluster can usually be described by a Navarro-Frank-White profile:

$$\rho(r) = \frac{\rho_s}{\frac{r}{r_s}(1+\frac{r}{r_s})^2} \tag{1.62}$$

This profile was obtained from N-Body simulations of dark matter halos in hierarchically clustering universes (Navarro et al. (1996) [38]). Its shape is common for halos of different masses and does not depend directly from cosmological parameters. Figure 1.18 shows an example.

On one hand, strong lensing inquires the inner part of the mass

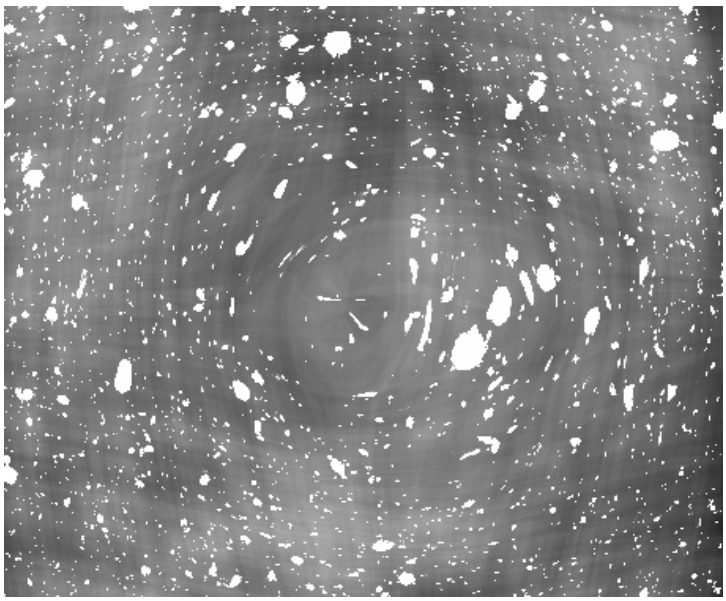

Figure 1.19: Simulated galaxies lensed by a massive cluster at the center of the image: note how images located far away from the cluster center tend to align tangentially to the direction image-cluster center due to weak lensing action

distribution of a galaxy cluster. On the other hand, *weak lensing* can give information of the mass profile at the external part of the cluster, allowing to build the cluster mass function and put constrains on cosmological parameters, as well as test different dark matter models. The idea is that both κ and γ are nearly constant on galaxies scales, so that weak lensing creates elliptical images of circular sources (Figures 1.13 and 1.14). In fact, if galaxies were circles, it would possible to measure the reduced shear simply from an ellipticty measure.

$$\begin{aligned} a =& \frac{r}{1-\kappa-\gamma}, \qquad b = \frac{r}{1-\kappa+\gamma} \\ \epsilon =& \frac{a-b}{a+b} = \frac{2\gamma}{2(1-\kappa)} = \frac{\gamma}{1-\kappa} \sim \gamma \end{aligned} \tag{1.63}$$

In particular, as we will also deepen in the next chapter, it introduces a pure tangential ellipticity, i.e. perpendicular to the direction identified by the image position and the cluster center, as suggested by Figure 1.19.

It is possible to measure the ellipticity by means of a second order tensor, which describes brightness moments, both on the source and on

the image plans.

$$Q_{ij} = \frac{\int d^2\theta I(\theta) q_I[I(\theta)](\theta_i - \overline{\theta_i})(\theta_j - \overline{\theta_j})}{\int d^2\theta I(\theta) q_I[I(\theta)]}$$
$$Q^{(s)}_{ij} = \frac{\int d^2\beta I^{(s)}(\beta) q_I[I^{(s)}(\beta)](\beta_i - \overline{\beta_i})(\beta_j - \overline{\beta_j})}{\int d^2\beta I^{(s)}(\beta) q_I[I^{(s)}(\beta)]} \tag{1.64}$$

where q_I is a weight function, which allows to select the proper scale covered by a galaxy, $I(\theta)$ and $I^{(S)}(\beta)$ are the surface brightness on the image and source plane respectively and $\overline{\theta}$ and $\overline{\beta}$ are the image centroids

$$\overline{\theta} = \frac{\int d^2\theta I(\theta) q_I[I(\theta)]\theta}{\int d^2\theta I(\theta) q_I[I(\theta)]} \qquad \overline{\beta} = \frac{\int d^2\beta I^{(s)}(\beta) q_I[I^{(s)}(\beta)]\beta}{\int d^2\beta I^{(s)}(\beta) q_I[I^{(s)}(\beta)]}$$

The trace of Q_{ij} describes the size of the image and for circular isophotes it is true that $Q_{11} = Q_{22}$ and $Q_{12} = Q_{21} = 0$.
The eigenvalues obtained diagonalizing Q_{ij} are linked to the inverse of each semi-axis:

$$\begin{aligned} \lambda_+ &= \frac{1}{2}\left(Q_{11} + Q_{22} + \sqrt{(Q_{11} - Q_{22})^2 + 4Q_{12}}\right) = \frac{1}{a^2} \\ \lambda_- &= \frac{1}{2}\left(Q_{11} + Q_{22} - \sqrt{(Q_{11} - Q_{22})^2 + 4Q_{12}}\right) = \frac{1}{b^2} \end{aligned} \tag{1.65}$$

which means that considering a complex definition, where $|\epsilon| = \sqrt{\epsilon\epsilon*} = \sqrt{\epsilon_1^2 + \epsilon_2^2}$, the ellipticity can be calculated as

$$\epsilon = \frac{Q_{11} - Q_{22} + 2iQ_{12}}{Q_{11} + Q_{22} + 2(Q_{11}Q_{22} - Q_{12}^2)^{1/2}} \tag{1.66}$$

The intrinsic ellipticity is similarly described by $Q^{(s)}_{ij}$. The observed ellipticity on the lens plane and the intrinsic ellipticity on the source plane are linked by the lens equation, which means that in a first order approximation $\beta = A\theta$, with A being the lensing Jacobian, in a reference system centered at the origin. The tensors on the two planes are linked by the relation

$$Q^{(s)} = AQA^T = AQA \tag{1.67}$$

It is possible to relate the intrinsic ellipticity of the source to the ellipticity of the image using the reduced shear $g = \frac{\gamma}{1-\kappa}$: combing the

definition of the lensing Jacobian 1.51, the ellipticity 1.66 and the relation 1.67 yields

$$\epsilon^{(s)} = \begin{cases} \dfrac{\epsilon - g}{1 - g^*\epsilon} & \text{if } |g| \leq 1 \\ \dfrac{1 - g\epsilon^*}{\epsilon^* - g^*} & \text{if } |g| > 1 \end{cases} \tag{1.68}$$

Working with a large number of galaxies, it is expected to have sources with random orientation, i.e. random phases of the complex ellipticities, so that a null average expected value of intrinsic ellipticity makes sense. In this case, it is true that

$$\epsilon = \begin{cases} g & \text{if } |g| \leq 1 \\ \dfrac{1}{g^*} & \text{if } |g| > 1 \end{cases} \tag{1.69}$$

Therefore, ellipticity measures the reduced shear. Unfortunately, additional distortions on galaxies images are given by different contributions, such as the atmosphere and instrumental effects, the details will be discussed in the next chapter.
Shear profiles are a powerful tool in order to estimate the cluster mass, the following procedure is usually adopted.

- Selected background galaxies and measure their ellipticity;
- Identify the cluster center and measure the average ellipticity in different radial bins;
- Choose a lens model (e.g. NFW 1.62) and calculate its reduced shear;
- Fit this model to ellpiticity measurements (equation 1.69), obtaining model parameters (e.g. ρ_s and r_s);
- Calculate the mass profile $M(r)$ integrating the density model profile.

This is the principle of operation, specific details, also involved in this thesis work, will be discussed in following chapters.

Chapter 2

Methodology of the analysis

This thesis is centered around the topic of **weak lensing**, introduced in the last section.
The idea is to learn how to make a weak lensing analysis, so basically reconstruct shear profiles using simulated galaxies surrounded by different types of noise. Moreover, the intent is to use these profiles in order to obtain the mass of the cluster that acts as the lens, distorting the images of galaxies. In order to investigate on weak lensing features, different types of simulations have been produced, with a variety of telescopes, source catalogs and deflectors.
Note that in this work I have always considered a Flat Λ_{CDM} cosmology with $\Omega_\Lambda = 0.7$ and $\Omega_M = 0.3$.

2.1 Simulations with Skylens

Simulations have been performed by means of a fortran90 code, named SkyLens. A first description of the code can be found in *Meneghetti et al.* (2008) [39], while a recent overview is given by *Plazas et al.* (2018) [40]. The fortran language might seem a bit obsolete, but it is still one of the most efficient in terms of computational speed, in fact is still widely used, especially for simulations in various fields, like gravitational lensing, cosmology and hydrodynamics, for example SuperNovae explosions or AGN activity.
This is the principle of operations: as for the sources, the code uses stamps containing real galaxies, which have been observed in the Hubble

Ultra Deep Field. Moreover, these objects have been cleaned from noise. They are placed behind the cluster that acts as the lens and ray-tracing is implemented in order to obtain the lensed image of the background sources.
Moreover, Skylens can introduce typical observational noise in the images, so that the output of the simulation is actually composed by two images: one with only the lensed galaxies and one with the addition of noise, which basically constitutes a simulated observation. It is possible to obtain mock observations with a variety of telescopes, both ground and space based, different filters and exposure times: this might allow to compare simulations with real data from the main telescopes. Let's take a look at the principal telescopes that can observe lensing features.

- *Hubble Space Telescope*: HST is a space based telescope, it was launched in April 1990 by NASA. Its primary mirror has a 2.4 m diameter, with many instruments that allow to span from UV to NIR parts of the electromagnetic spectrum. These include the Wide Field Camera (WFC), installed in 2009, which is the most advanced instrument mounted on HST. It covers both the UVIS and the IR bands, with a Field of View (FOV) of 164×164 $arcsec^2$, with a resolution of 0.04 $\frac{arcsec}{px}$. It is responsible for some of the best looking recent images, like the Pillars of Creation. A bigger field of view of 204×204 $arcsec^2$ is covered by the *Advanced Camera for Surveys* (ACS). It is equipped with a set of 38 filters, that allow the production of quality imaging and spectroscopy.

- *Spitzer Space Telescope*: SST is a space based telescope, launched in 2003 and is planned to be retired in 2020. Because it works in the IR band, its detectors are kept at a temperature of only 5 degrees over the absolute zero. Its three cameras allow the analysis of wavelengths that span from 3.6 μm to 160 μm. SST offers the best opportunity to measure Satellite Parallax in the context of microlensing. Nowadays, exoplanets are one of the most important themes of Spitzer research.

- *Subaru Telescope*: Subaru is a ground based reflecting telescope, with a primary mirror of 8.2 m. It is located at the *Mauna Kea Observatory* in Hawaii and is run by the National Astronomical

Observatory of Japan. It has four focal points, where several cameras and instruments can be mounted, covering Visible and IR bands. One of these is FMOS (Fiber Multi Object Spectrograph), which allows to obtain spectra of up to 400 objects, either stars or galaxies, simultaneously; The most notable is the Hyper Supreme Cam (HSC), which replaced the Suprime Cam in 2012. It is a 870 megapixel camera, that covers a very large FOV, around 1.5°, which is ideal to study weak lensing distortions at large radii from a cluster center.

- *Very Large Telescope*: VLT is located in the Atacama Desert in Chile and is an ensamble of four telescopes, each with a main mirror of 8.2 m, that can also be combined together to do interferometry. It is administrated by ESO (European Southern Observatory). It has an incredible amount of instruments, both for imaging and spectroscopy, as well as fiber instruments. The most notable renovation was done in 2017, with the introduction of laser tomography on VLT4: this adaptive optics technology allows to obtain images that reach basically the diffraction limit of the telescope, correcting seeing effects on the PSF (Point Spread Function).

- *Euclid*: Euclid is a space based project run by ESA (European Space Agency). The telescope will have a primary mirror of 1.2 m and will cover the optical and infrared bands. The goals are to investigate on the nature of dark matter and dark energy, providing state of the art constrains on their description, using weak gravitational lensing and galaxy clustering. The launch is expected in 2021. A review of the project is provided by Racca et al. (2016) [41].

Figure 2.1: Pictures of the Hubble Space Telescope (left) and the Subaru telescope (right). Credits to NASA/ESA/NAOJ

Skylens can produce mock images with a variety of telescopes, according to their characteristics. The following part of this section is meant

to describe the characteristics and parameters of this code, as well as its more detailed operation.

2.1.1 Input file

The input file contains every crucial information needed to do the simulation, like the size of the *FOV*, the exposure time and options to include noise, background galaxies and lensing effects. A notable input is the *PSF* file, which has to be convolved with simulated galaxies. If the observation is ground based, a seeing value has to be specified: in this work a value of $\theta_{seeing} = 0.6$" has been considered.
The telescope has to be specified: Skylens can produce simulations with basically every telescope, including *HST*, Euclid and Subaru. Fundamental parameters are the pixel scale, the gain (number of electrons produced by a photon on the detector) and the *RON* (Read Out Noise), which is the error in associating a certain number of electrons to the proper wavelength channel. This is necessary to define the total throughput function, which is the result of an observation.

$$T(\lambda) = C(\lambda)M(\lambda)R(\lambda)F(\lambda)A(\lambda) \tag{2.1}$$

where λ is the wavelength, C(λ) is the detector quantum efficiency, i.e. how many photons that reach the detector are actually converted into electrons, M(λ) is the reflectivity, which is the percentege of photons that are reflected correctly onto the focus, R(λ) is the transmission of the optical system, which basically counts how many photons are lost between the primary mirror and the detector and also includes the filter, F(λ) is true flux of the source and A(λ) is the extinction function.
Skylens produces a map of photon counts in each pixel, which is the sum of three different contributions: in each pixel there will be electrons related to photons from the sources and the sky, as well as the dark current contribution. This last term is given by thermal electrons in the conduction band and is not linked to photons striking the detector. The

counts in each pixel can be written as

$$n_\gamma(\vec{x}) = \frac{\pi D^2 t_{exp} p^2}{4h} \int I(\vec{x}, \lambda) \frac{T(\lambda)}{\lambda} d\lambda$$
$$n_{sky} = \frac{\pi D^2 t_{exp} p^2}{4h} \int \frac{T_\lambda S_\lambda}{\lambda} d\lambda \tag{2.2}$$

where D is the primary mirror diameter, t_{exp} is the exposure time, p is the pixel width in arc seconds, $I(\vec{x}, \lambda)$ is the surface brightness of the source, h is the Planck constant and S(λ) is the flux from the sky. The dark current term can be given in electrons per second or as the equivalent of the sky brightness, it is a term that depends on the detector electronics. Another crucial input is the catalog of background sources, which has to be generated by an external utility. The creation of this catalog is based on the **HUDF** (Hubble Ultra Deep Field), described in *Rafelski et al.* (2015) [42] and the **XDF** (Extreme Deep Field), described in *Illingworth et al.* (2013) [43]. These fields have been studied with *HST* and cover an area of around 12 arcmin^2 on the sky, but deep observations and techniques such as photometric redshift (when spectroscopic data is not available) and Lyman break analysis allow the study of galaxies at $z > 7$. Wavelengths span from Ultra Violet to Near Infrared, analyzed with both WFC3 and ACS cameras of HST. The result is a catalog of sources, each with its own ID, coordinates (both in pixels on the mosaic and in right ascension, declination in the J2000 reference frame) and a list of properties such as magnitude, flux and redshift.

These galaxies are used as templates to create a random distribution of galaxies, giving the size of the *FOV*, the filter used to calculate the flux, a specific band used to observe the *UDF* in order to rescale fluxes and the magnitude limit of the catalog. Note that it is important that the filter given to calculate fluxes is compatible with filter and telescope used to make the simulation. At this point, a certain number of galaxies is generated, proportionally to the ratio between the FOV of the catalog and the UDF. Position and angle on the sky surface are assigned randomly, while the flux of each galaxy is calculated according to its *SED* (Spectral Energy Distribution) template and the filter considered. After applying the proper cuts in Magnitude and/or redshift, the result is a catalog of background sources that will be given to Skylens as an input and will be processed in order to get a simulated observation.

2.1.2 Deflector

The deflector is another crucial input of the code. This is a fits cube file containing the two components of the deflection angle (see equation 1.36). In order to produce several simulations, I was given 29 mass maps of simulated galaxy clusters at 6 different redshift values (0.507, 0.444, 0.404, 0.385, 0.366, 0.247), obtained by means of N-body simulations combined with hydrodynamics, which are extensively discussed by *Rasia et al.* (2012) [44]. From the 3D mass map, it is possible to obtain a 2D map projecting the mass profile along one axis (Figure 2.2), so that every cluster at a single redshift can be projected along three different axes.

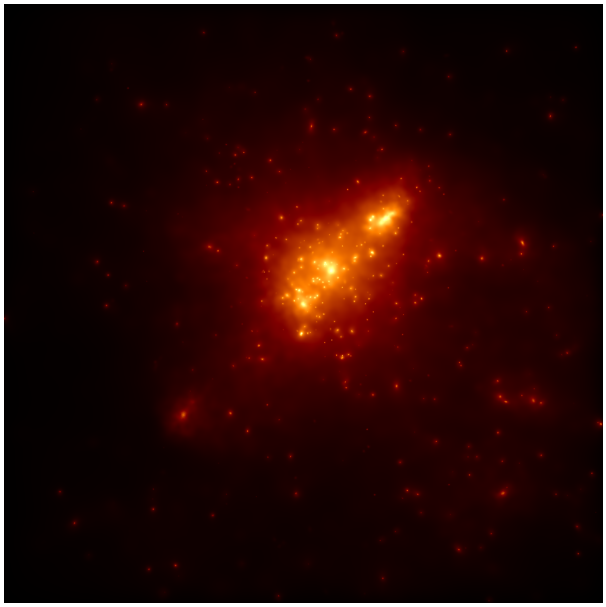

Figure 2.2: Mass map of a simulated cluster at z = 0.37

From the projected mass map it is possible to calculate the convergence K, according to equation 1.45 and the two components of the reduced deflection angle, simply as the gradient of the cluster projected potential (equation 1.44), which produces the maps displayed in Figure 2.3. This procedure can be done with virtually any mass distribution.

2.1.3 Simulation

Once all the inputs are specified, the code is ready to perform the simulation. The first thing to do is reading the input file, including the name of the telescope, necessary to prepare the mock observation

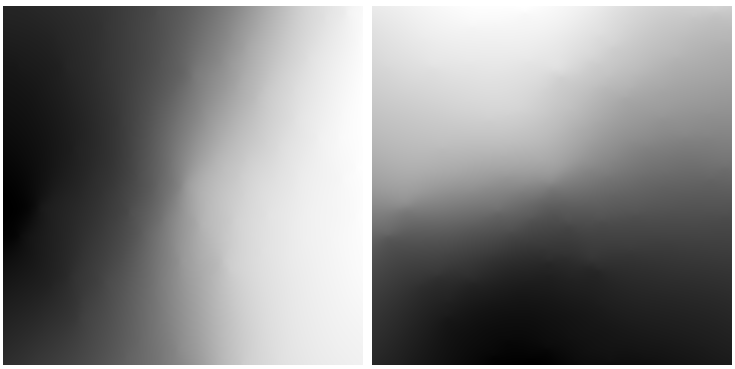

Figure 2.3: Deflection angle of the simulated cluster, considering a source plane at $z_s = 2$

according the instrument considered.
The source catalog is imported and the galaxy templates are stored in memory and galaxies are constructed as explained in the previous section. At this point Skylens builds a given number of planes, read from the input file, between redshifts z=0 and z=12 according to the scaling of the lensing distance $D = \frac{D_{LS} D_L}{D_S}$ with redshift (Figure 2.4).

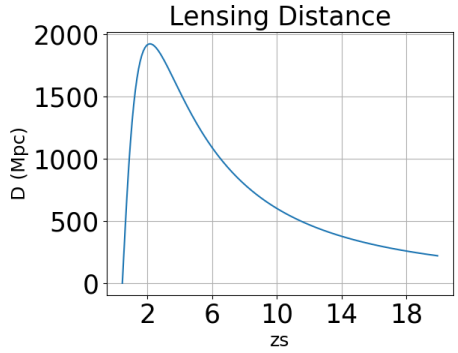

Figure 2.4: Lensing distance as a function of redshift of the source plane

Planes are constructed in a way that their redshift sampling is denser where D is higher. A typical value of 100 planes has been usually utilized, creating as many redshift bins. Sources in each bin are placed on the proper plane and are processed by a ray-tracing algorithm: light rays are traced from the observer, i.e. the detector of the telescope, to each source plane. This means that these rays have to travel around the deflecting cluster, so that they are displaced according to the deflection along the line of sight, which is properly rescaled by a factor $\frac{D_{LS}}{D_S}$, based on the deflection angle and the redshift of each single source plane. This allows to map each source plane onto the image plane by means of its own reduced

deflection angle, simply by using the lens equation (1.41). One of the most recent introductions in Skylens is the possibility to make simulations with multiple deflectors along the line of sight. In this case it is necessary to consider multiple lens planes and calculate the displacement as

$$\vec{\beta} = \vec{\theta} - \sum_{i=1}^{N_L} \vec{\alpha}_i(\vec{\theta}) \tag{2.3}$$

where N_L is the number of deflectors. At this point each single source is ready to be deflected. The first output is an image containing only the lensed sources, convolved with the PSF. The latter is also added to a background noise in order to create a proper mock observation: this is the second output of SkyLens. An example is shown in Figure 2.5.
A useful tool is the so called *only sample shear* mode: this allows to calculate the reduced shear $g = \dfrac{\gamma}{1-\kappa}$ at the image position of each source, obtained from the position of the source and its relative displacement field. The result is a text file containing the identification number, positions, reduced shear, redshift and magnitude of each galaxy.

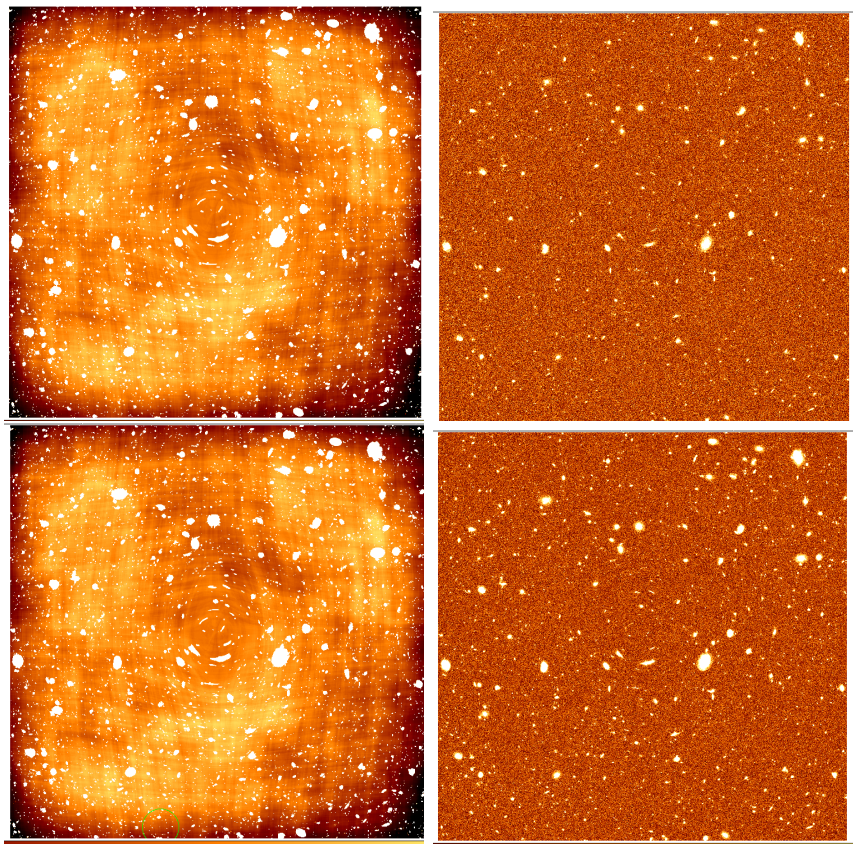

Figure 2.5: These panels show a mock observation produced with SkyLens of the same field of view with Euclid (VIS) in the first row and HST (f814w) in the second row. The images on the left side contain only the simulated lensed galaxies, while the addition of noise has been done in the images on the right side

2.2 KSB method

The **Kaiser Squires Broadhurst** (*KSB*, Kaiser et al. 1994 [45]) approach is an algorithm that allows to estimate the shear signal, considering the effect of the total PSF on galaxy shapes. The idea is simple: the image of the galaxy is processed by the deflector (e.g. a galaxy cluster), which causes a first shear distortion. The images are then modified by the atmosphere and the interaction with the telescope optics, they are pixelated and can be saturated: all these effects cause distortions that have to be corrected in order to reconstruct the pure gravitational shear. Figure 2.6 shows this process.

The KSB method takes into consideration both instrumental and seeing effects. It is based on the assumption that the PSF can be described by a dominant isotropic component and a less significant anisotropic

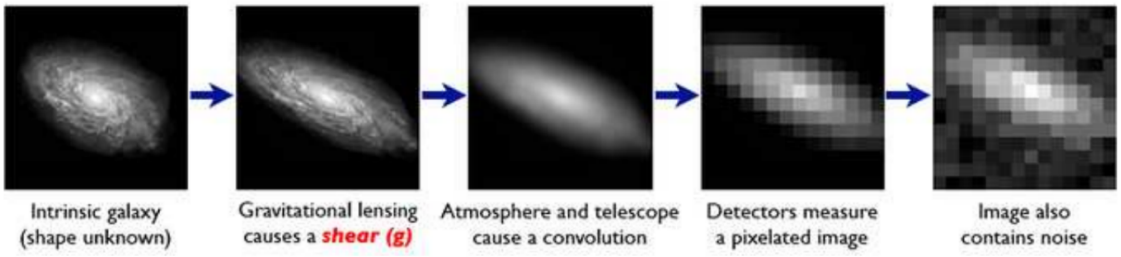

Figure 2.6: Path of a background galaxy image from its unknown intrinsic shape to the one detected by a ground based telescope

component, both of them have to be corrected. The atmosphere generally introduces a smearing in the image, an effect that depends on the size of the source. On the other hand, a camera distortion produces a shear, which depends on the shape of the object. The procedure that was followed in this thesis is similar to the one described in Radovich et al. (2015) [46]. The KSB algorithm is based in the following quantities: e_{obs}, the observed ellipticity of the source and two tensors: the *smear polarizability* P^{sm} and the *shear polarizability* P^{sh}, which are calculated for every source. The first one considers a contribution on the observed ellipticity due to a PSF anisotropic component $\delta e_\alpha = P^{sm}_{\alpha\beta} p_\beta$, where p_β measures the PSF anisotropy; similarly, the second one accounts for an isotropic distortion caused by the response to a gravitational field $\delta e_\alpha = P^{sh}_{\alpha\beta} g_\beta$. They are defined as

$$
\begin{aligned}
P^{sh}_{\alpha\beta} &= \chi^{sh}_{\alpha\beta} - e_\alpha e^{sh}_\beta \\
\chi^{sh}_{\alpha\beta} &= \frac{1}{I_{11}+I_{22}} \int d^2\theta \begin{bmatrix} 2W\theta^2 + 2W'(\theta_1^2-\theta_2^2) & 4W'(\theta_1^2-\theta_2^2)\theta_1\theta_2 \\ 4W'(\theta_1^2-\theta_2^2)\theta_1\theta_2 & 2W\theta^2 + 8W'\theta_1\theta_2 \end{bmatrix} f(\theta) \\
e^{sh}_\alpha &= 2e_\alpha + \frac{2}{I_{11}+I_{22}} \int d^2\theta \begin{bmatrix} \theta_1^2-\theta_2^2 \\ 2\theta_1\theta_2 \end{bmatrix} W'\theta^2 f(\theta) \\
P^{sm}_{\alpha\beta} &= \chi^{sm}_{\alpha\beta} - e_\alpha e^{sm}_\beta \\
\chi^{sm}_{\alpha\beta} &= \frac{1}{I_{11}+I_{22}} \int d^2\theta \begin{bmatrix} W + 2W'\theta^2 + W''(\theta_1^2-\theta_2^2) & 2W''(\theta_1^2-\theta_2^2)\theta_1\theta_2 \\ 2W''(\theta_1^2-\theta_2^2)\theta_1\theta_2 & W + 2W'\theta^2 + 4W''\theta_1^2\theta_2^2 \end{bmatrix} f(\theta) \\
e^{sm}_\alpha &= \frac{1}{I_{11}+I_{22}} \int d^2\theta \begin{bmatrix} \theta_1^2-\theta_2^2 \\ 2\theta_1\theta 2W'\theta^2 f(\theta) \end{bmatrix} (2W' + W''\theta^2) f(\theta) \qquad (2.4)
\end{aligned}
$$

An extended explanation of these tensors can be found in Hoekstra et al. (1998) [48]. It is convenient to utilize the same weight function W (see equation 1.64) for both the objects that have to be corrected and the PSF estimate: this is usually a gaussian function, which allows to suppress sky noise at the edge of each galaxy in the quadrupole moment calculation.
The ellipticity e_{obs} is calculated by means of the brightness moments tensor, as shown in the first chapter (equation 1.66). The PSF correction is performed using stars: they are used as a PSF estimator, given the fact that they should be pure points, so observing their profile basically results in a PSF evaluation. The anisotropic component is calculated according to

$$\begin{aligned} e_{aniso} &= e_{obs} - P^{sm}p \\ p &= e^*_{obs} - \frac{e^*_{obs}}{P^{sm*}} \end{aligned} \tag{2.5}$$

where starred terms refer to stars measurements. The term e_{aniso} can be written as the sum of two components: the intrinsic ellipticity of the source, which is unknown in principle, and the reduced shear, utilizing the *pre-seeing shear polarizability* P^γ, which was introduced by Luppino and Kaiser (1997) [47] and corrects the isotropic part of the PSF, given mainly by the atmospheric seeing.

$$\begin{aligned} e_{aniso} &= e + P^\gamma e_{iso} \\ P^\gamma &= P^{sh} - P^{sm}\frac{P^{sh*}}{P^{sm*}} \end{aligned} \tag{2.6}$$

Now, considering the fact that averaging over a very large number of galaxies the intrinsic ellipticity will average to zero $< e > = 0$, from equation 2.6 it is possible to obtain an estimation of the shear signal, which has been cleaned from spurious contributions.

$$\begin{aligned} e_{iso} &= \frac{e_{aniso}}{P^\gamma} \\ g &= e_{iso} \end{aligned} \tag{2.7}$$

This is the output of the KSB algorithm: the shear signal given only by the gravitational fields of the deflector. Note that if P^{γ} ends up being very small, it is possible to obtain values of $e_{iso} > 1$, which does not make sense; so only values such that $e^2_{iso1} + e^2_{iso2} < 1$ are taken into consideration.
From the two shear components it is possible to obtain the tangential and cross components of the shear, according to the fact that the shear is a tensor with spin 2.

$$\begin{aligned} g_t &= -g_1 cos(2\phi) - g_2 sin(2\phi) \\ g_x &= -g_1 sin(2\phi) + g_2 cos(2\phi) \end{aligned} \tag{2.8}$$

where ϕ is the position of each source on the sky plane with respect to the cluster center. In fact, it is very important to identify the cluster center as well as possible in this type of analysis.

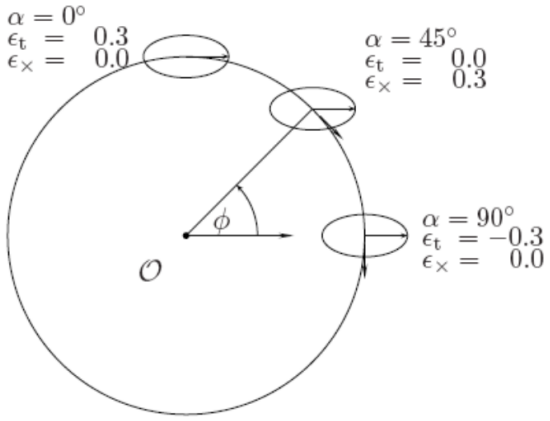

Figure 2.7: Tangential and cross component of the shear

Given the definition 2.8 a positive tangential component g_t refers to an image which is tangentially magnified, while a negative tangential components corresponds to a radially distorted image. This is clear looking at Figure 2.7. Since gravitational lensing is an effect that can be described by a scalar potential (equation 1.43), it is curl free: this means that the cross component g_x should average to zero, which provides a check for the correctness of the analysis.

2.2.1 Object selection

In order to apply the KSB method correctly it is very important to distinguish and select specific objects:

- separate stars from galaxies
- select only galaxies located behind the cluster

The first step is necessary to implement the algorithm explained in the previous section and use stars to estimate the PSF contribution on the total ellipticity of a source. It can be done by means of a two parameters diagram $(M; \delta)$, as done in Huang et al. (2011) [49]. M is the magnitude of each source measured by the photometry software utilized (e.g. SexTractor), while $\delta = \mu_{max} - M$, where μ_{max} indicates the peak surface brightness of each source. In this context, δ can be used as an estimator of the source size, which allows to separate stars from galaxies. Other times the radius containing 50% of the total source flux is used as a size estimator: this quantity can be obtained from FLUX RADIUS, an output parameter of Sextractor. This allows to define also the size of the window function W used to do ellipticity measures, in order to suppress the outer parts of each galaxy. It is possible to define the ellipticity signal to noise ratio as

$$SNe(\theta) = \frac{\int I(\theta)W(\theta)d^2\theta}{\sigma_{sky}\sqrt{\int W^2(\theta)d^2\theta}} \tag{2.9}$$

It is common to consider only sources with $SNe(\theta) > 5$ for ellipticity measures, since under this threshold the parameter FLUX RADIUS starts to shrink, which translates in a less meaningful shape estimate.
Moreover, obviously only galaxies behind the cluster are lensed. Averaging over a sample of galaxies that also contains foreground sources would cause a dilution of the shear signal. Therefore, it is necessary to assign to each galaxy its proper redshift and analyze only the ones with $z > z_{lens}$. This is obviously straightforward when photometric redshifts are available, but if it is not the case, another method is proposed by Formicola et al. (2014) [50]: the separation can be done considering the CC (color-color) diagram, when photometric data is on tap in at least three filters. This method uses COSMOS galaxies and their position in the CC space as a training set for the sample under study. Data in 30 filters that span

from UV to IR are available. A specific line is individuated on the CC diagram: the tangent to the ellipse containing 20% of the total foreground sources, parallel to the ellipse major axis. The distance from this line $d = \frac{a + col1 + col2 + c}{\sqrt{a^2 + 1}}$ separates foreground ($d > 0$) and background galaxies ($d < 0$). An example is shown in Figure 2.8.

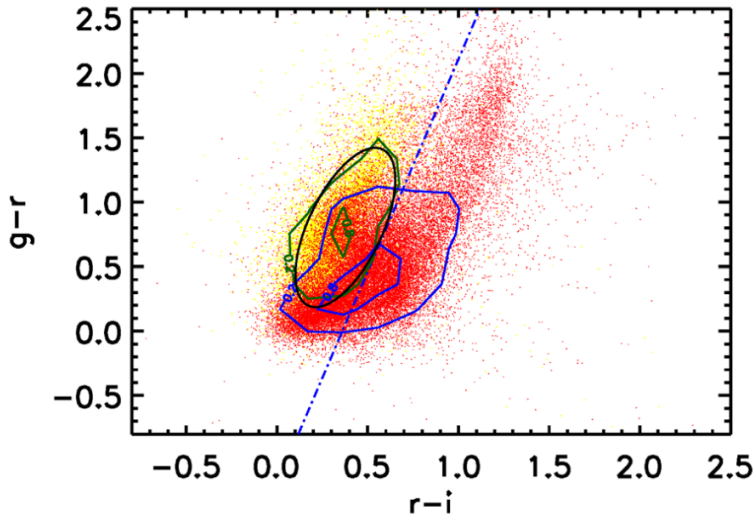

Figure 2.8: CC diagram of the COSMOS sample [50]: galaxies are separated between foreground (yellow dots) and background (red dots), as well as by the blue line, corresponding to a first estimate of d(a,c). Number density contours are represented by the green and blue lines, respectively

A magnitude error threshold is chosen: if uncertainties are too big, the color of a source is not reliable: these galaxies are treated as background sources. At this point an iterative process begins: the coefficients a, c are chosen as the ones that maximize the shear signal (equation 2.8): a new selection of background sources is performed, considering the distance d as a function of these new coefficients $d(a_n, c_n)$. A check of the goodness of the analysis is provided by g_t of the foreground sources and g_x of the background galaxies, which should both average to zero.

2.3 Code testing

Before proceeding with the explanation of the main results of this work, I had to make sure that the simulations were performed correctly. For this task, I took into consideration an analytical lens, so that it is possible to know in principle the expected position of the images and verify whether the galaxies in the mock observation are placed where expected or not. In particular I considered a so called pseudo elliptical lens, with a core term, in order to describe a lens without singularities. This lens is described by a lensing potential (see equation 1.43):

$$\Psi(\vec{x}) \;=\; \sqrt{x_1^2 + f^2 x_2^2 + x_c^2} \tag{2.10}$$

where f is responsible for the introduction of an ellipticity in the lens potential, as shown in Figure 2.9, while x_c is the core term, which allows the potential not to go to zero for $(x_1, x_2) = (0, 0)$. The deflection angle is computed as the gradient of the lens potential (equation 1.44).

I built a model using a source with a *Sersic* surface brightness profile [51]:

$$\begin{aligned} I(R) \;&=\; I_0 exp\left[-b_n\left(\frac{r}{r_e}\right)^{1/n}\right] \\ b_n \;&\sim 1.99n - 0.33 \end{aligned} \tag{2.11}$$

where $n \sim 4$ for old elliptical galaxies, while $n \sim 1$ for spiral galaxies. The source was placed between the radial and the tangential caustics, which translates in three multiple images of the source, as shown in Figure 2.10.

I run a simulation with SkyLens, using a single source identified in the *UDF* as explained in the previous section and placing it at the same position of the source in Figure 2.10. The result is shown in Figure 2.11.

Note how the blue dots in Figure 2.11 (i.e. the positions of the multiple images) match the positions of the multiple images in the model shown in Figure 2.10. This is a confirmation that SkyLens is performing the simulations correctly.

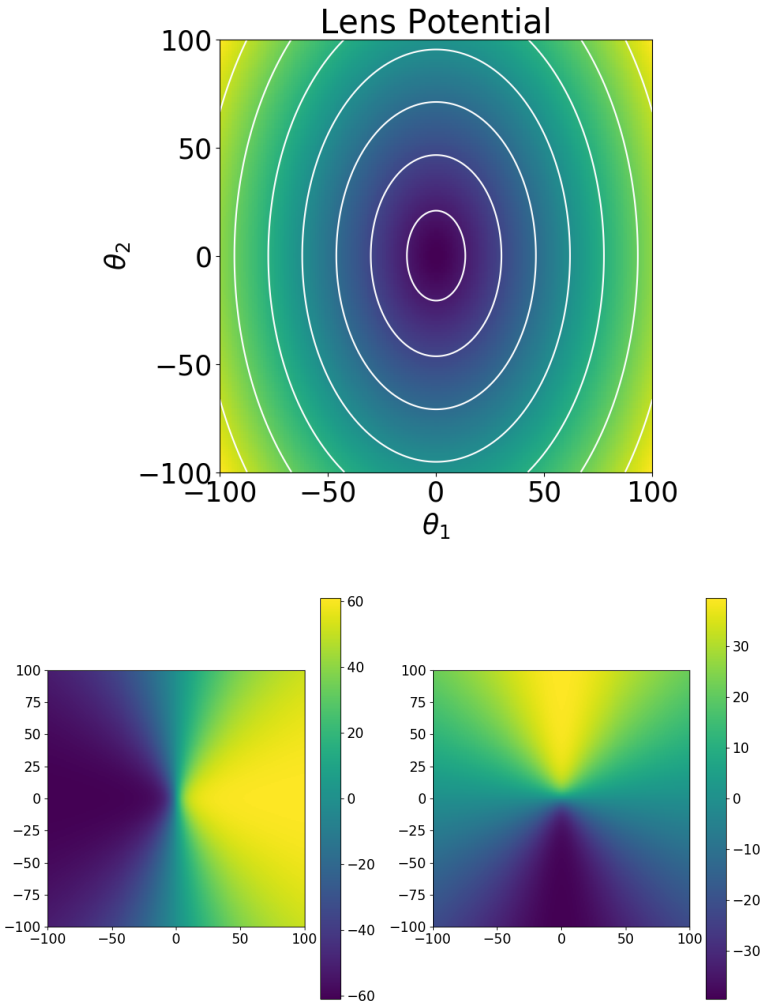

Figure 2.9: Lens potential with its level contours for a lens with $f = 0.35$ and $x_c = 3$ (first panel) and its deflection angle (second panel)

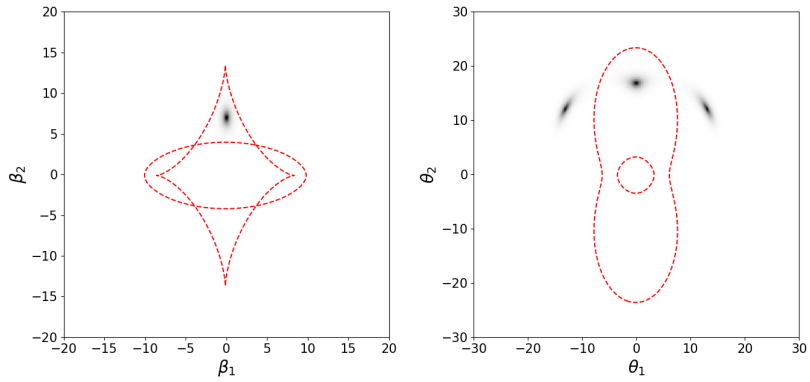

Figure 2.10: Caustic lines with the source on the source plane (first panel), critical lines with multiple images on the image plan (second panel)

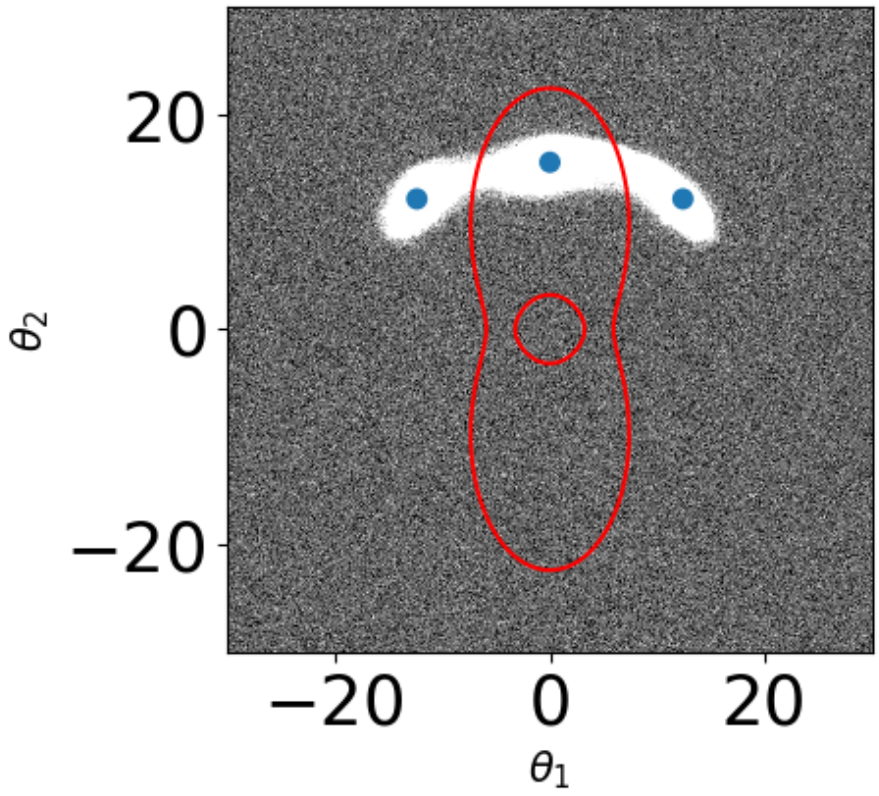

Figure 2.11: Mock observation created using one single galaxy, at the same position of the model, with an analytical lens as a deflector. The three blue dots identify the location where multiple images of the same source have been placed by SkyLens

Chapter 3

Data Elaboration

This chapter will collect the results of my thesis work. First of all I worked on the galaxy cluster **MACS J1206**, running simulations with its deflection angle maps and putting the simulated galaxies in different types of noise. These images have been analyzed using a KSB pipeline, in order to obtain the shear profile of this cluster, which has been compared to an expected model. Moreover, an estimate of the cluster mass was obtained from this profile.
This type of testing has been repeated on simulations with MACS J1206 as a deflector, but with different filters and also on two simulated clusters, called Ares and Hera. A complete description of the whole work is given in the following sections.
I chose to perform the whole data analysis in Python, mainly because of its simplicity as a programming language, as well as its many third part modules developed for data elaboration and astrophysics in general, such as *numpy*, *astropy*, *scipy* and *lmfit*.

3.1 MACS J1206

MACS J1206 is a galaxy cluster, located around 4.5 billion light years away from the Earth, at redshift $z = 0.439$. It has been observed with different telescopes, in 2011 it was analyzed by Hubble Space Telescope as a part of the Cluster Lensing and Supernova survey (CLASH). Its coordinates are $RA = 12^h06^m12.2^s$ and $DEC = -08°48'01''$ in the *J2000* reference frame.

First of all, I collected a set of various observations of this cluster with

Figure 3.1: HST color composite picture of MACS J1206. Lensing effects such as gravitational arcs are clearly visible and 47 multiple images of 12 background galaxies have been identified. Credits to NASA, ESA, M. Postman (STScI) and the CLASH Team

band (Å)	**exposure**	**Zeropoint**	**program**
R_C (6288.71)	2900 s	23.95	S03B-UH51A
B (4458.32)	2400 s	23.13	Umetsu09
V (5477.83)	2200 s	23.59	Ebeling09
I_C (7683.88)	3600 s	23.72	UH-30A, Ebeling09
Z (9036.88)	1600 s	23.51	UH-30A

Table 3.1: Set of Subaru observations of MACS J1206

the Subaru Telescope, spanning from 2003 to 2009, taken by the Supreme Cam, as part of different observing programs. They are necessary because one of my main purposes was inserting the simulated galaxies in real observations of this cluster.

These are all broad band filters, centered in the wavelengths reported in Table 3.1, their transmission is shown in Figure 3.2. The images are coadded mosaics, covering a total field of view of $36' \times 24'$, with a pixelization of 0.2 $\frac{arcsec}{pixel}$.

Figure 3.3 shows the image in the R_C band. The center of this image is not aligned with the BCG, this is an important aspect that has been taken into consideration in my analysis.

In order to perform a simulation using this cluster as a deflector, I exploited the software **LensTool**, see Jullo and Kneib (2009) [52], which was elaborated at *Laboratoire d'Astrophysique de Marseille* (LAM). It

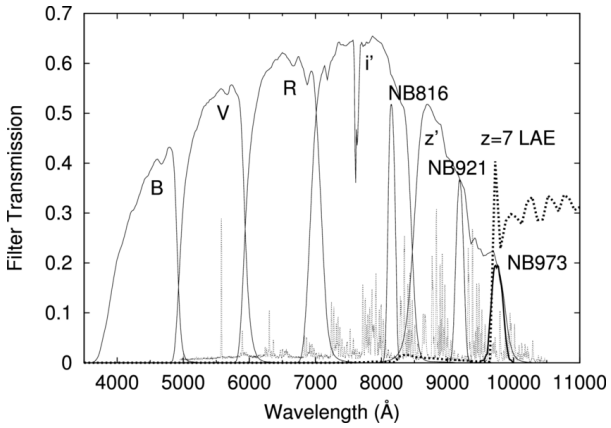

Figure 3.2: Subaru Supreme Cam Filters used in this study, along with other intermediate band filters

allows to model mass distributions of galaxies and clusters in general, using both strong and weak lensing constraints. I utilized a model of the cluster potential constructed by *Carminha et al.* (2017) [53], which is basically a combination of different Pseudo Isothermal Mass Distribution (*PIEMD*), whose density and convergence profiles are described by equation 3.1.

$$\begin{aligned} \rho(r) &= \frac{\rho_0}{(1+\frac{r^2}{a^2})(1+\frac{r^2}{s^2})} \\ \kappa(R) &= \frac{\sigma_0^2}{2G}\frac{s}{s-a}\Big(\frac{1}{\sqrt{R^2+a^2}} - \frac{1}{\sqrt{R^2+s^2}}\Big) \end{aligned} \tag{3.1}$$

where a is the core radius, s is the truncation radius. Note that this profile is built in a way that for $a < r < s$, the density profile is isothermal $\rho(r) \propto r^{-2}$. A proper isothermal density profile would describe a mass distribution that behaves like a perfect gas in equilibrium, both thermal and hydrostatic, in a gravitational potential with spherical symmetry and can be written as

$$\rho(r) = \frac{\sigma_v^2}{2\pi G r^2} \tag{3.2}$$

A crucial step of my work was making sure that the cluster center in the simulations was aligned with the observations. In order to do this, I checked the pixel shift between the center of the observed image and the center of the BCG, both along the x and y axis, obtaining a difference of $(-189px, -17px)$. Given the fact a single pixel covers $0.2''$, the respective shift is given by $(-37.8'', -3.4'')$.

A weak lensing analysis requires the possibility to consider galaxies located

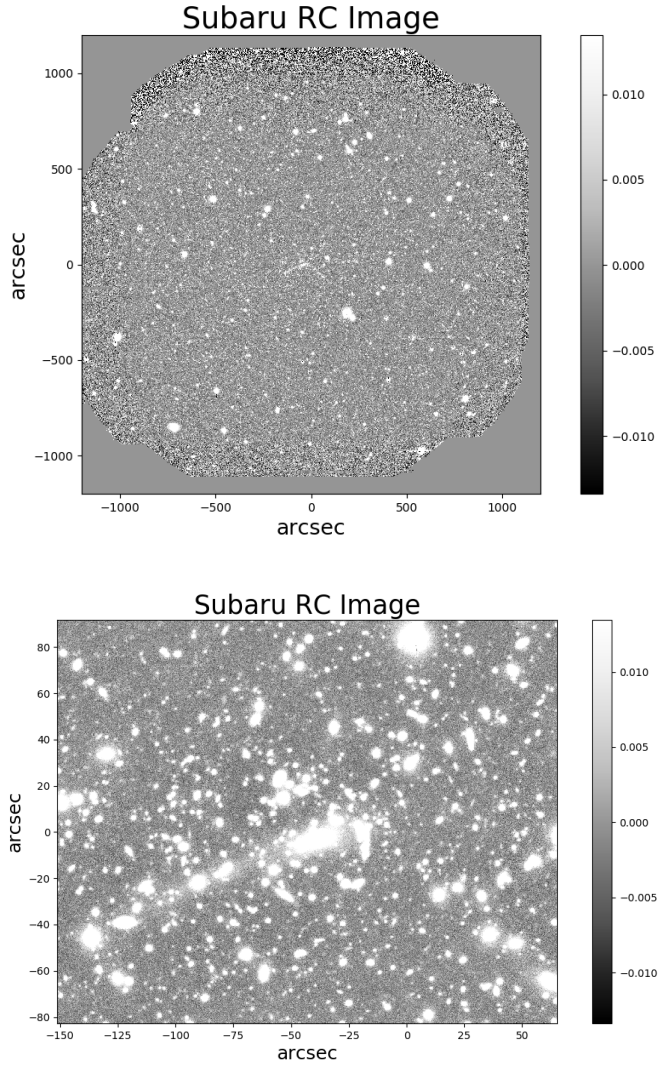

Figure 3.3: R_C image of MACS 1206 shown in its full extension (upper) and zoomed in the central part (lower). The colorbar indicates the counts/sec

far away from the cluster center. Because of this, I performed simulations with a FOV of 1800×1800 $arcsec^2$. In order to make sure that the alignment was properly done, I set the field limits in LensTool as

$$X_{MIN} = -862.2'' \quad X_{MAX} = 937.8''$$
$$Y_{MIN} = -896.6'' \quad Y_{MAX} = 903.4''$$

Running LensTool under these conditions allowed me to obtain the convergence map (calculated according to equation 1.45) of MACS J1206, with a side of $2048px$. A source redshift value of $z_s = 2$ was considered to

build this map and every other model map in the following pages. The result is shown in Figure 3.4.

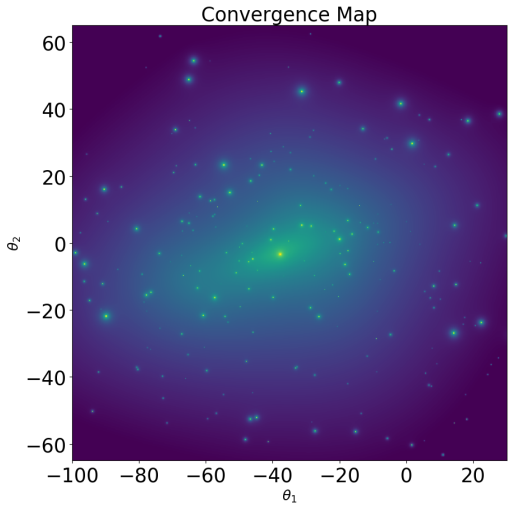

Figure 3.4: Central zoom of the convergence map of MACS J1206 obtained from LensTool, for $z_s = 2$. The colormap is in logarithmic scale and covers values between 0.1 and 3.0

From this convergence map, I was able to obtain the two components of the deflection angle thanks to equation 1.39, which links the surface mass density (i.e. the convergence) to the deflection angle. In the real space this is a convolution, so that in the Fourier space it is a simple multiplication, which can be written as

$$\vec{\tilde{\alpha}}(\vec{k}) \;=\; \frac{1}{\pi}\tilde{\kappa}(\vec{k})\vec{\tilde{K}}(\vec{k}) \tag{3.3}$$

where $\tilde{\kappa}(\vec{k})$ is the Fourier transform of the convergence and $\vec{\tilde{K}}(\vec{k})$ is the Fourier transform of the so called called Kernel function $\vec{K}(\vec{x}) = \dfrac{\vec{x}}{|\vec{x}|^2}$. This operation in the Fourier space is straightforward using the Python package **fft** from *numpy*. The result is shown in Figure 3.5.

After different attempts of completing a simulation deep enough to allow the analysis of a significant number of sources and also given the values of the zeropoint in Table 3.1, I chose a magnitude limit of 27 for the simulated sources, which are distributed in a squared field with 30 arcmin side, which was also basically the limit of the calculating power that I had available. Under these conditions, the number of sources which has been processed by SkyLens is around 120000, in the R_C band, which is the image I mostly worked on.

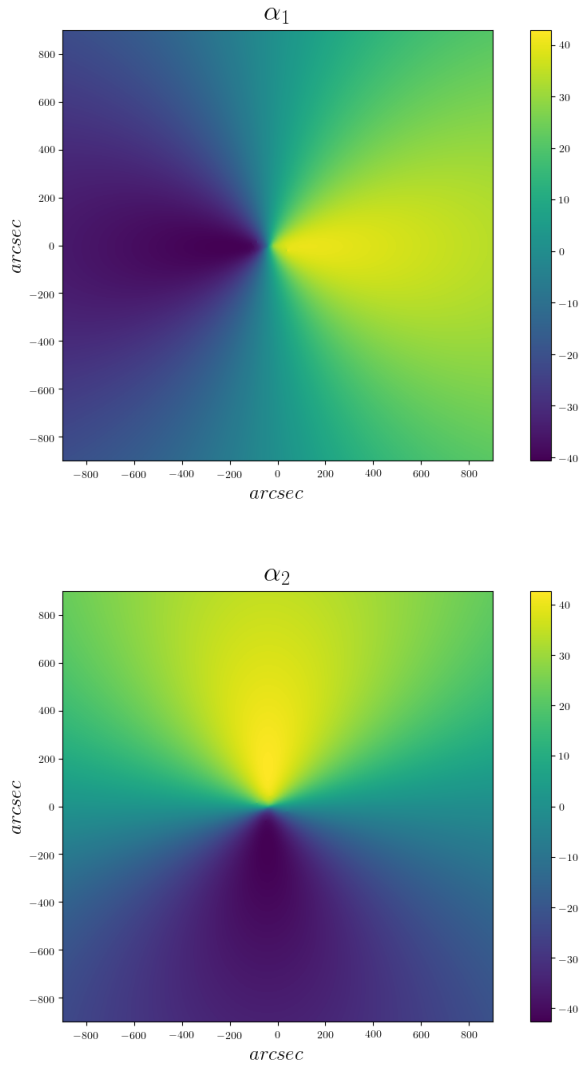

Figure 3.5: Deflection angle α_1 and α_2 for MACS J1206

3.1.1 MACS J1206 in the R_C band

As previously outlined, I included three different types of noise in the simulations, from which I obtained three distinct images to analyze, one for each type of noise. All of them contain the same simulated galaxies, but noise is different.

- Observation Noise: simulated sources were stacked over the real observation of the cluster
- Poisson Noise: noise is purely given by a poissonian count which is comparable to the noise of the real observation
- SkyLens Noise: noise introduced directly by SkyLens, as explained

in chapter 2

Let's get into the detail of the noise production, especially in the first two cases. In the first case, I worked with two initial images: the one containing the simulated galaxies without any type of noise and the real observation (Figure 3.3). For both of them, each pixel has a side of $0.2''$ on the sky plane, but the first one has a side of $1800''$, so that it consists of a square image of 9000×9000 px^2, while the second one has some empty boundary pixels, making it a 12000×12000 px^2 image. It is crucial that the central pixels of the two images coincide. Another point of emphasis was making sure that I used a proper common scale: SkyLens produces an image with total counts in each pixels, while the observation is given in counts per second, so before summing the two, I divided the counts from the mock image by the respective integration time (in this case $2900s$). This whole procedure allows to put simulated galaxies in a real noise, which also contains the intra-cluster light (ICL). This is simply done by adding pixel by pixel the mock image containing only the simulated sources to the real observation.
As for the second case, noise was created artificially: the first step consisted in analyzing the real observation of the galaxy cluster, considering around 50 areas, spread over the whole FOV and small enough to have no sources inside them (I ended up working with zones of about 100 $arcsec^2$), and measuring the counts per second in each of these zones. For this task I used the software SAO Image ds9, an application that allows image and data visualization, it works with files in format *fits* (Flexible Image Transport System), the most common file format in astronomy and astrophysics. A review of ds9 can be found in Joey and Mandel (2003) [54].
I considered the median of all these measures per unit area as the typical noise value in the image. At this point, in each pixel of the simulated image I added a random count number extracted from the Poisson distribution

$$P_\lambda(n) = \frac{\lambda^n}{n!} e^{-\lambda} \tag{3.4}$$

which is, in general, the probability to obtain a certain number n of discrete events given an expected value of λ. In this case λ is exactly the typical noise value previously obtained. I did this using the Python function *random.poisson* from numpy, which directly draws samples from a

Poisson distribution. The images that have been taken into consideration, are shown in Figure 3.6.

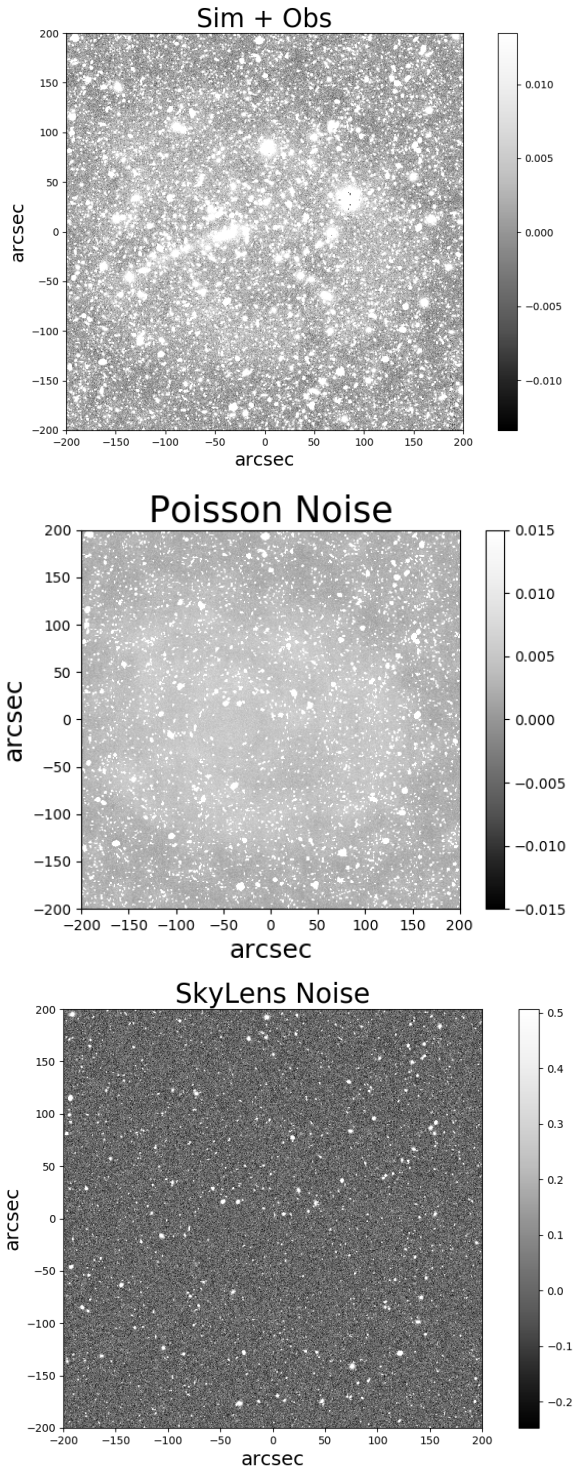

Figure 3.6: Images with different types of noise: images show simulated galaxies immersed in a real observation (first panel), simulated galaxies surrounded by a Poisson noise (second panel) and surrounded by the noise introduced by SkyLens (third panel). All images are zoomed in the central 400″

These images are the true starting point of the KSB analysis.
I also considered the critical lines of this deflector: from the convergence map obtained with LensTool and the deflection angle calculated as previously explained, the determinant of the Jacobian was calculated as

$$det(A) = (1 - \frac{d\alpha_1}{dx})(1 - \frac{d\alpha_2}{dy}) - \frac{d\alpha_1}{dy}\frac{d\alpha_2}{dx} \tag{3.5}$$

Since the critical lines identify the points with ideally infinite magnification, they can be viewed as the zero levels contours of the determinant of the Jacobian, this is straightforward looking at equation 1.53. The critical lines are plotted over the image with both simulated galaxies and real objects in Figure 3.7.

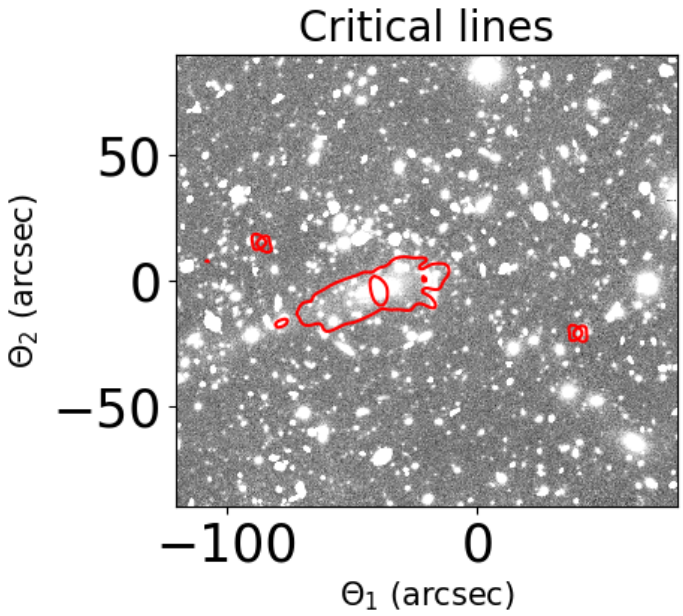

Figure 3.7: Critical lines of MACS J1206 plotted over its real observation with the addition of simulated galaxies

This is a typical configuration with a central radial critical line and a surrounding tangential critical line, which provides a confirmation that the deflector was built correctly.

3.2 KSB implementation

The KSB analysis, explained in Chapter 2, was carried out with a couple of precautions: the ellipticity was measured only on the simulated objects and the PSF that has been used to perform the simulations was also used to implement the KSB method. Because of this, there was no need to separate stars from galaxies in order to estimate the PSF contribution. So, the first thing that has to be done is detecting the objects. For this task, I used the software *Sextractor*, a program that extracts a catalog of sources from an astronomical image.

3.2.1 Sextractor

The software *Source Extractor* is ideal to make photometry measurements on all detected objects in a large astronomical image. It works well with CCD type of data, it is fast and is able to deal with large fits files. It has some limitations, like accuracy: output parameters are usually calculated from moments and not fitted, which would be more precise. Moreover, it tends to break down in crowded fields, but for my purposes it is the best solution.
Sextractor follows a series of steps:

- Measure of the background
- Detection of the objects over a given threshold
- Measure shape and positions of these objects
- Clean each source measurement, considering contributions from close sources
- Perform photometry and write the results in the output catalog

A detailed descriptions of these steps can be found in the Sextractor manual [55], there are also multiple options available, as Figure 3.8 shows.

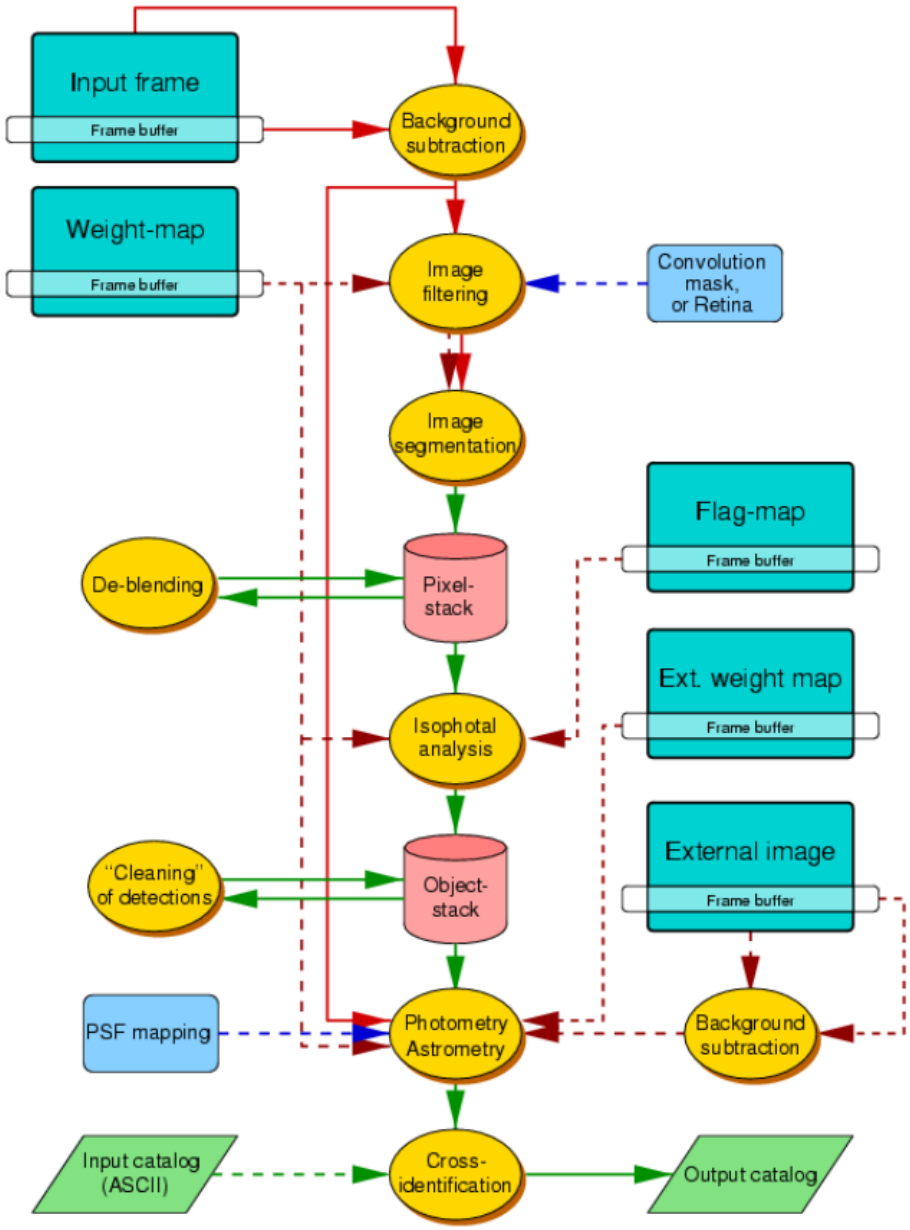

Figure 3.8: Complete algorithm of a Sextractor run. It is possible to give different weights to specific pixels, or even flag some of them, as well as comparing the output catalog with another one. There is the possibility to deblend objects, distinguish between one single object and different sources really close to each other

A very useful characteristic of Sextractor, is the possibility to use it in dual mode: this means detecting the sources on one image and make photometry measurements on another one. This is perfect for this work, in fact I made the source detection on the simulated image without noise and then made the other quantitative measures on the specific image under analysis. This allowed me to be sure that the analysis was done

only on the simulated galaxies, especially in the case of the image with both real and mock objects, where a direct source detection on the image would have included also real observed galaxies. Obviously, the images have to be well aligned for this task to work successfully.
Sextractor makes measurements according to a specific configuration file, which basically contains what has to be analyzed and how to do it. It needs some specific parameters, that are usually read from the header of the fits file, like the *gain*, i.e. the number of electrons that are converted into a digital count, or the magnitude zero-point of the image.
One of the most crucial steps is the background estimate. I calculated it in circular areas with a diameter of 64 pixels, a standard input value for this parameter. Sextractor computes the mean counts in that area and the standard deviation, rejects extreme values and repeats the process until every pixel has counts within a $\pm$ 3 σ range. This background estimate is fundamental, because sources are then recognized according to a specific threshold, which is a multiple of the variance of the background value. I used a 1.5σ threshold value. I also considered a gaussian filter in order to suppress counts at the boundary of each source.
After detection, Sextractor performs photometry. In this phase initial parameters are used: gain is used to convert counts into flux and the magnitude zero-point for calibration. Different isophotes are individuated according to the pixels above the threshold and aperture photometry is performed: counts are numbered inside regions of 2.5, 5, 10, 20, 40 pixels.
The results are written in the output catalog, which contains the number of objects detected with their own position, their magnitude, their size (according to the parameter FLUX RADIUS) and the factors a, b that describe the ellipticity of each source, according to

$$\begin{aligned} \frac{x^2}{a^2} + \frac{y^2}{b^2} &= 1 \\ \epsilon &= \frac{a-b}{a+b} \end{aligned} \tag{3.6}$$

as well as the angle θ that describes its orientation with respect to the x-axis. These are computed from the objects second order moments.
This concludes the source detection on the images.

3.2.2 Ellipticity analysis

At this point, the objects catalog is ready to be processed by the actual KSB pipeline (Radovich et al. [46], Huang et al. [49]). This procedure was done in python language as well. First of all, galaxies were further selected according to a magnitude cut, with values of $mag_l = 14$ and $mag_u = 26$, and a signal to noise ratio cut, which means that only sources with $\frac{S}{N} > 5$ were considered for the analysis, in order to consider only meaningful sources for the shear estimate. Each source is analyzed according to its centroid and its size determined by Sextractor. The procedure follows the explanation of the KSB method in section 2.2, with the exception that there is no need to estimate the PSF, so the procedure is done simply by working directly on the PSF image. Everything is done utilizing three functions:

- **ksb**: the first one implements the equations in Hoekstra et al. [48], calculating the smear and shear polarizabilty tensors P^{sm} and P^{sh}, given a certain image, its centroid, its size and the noise surrounding it

- **ecorr**: the second function basically applies equations 2.6 and 2.7 on a single source, given the tensors calculated by *ksb*

- **getell**: the third and last function uses the first two, in order to apply the correction to each source, calculating P^{sm}, P^{sh} and P^{γ} directly on each source and on the PSF image

So finally, the output of this algorithm is e_{iso}, an estimate of the ellipticity contribution on each source only due to the gravitational field of the deflecting galaxy cluster, or, to explain better, the observed ellipticity cleaned from every possible PSF distortion. In fact, note that on the single galaxy there is still the contribution of its intrinsic ellipticity, which will vanish only averaging over the total number of sources in different radial bins, which is the next step of the work.

3.3 Catalog analysis

The output catalog of the KSB implementation is basically a text file with specific data of each source: its position, flux, magnitude and initial

observed ellipticity, all coming from the Sextractor run. Moreover, there are the four different components of the tensors P^{sh} and P^{sm}, along with the values of P^{γ}, e_{aniso} and most importantly the two components of e_{iso}. This part of the analysis was performed in Python as well.
First of all, I read the two components of e_{iso} and the galaxy positions from the output catalog of the KSB algorithm. After that, the cluster center was located as the central pixel of the BCG. This was done exploiting previous astrometric calibrations, so that the cluster positions is known to be in

$$\begin{aligned} RA &= 12h\ 06m\ 12.15s \\ DEC &= -8d\ 48m\ 03.37s \end{aligned} \tag{3.7}$$

In the observations with a side of 12000 px these coordinates were identified at pixels ($X_C = 5811$, $Y_C = 5983$), which translates in a position of ($X_C = 4311$, $Y_C = 4483$) in the simulated images with side of 9000 px. Figure 3.9 shows this matching.

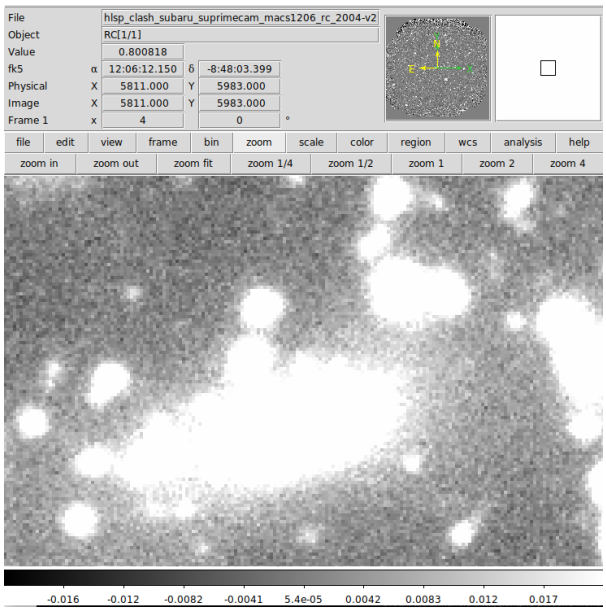

Figure 3.9: Identification of the cluster center in a ds9 panel. Note the matching between the coordinates in right ascension and declination with pixels

Only sources with $\sqrt{e1_{iso}^2 + e2_{iso}^2} < 1$ have been selected. I calculated the distance from the cluster center and the angle with respect to it for

each galaxy as

$$\begin{aligned} d &= \sqrt{(x - X_C)^2 + (y - Y_C)^2} \\ \theta &= arctan\left(\frac{y - Y_C}{x - X_C}\right) \end{aligned} \tag{3.8}$$

The distance value was multiplied by 0.2 $arcsec/px$ in order to transform it from a distance in pixels to a distance in arc-seconds.
Now, consider the fact that I had the Lenstool model of MACS J1206 available, which allowed me to create its convergence map and also its shear maps, from which it is possible to obtain the true model for its reduced tangential shear profile, according to equation 2.8. These maps were created for a source redshift $z_s = 2$, so in foresight of a future comparison between the model obtained from Lenstool and the profiles obtained from different images, it is necessary to rescale the shear signal of each galaxy to $z_s = 2$. For this task, I took advantage of the *only sample shear* mode of SkyLens, in order to have a catalog with each galaxy position, the reduced shear of that position and the source redshift. Working with this data allows me to understand what SkyLens is seeing as an input. It is possible to rescale the shear signal according to

$$g(z_{s_0}) = \frac{d_s}{d_{ls}} \frac{d_{ls_0}}{d_{s_0}} g(z_s) \tag{3.9}$$

where $z_{s0} = 2$, z_s is the single source redshift and the relative distance factors are indicated accordingly. Each distance is calculated as an angular distance (see equation 1.10), as is commonly done in lensing analysis. Considering the cosmological parameters of this work, values of $z_{s0} = 2$ and $z_l = 0.439$ translate in corresponding distances of $d_l = 1193.8 Mpc$ $d_{ls} = 1252.8 Mpc$ and $d_s = 1825.4 Mpc$.
In principle it is not difficult to apply equation 3.9, since each quantity is given in the catalog, but this is very useful because it allows to know where each source is and it is possible to compare these positions with the ones found by Sextractor. This gives the possibility to track each source also in the simulated images and assign them their own redshift. This is crucial in order to rescale the shear signal of each source to $z_s = 2$. An important correction that had to be taken was considering not the exact redshift of each galaxy, but the redshift of the plane where the source was placed by SkyLens. This is fundamental, because the code calculates the

reduced deflection angle and performs the displacement (equation 1.41) according to the redshift of the source plane.

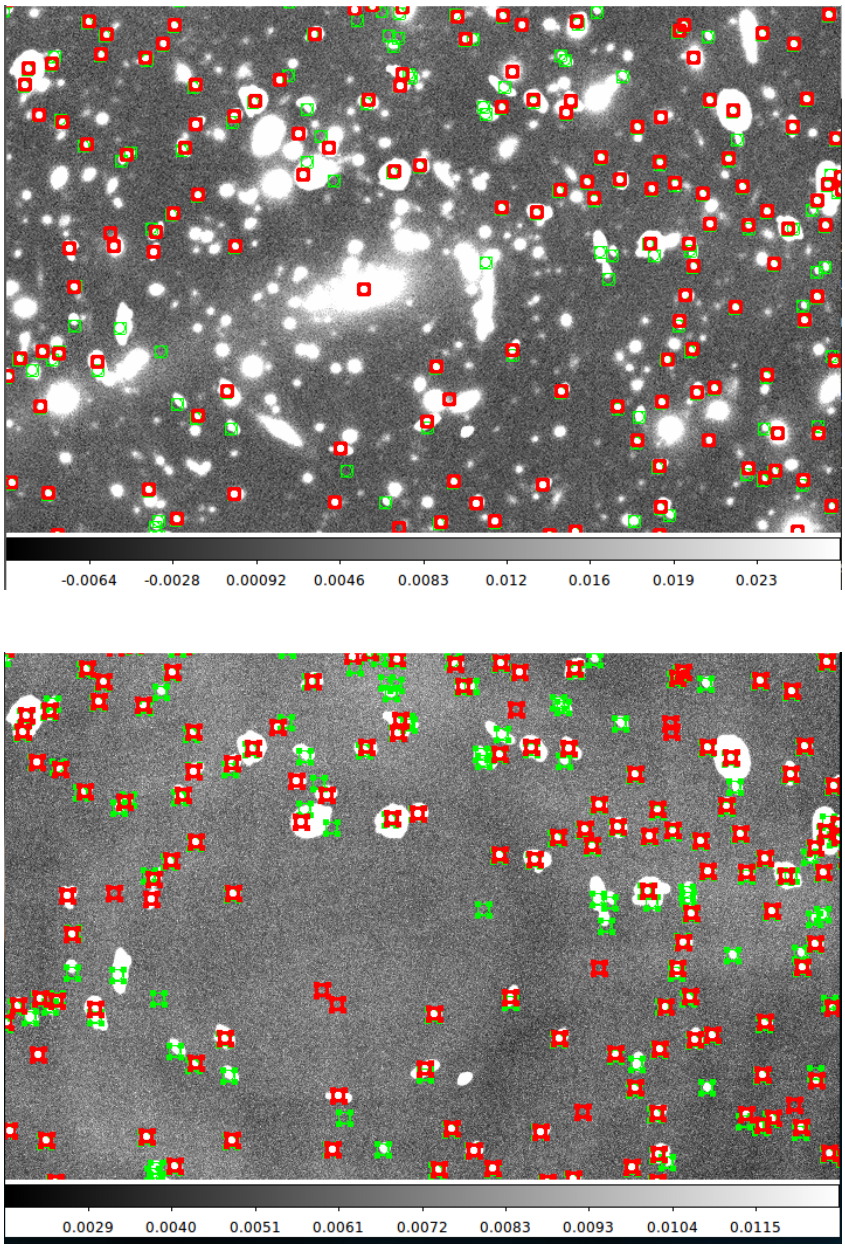

Figure 3.10: Match between different galaxy catalogs: simulated sources detected in the real observation (first panel) and in the Poisson noise (second panel) are shown in red, while galaxies positions calculated by SkyLens are represented in green

In order to match galaxies between two different catalogs, I checked where both the x coordinate and the y coordinate had a difference which is smaller than 2 pixels and assigned the proper redshift to each galaxy. I had to cope with some data loss. In fact, the position obtained from SkyLens is not exactly the same of the centroids individuated by Sextractor. This

means that some of the galaxies were not recognized. Moreover, there were some double matches, when two galaxies are really close to each other. I was able to count these matches and exclude them from my analysis. I did not consider these losses significant though, because the percentage of sources lost was always under 10% with respect to the total number of galaxies analyzed.
At this point, I had a list of sources with their distance from the cluster center, their relative angle, their ellipticity and redshift of the plane used to process them. Applying equations 2.8 and 3.9 it is straightforward to obtain the reduced tangential and cross-component shear for each galaxy. Then, the radial bins analysis comes into place. I created different numbers of radial bins, between 6 and 9 for different images studied, in order to average on at least 100 galaxies in each bin, especially for the inner most bin. I worked with logarithmic distances, in order to have more sources closer to the cluster center. I assigned each galaxy to its proper radial bin and calculated the average shear components with their relative standard deviation in each bin as

$$\begin{aligned} g_T(i) &= \frac{\sum_{j=0}^{k} g_t(j)}{k} \\ g_X(i) &= \frac{\sum_{j=0}^{k} g_x(j)}{k} \\ \hat{\sigma_T^2}(i) &= \frac{\sum_{j=0}^{k} (g_t(j) - g_t(i))^2}{k} \\ \hat{\sigma_X^2}(i) &= \frac{\sum_{j=0}^{k} (g_x(j) - g_x(i))^2}{k} \end{aligned} \tag{3.10}$$

where the index i refers to a single bin, the index j to each galaxy in a specific bin and k is the total number of sources in a single bin. I calculated the dispersion of shear values as

$$\sigma = \frac{\sqrt{\hat{\sigma^2}}}{\sqrt{N}} \tag{3.11}$$

with N being the total number of galaxies in each bin. This concludes the procedure to obtain tangential and cross-component shear estimate with the KSB algorithm.

3.3.1 Lenstool Model

The model of MACS J1206 allowed me to build its convergence map (Figure 3.4) as well the two components of its shear (equation 1.50), which are shown in Figure 3.11.

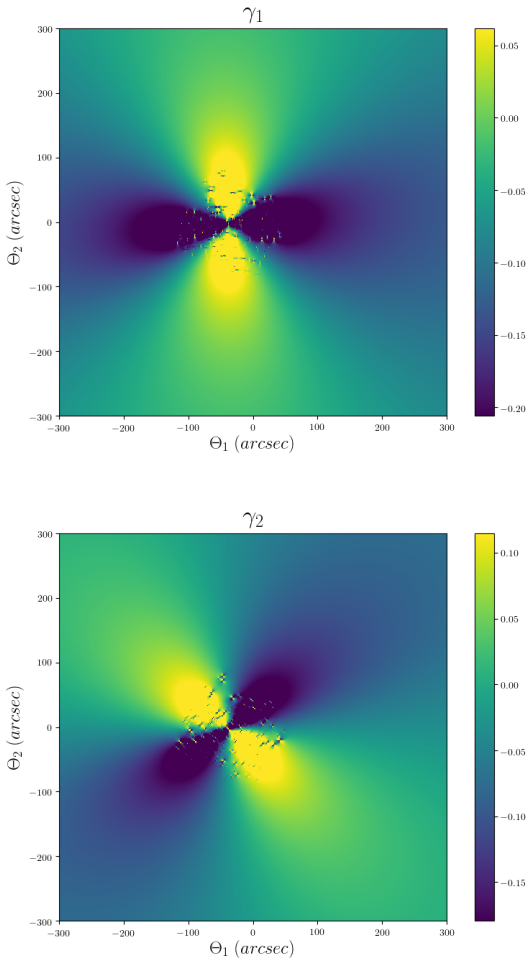

Figure 3.11: Shear maps of MACS J1206 obtained with lenstool, zoomed in the central 600″

With these maps, I calculated the reduced shear in each pixels and, following to the procedure explained in the previous section, I obtained the model profiles for both the tangential and cross component of the shear, shown in Figure 3.12.

The cross component is null, according to the fact that shear is curl free, while the tangential component increases towards the cluster center under its gravitational presence. I considered every shear profile obtained from the analysis of different images related to this model. The following table 3.2 summarizes the results.

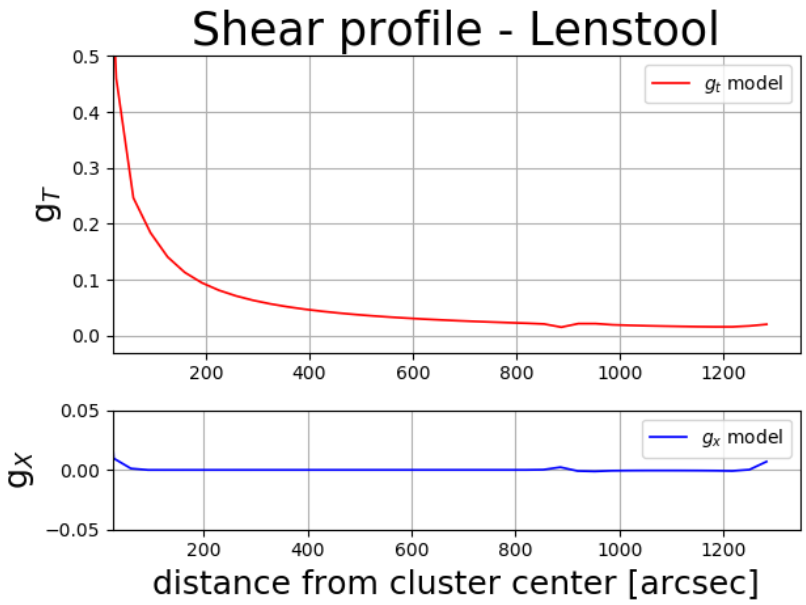

Figure 3.12: Tangential and cross component of the shear of MACS J1206, obtained elaborating convergence and shear maps from Lenstool

Image	N galaxies	N matches
Sim + Obs	87637	70043
Poisson	88277	70857
Noisy	38498	31028
SkyLens	102465	-

Table 3.2: Number of galaxies in different simulated images

The fourth line in Table 3.2 does not properly refer to an image, it rather refers to the catalog obtained with the *only sample shear* mode, so it contains every galaxy that has been simulated. The other three are the ones shown in Figure 3.6. Note that the number of sources is generally lower with respect to the total number of the simulated ones, this happens because the more faint galaxies disappear under the noise. In fact, the number of sources in the image with both real and simulated objects is similar to the Poisson noise image, where noise was created accordingly to the real observation. On the other hand, the image with noise added from SkyLens contains significantly less galaxies, an indication that this type of noise is not comparable with the one from the real observation, as opposed to the Poisson image case.

These profiles were compared to the model of MACS J1206, obtained with Lenstool in Figure 3.12.

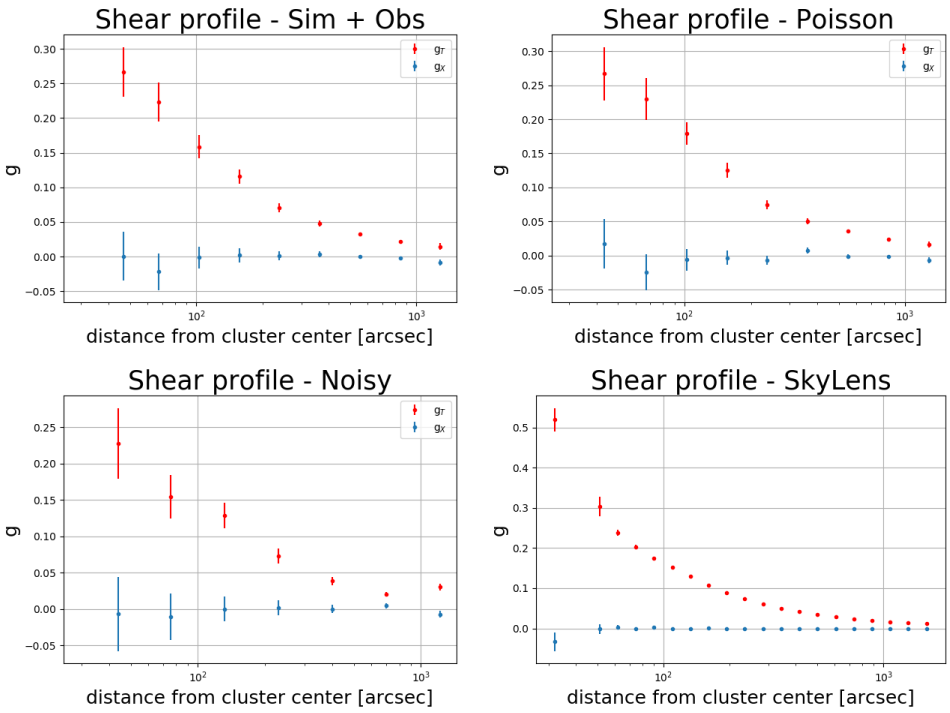

Figure 3.13: Shear profiles obtained from KSB analysis of different images

First of all, note how the shear measured from SkyLens follows the model. Both the image with simulated and real galaxies and the one built with Poisson noise seem to reproduce the model well. This is not the case for the image with noise introduced directly by SkyLens, which underestimates the shear profile primarily towards the cluster center. This is probably caused by the noise itself. The initial value of ellipticity is measured from brightness moments of each source, so if especially the outer parts of the galaxies are overwhelmed by noise, the ellipticity measure will be biased.

In order to work with a more quantitative comparison, I built a reduced χ^2 function for each g_T profile with respect to the model $\bar{g_T}$.

$$\chi^2_R = \frac{\sum_{i=0}^{n}(g_T(i) - \bar{g_T})^2}{\sigma^2_T(i)} \frac{1}{n} \tag{3.12}$$

where n is the total number of data points available of each profile (i.e. the number of bins) and the index i ranges over the whole dataset. The χ^2 test is usually adopted to compare a certain set of data to a model obtained by fitting that specific set of data, which is not what happens in this case. Nonetheless, it is a good indicator of how much each set of data

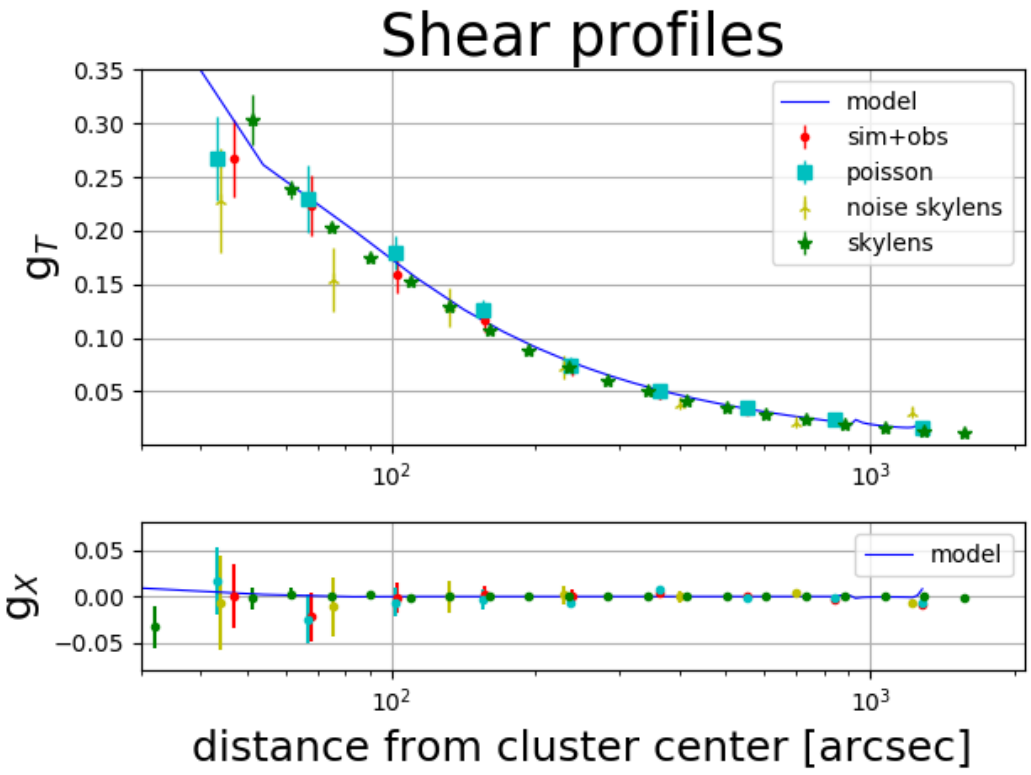

Figure 3.14: Different shear profiles compared to the Lenstool model

deviates from the expected model, in units of the standard deviation of each point. In fact, if the error is dominated by a statistical contribution, which is intrinsic to the measurement process, it is reasonable to expect a difference of 1 σ between data and model, if measures distribute in a gaussian way around a mean expected value. This means that each data point should contribute to the total χ^2 with a value of 1. Dividing the final result by the total number of data point, should give a final $\chi^2_R \sim 1$. Bigger values of χ^2_R reflects a bad agreement between data and model. This model profile is not an analytical function, it derives from pixelated maps (Figure 3.11). So, in order to obtain a proper $\bar{g_T}$ value to compare to my data, I considered the model values corresponding to the index with smaller difference between the distance arrays of the KSB data and the model itself.

These χ^2_R values simply confirm the previous evaluation, the image with noise introduced by SkyLens does not reproduce the Lenstool model correctly, while the other two images seem to carry out the task, validating this type of analysis.

Image	χ^2_R
Sim + Obs	0.79
Poisson	0.74
Noisy	2.53

Table 3.3: Reduced χ^2 values for different shear profiles

3.4 Cluster Mass Estimate

The basic idea to obtain the cluster mass is considering a Navarro-Frenk-White (NFW, equation 1.62) density profile and check how different shear profiles reproduce it.

3.4.1 Theoretic approach

It is possible to rewrite this profile as a function of two specific parameters: the halo scale radius r_s and its concentration c

$$\rho(r) = \frac{\delta_c \rho_c}{\frac{r}{r_s}(1+\frac{r}{r_s})^2} \tag{3.13}$$

where $\rho_c = \frac{3H^2(z)}{8\pi G}$ is the critical density of the universe (see equation 1.12) and $\delta_c = \frac{200}{3}\frac{c^3}{ln\,(1+c) - \frac{c}{1+c}}$ is the characteristic overdensity of the halo. The scale radius r_s and the concentration c are also linked by the virial radius $r_{vir} = r_s c$. The virial radius is often interpreted as the radius inside which the mean mass density of the halo is equal to $200\rho_c$, so it is common to refer to the virial radius as $r_{200} = r_s c$.
In order to obtain the total mass of the cluster, it is necessary to integrate the density profile (equation 3.13). It is common to integrate from the cluster center up to the virial radius r_{vir}, in this case the cluster mass is

$$M = \int_0^{r_{vir}} 4\pi r^2 \rho(r) dr = 4\pi \delta_c \rho_c r_s^3 \left[ln\,(1+c) - \left(\frac{c}{1+c}\right)\right] \tag{3.14}$$

In order to work with shear data it is necessary to infer the tangential shear profile of a NFW halo mass distribution. I followed the same procedure explained by Wright et al. (2000) [56]. The convergence can be calculated from the 2D projection of the surface density

$$\Sigma(R) = 2\int_0^\infty \rho(r,z)dz$$

$$\Sigma_{NFW}(x) = \begin{cases} \frac{2r_s\delta_c\rho_c}{x^2-1}\left[1-\frac{2}{\sqrt{1-x^2}}arctanh\sqrt{\frac{1-x}{1+x}}\right] & \text{if } x<1 \\ \frac{2r_s\delta_c\rho_c}{3} & \text{if } x=1 \\ \frac{2r_s\delta_c\rho_c}{x^2-1}\left[1-\frac{2}{\sqrt{x^2-1}}arctan\sqrt{\frac{x-1}{1+x}}\right] & \text{if } x>1 \end{cases} \tag{3.15}$$

where $x = \frac{R}{r_s}$ is called dimensionless radius. Given the fact that the NFW profile has spherical symmetry, it is possible to write the radial trend of the shear as

$$\gamma_{NFW} = \frac{\bar{\Sigma}_{NFW}(x) - \Sigma_{NFW}(x)}{\Sigma_C} \tag{3.16}$$

where Σ_C is the critical surface density and $\bar{\Sigma}_{NFW}(x)$ is the mean surface mass density inside x and is calculated as $\bar{\Sigma}_{NFW}(x) = \frac{2}{x^2}\int_0^x x'\Sigma_{NFW}(x')dx'$, the result is

$$\bar{\Sigma}_{NFW}(x) = \begin{cases} \frac{4}{x^2}r_s\delta_c\rho_c\left[\frac{2}{\sqrt{1-x^2}}arctanh\sqrt{\frac{1-x}{1+x}}+ln\left(\frac{x}{2}\right)\right] & \text{if } x<1 \\ 4r_s\delta_c\rho_c\left[1+ln\left(\frac{1}{2}\right)\right] & \text{if } x=1 \\ \frac{4}{x^2}r_s\delta_c\rho_c\left[\frac{2}{\sqrt{x^2-1}}arctan\sqrt{\frac{x-1}{1+x}}+ln\left(\frac{x}{2}\right)\right] & \text{if } x>1 \end{cases} \tag{3.17}$$

Combining equations 3.16 and 3.17 it possible to finally get the tangential shear component of a NFW mass distribution

$$g_T(x) = \begin{cases} \frac{r_s\delta_c\rho_c}{\Sigma_c}g_<(x), & \text{if } x<1 \\ \frac{r_s\delta_c\rho_c}{\Sigma_c}\left[\frac{10}{3}+4\ln\left(\frac{1}{2}\right)\right], & \text{if } x=1 \\ \frac{r_s\delta_c\rho_c}{\Sigma_c}g_>(x), & \text{if } x>1 \end{cases} \tag{3.18}$$

where the functions $g<(x)$ and $g>(x)$ only depend on the dimen-

sionless radius x and do not depend on cosmology. They are defined as

$$\begin{aligned} g_<(x) &= \frac{8\ arctanh\sqrt{(1-x)/(1+x)}}{x^2\sqrt{1-x^2}} + \frac{4}{x^2} ln\left(\frac{x}{2}\right) \\ &- \frac{2}{x^2-1} + \frac{4arctanh\sqrt{(1-x)/(1+x)}}{(x^2-1)(1-x^2)^{\frac{1}{2}}} \\ g_>(x) &= \frac{8\ arctan\sqrt{(x-1)/(1+x)}}{x^2\sqrt{x^2-1}} + \frac{4}{x^2} ln\left(\frac{x}{2}\right) \\ &- \frac{2}{x^2-1} + \frac{4\ arctan\sqrt{(x-1)/(1+x)}}{(x^2-1)^{\frac{3}{2}}} \end{aligned} \tag{3.19}$$

So the first comparison that has been considered in order to get an estimate of the cluster mass was the one between different shear profiles g_T obtained in the previous section and a NFW profile $g_{T,NFW}$ (equation 3.18).
A second condition utilized involves the Einstein radius (equation 1.59), with the exception that for an extended mass distribution, it involves only the mass inside it and not the total mass of the lens

$$\theta_E = \sqrt{\frac{4GM(<\theta_E)}{c^2}\frac{D_{LS}}{D_L D_S}} \tag{3.20}$$

The overall procedure is similar to the one applied by Umetsu et al. (2012) [57], who also worked on MACS J1206. The mass inside the Einstein radius, necessary to carry out equation 3.20, for a NFW halo can be obtained integrating 3.13 from the cluster center to the Einstein radius.

$$M(<r_E) = \int_0^{r_E} 4\pi r^2 \rho(r) dr = 4\pi\delta_c\rho_c r_s^3 \left[ln\left(\frac{r_s+r_E}{r_s}\right) - \frac{r_E}{r_s+r_E}\right] \tag{3.21}$$

where $r_E = \theta_E D_L$, with D_L being the distance of the lens from the observer.
The Einstein radius can also be thought as the tangential critical line (equation 1.54). One way to consider a characteristic value of the Einstein radius is measuring the area inside the critical line A_C, i.e. the *critical area* and then calculate the effective Einstein radius as

$$\theta_E = \sqrt{\frac{A_C}{\pi}} \tag{3.22}$$

A similar approach was taken by Zitrin et al. (2012) [61]. So it is possible to compare the Einstein radius $\theta_{E,NFW}$ calculated from equation 3.20 with θ_E obtained from checking where $1 - K - \gamma = 0$. I considered an uncertainty value of $\sigma_{\theta_E} = 2''$ on the Einstein radius estimate.
So the final goal is to minimize the residual

$$\chi^2_T = \chi^2_{WL} + \chi^2_{SL} = \sqrt{\frac{(g_T - g_{T,NFW})^2}{\sigma^2_T} + \frac{(\theta_E - \theta_{E,NFW})^2}{\sigma^2_{\theta_E}}} \tag{3.23}$$

For this task I used the Python package *lmfit*, aimed at minimizing 3.23. This package allows to face non linear least squares cases thanks to complex fitting models. The method used to minimize the residual is *Nelder-Mead*, also known as downhill simplex method (Nelder and Mead (1965) [58]).
Moreover, a Bayesian analysis has been performed in order to obtain the probability distribution function of the two parameters r_s and c. For this task it is necessary to consider a Likelihood function, which basically tells how different sets of parameters are able to reproduce a certain set of observed data according to the Bayes probability theorem, where $P(A|B)$ is the probability that the condition A is verified when B is true, vice versa for $P(B|A)$, while $P(A)$ and $P(B)$ are the probabilities to observe A and B independently.

$$\begin{aligned} P(A|B) &= \frac{P(B|A)P(A)}{P(B)} \\ ln\mathcal{P}(p|d) &= ln\mathcal{L}(d|p) + ln\mathcal{P}(p) \end{aligned} \tag{3.24}$$

so that the probability to have a certain set of parameters p given a set of data d depends on the probability to obtain that data d given the parameters p and the probability that those parameters p can actually fit the data. These terms are referred to as Posterior, Likelyhood and Prior. The Likelyhood function has been built as a gaussian function, so that the logarithmic Likelyhood becomes

$$ln\mathcal{L}(d|p) \;=\; -\frac{1}{2}\sum_{n}\left[\frac{(D_n - M_n)^2}{\sigma_n^2} + ln(2\pi\sigma_n^2)\right] \qquad (3.25)$$

where D_n and M_n are data points and model values calculated at the same distance of data and σ_n^2 are the variance values on each data point. This function has been used to sample the posterior distribution of r_s and c, by means of a *Markov Chain Monte Carlo* approach [59], which assumes a uniform prior $\mathcal{P}(p) \;=\; 0$. For this task, I used the Python package *emcee* [60], which implements this type of approach. The posterior is sampled according to a Markov walk and for each step the Likelyhood is calculated. This allows to locate the point in the parameter space that maximizes the Likelyhood, i.e. the parameters that reproduce the data set at best.

The final result of this analysis is the value of the two parameters r_s, c with their own probability distribution function and uncertainties; which can be used to infer the mass of the cluster, according to 3.14.

3.4.2 Mass values

In order to obtain the θ_E, I calculated the convergence K and the shear $\gamma = \sqrt{\gamma_1^2 + \gamma_2^2}$ maps from the reduced deflection angle of MACS J1206 as

$$\begin{aligned} K &= \frac{1}{2}\left(\frac{d\alpha_1}{dx} + \frac{d\alpha_2}{dy}\right) \\ \gamma_1 &= \frac{1}{2}\left(\frac{d\alpha_1}{dx} - \frac{d\alpha_2}{dy}\right) \\ \gamma_2 &= \frac{d\alpha_1}{dy} \end{aligned} \tag{3.26}$$

With these quantities I obtained a map of $1 - K - \gamma$.

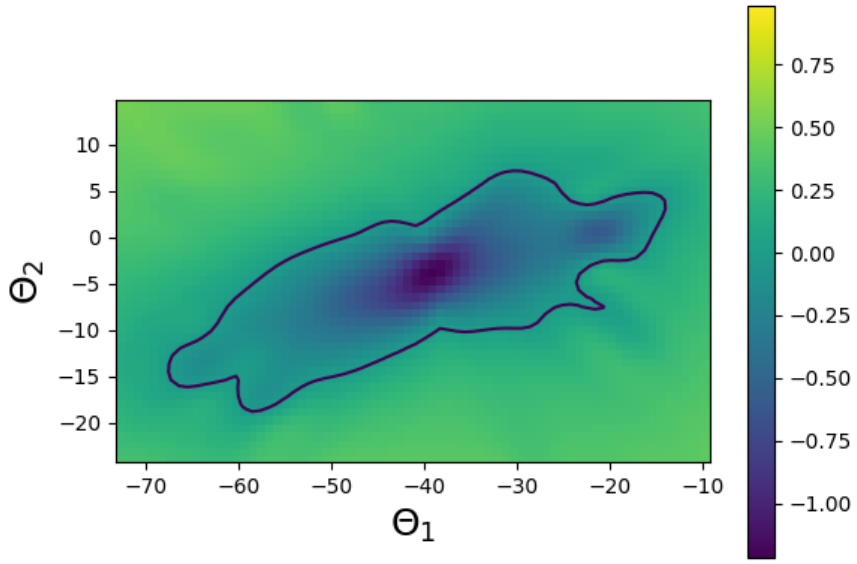

Figure 3.15: 2D map of $1 - K - \gamma$. The blue line identifies its zero level contours. Angles values are in arc-seconds

For the calculation of the critical area, I exploited an application of Green's theorem, which allows to relate the double integral on the area with the closed line integral along the contour of the respective area

$$\int\int_A \left[\frac{df}{dx} - \frac{dg}{dy}\right] dxdy = \int_d (fdy + gdx) \tag{3.27}$$

where f, g are two 2D functions with continuous derivatives. Similarly,

Image	**Mass** $[\frac{M_\odot}{10^{15}}]$	χ^2_R
Sim + Obs	$1.66^{+0.79}_{-0.57}$	1.5
Poisson	$1.88^{+0.99}_{-0.83}$	1.9
Noisy	$1.37^{+1.45}_{-0.77}$	3.3

Table 3.4: Mass values obtained from the analysis of different images

using the vertexes of the contours, it is possible to compute the contour area as

$$A_C = \frac{1}{2}\Sigma\left[y_0 dx - x_0 dy\right] \tag{3.28}$$

where (x_0, y_0) are the coordinates of each vertex and (dx, dy) is the separation between each vertex.
I calculated the effective Einstein radius according to equation 3.22, obtaining a value of $\theta_E = 14'' \pm 2''$, in agreement with uncertainty values of $2'' - 3''$ also estimated in [57]. The results are shown in Figures 3.16 and 3.17 and Table 3.4.

Uncertainties on the Mass values have been calculated according to [62]: given a function of two variables $f(x_1, x_2)$, I calculated f_0 where x_1 and x_2 are equal to the best fit values and then computed $f_1 = f(x_1 + \delta x_1, x_2)$ and $f_2 = f(x_1, x_2 + \delta x_2)$. The final uncertainty value σ_f was obtained from

$$\sigma_f^2 = \sum_i (f_i - f_0)^2 \tag{3.29}$$

It is evident that the image with noise introduced directly by SkyLens is again the more problematic one, just like in the comparison between each shear profile with the expected model (Figure 3.14). Overall, each value in table 3.4 is compatible with mass values obtained by Umetsu et al. [57], which validates this type of analysis to infer the mass of MACS J1206.

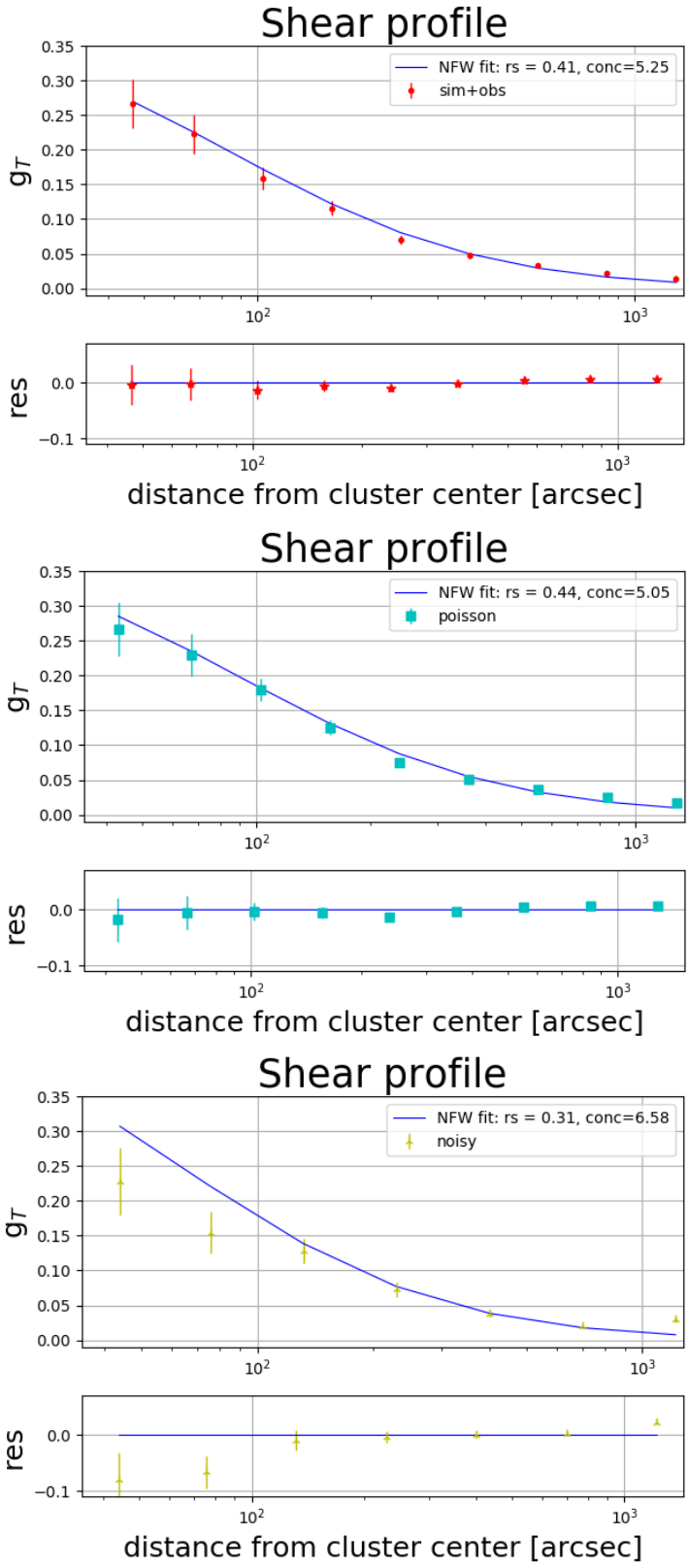

Figure 3.16: Tangential shear profiles with their NFW fit

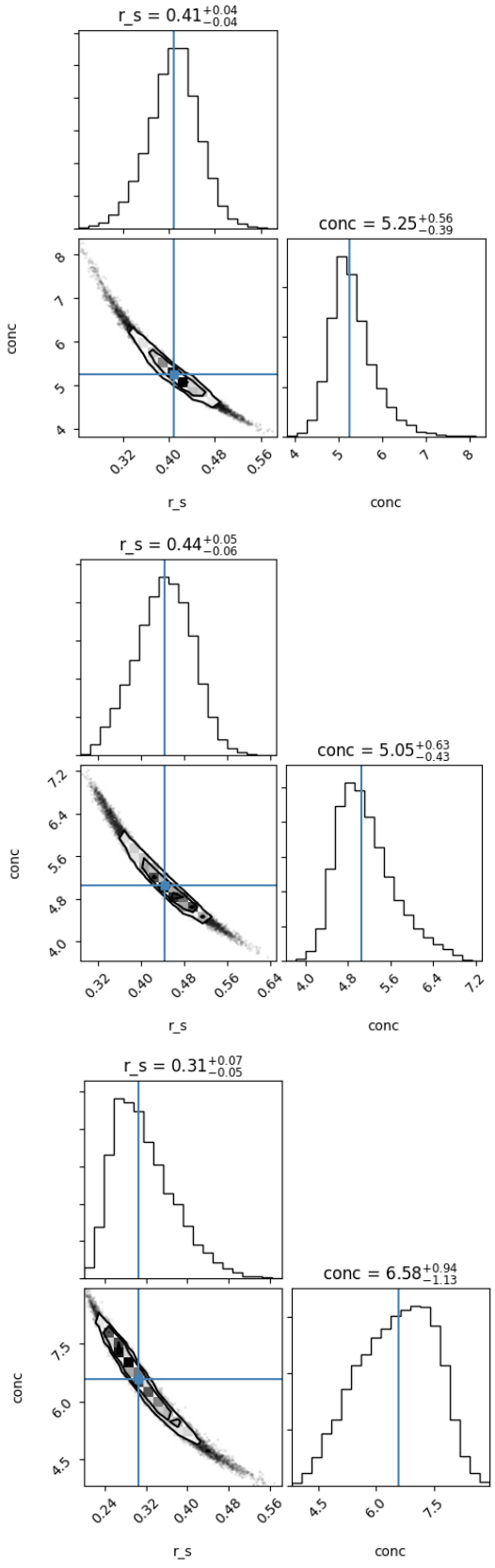

Figure 3.17: PDF of the two parameters scale radius r_s, concentration of the halo c for different images, the contour plots evidence the 1σ and 2σ confidence levels

Chapter 4

Additional clusters

In order to increase the statistics of my results, I performed the same type of analysis explained in the previous chapter on more galaxy clusters. I considered the images in additional filters of MACS J1206 that I had available and two simulated clusters: *Ares* and *Hera*.

4.1 MACS J1206 - Z and I_C bands

The main initial configuration of the following results is the one explained in the previous chapter, since the deflector is always MACS J1206. However, different filters have been used for simulating the observation, each of them with its own associated PSF. Also, the exposure time has been changed according to the one of the real observation (see Table 3.1). The KSB method has been performed on images containing both real and simulated galaxies, shown in Figure 4.1.

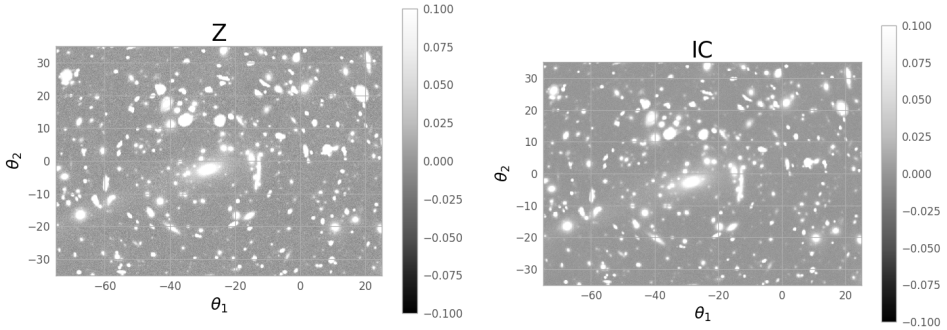

Figure 4.1: Images with both real and mock galaxies in the Z band (first panel) and I_C band (second panel), zoomed in their central parts. The colorbar indicates the photon count per second

Filter	**Mass** $[\frac{M_\odot}{10^{15}}]$	χ^2_R
Z	$0.74^{+0.57}_{-0.48}$	3.1
IC	$1.26^{+0.61}_{-0.45}$	6.5

Table 4.1: Mass values of MACS J1206 analyzing images in different filters

The results of the whole analysis are collected in the following plots and tables.

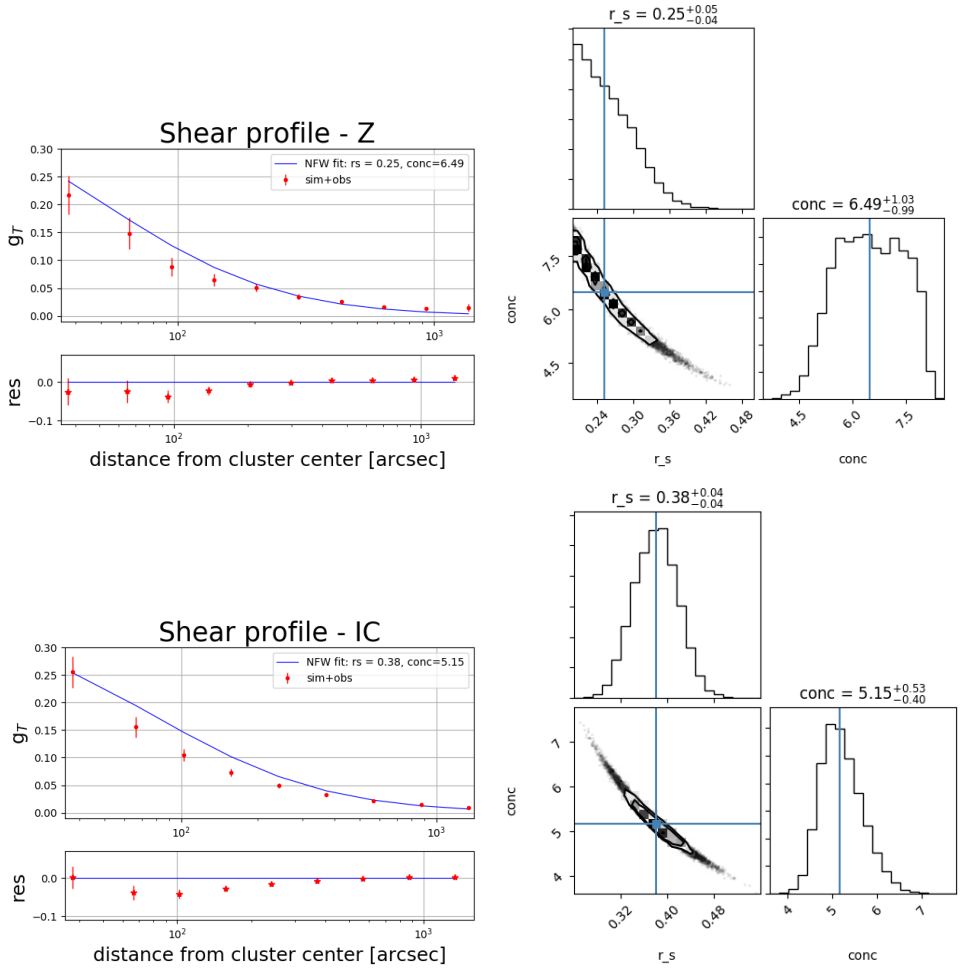

Figure 4.2: Shear profiles of MACS J1206 in different filters with their NFW fit and the best fit parameters

Note that both mass values are compatible with estimates from the R_C band (Table 3.4). The analysis from the Z band tends to estimate a lower value, probably because it is the one with lowest exposure time, 1600 s with respect to 2900 s of the R_C band. This translates in a lower signal to noise ratio, which makes it more difficult to evaluate the outer parts of the sources and the consequent ellipticity measurement.

4.2 Simulated Clusters

Ares and *Hera* are two simulated galaxy clusters, obtained in slightly different ways, as explained in the relative sections. They are more extensively discussed by Meneghetti et al. (2017) [63].
I performed simulations with *SkyLens* in order to obtain mock observations of background galaxies deflected by these clusters in the R_c band of Subaru, so both the filter and the PSF considered were the same of the MACS J1206 simulation in that specific band. The background sources catalog was also the same, but only galaxies located at redshift higher than the cluster redshift were taken into consideration, instead of sources with $z > 0.439$, which is MACS J1206 redshift. Moreover, a poissonian noise was added in these images as well, following the same exact procedure explained in the previous chapter.
A further test I tried to implement was considering the *Intra Cluster Light* in these two clusters, as an approximation. The ICL was simulated using the convergence map as a starting point, since it traces the projected mass of the cluster, multiplying it by a constant factor, which is the equivalent of considering a constant M/L, or, to be more precise in this case, L/M, since the goal is basically to translate a mass map into a photon count. This method assumes that the ICL is given basically only by stars that are no longer bound to their original galaxy because of interactions with the BCG or other galaxies in such a way that their location follows exactly the mass distribution of the galaxy cluster, in accordance with the fact that they are not gravitationally bound to a galaxy potential, but rather to the whole cluster potential.
The ICL obtained this way was then summed pixel by pixel to the simulated images, similarly to the addition of the poissonian noise.
The whole KSB weak lensing and mass estimate analysis has been applied to both clusters.

4.2.1 Ares

Ares was obtained thanks to the semi-analytic code: MOKA (Giocoli et al. [64]). It combines analytic models of dark matter halo profiles (e.g. Navarro-Frank-White 1.62) with state of the art N-body and hydrodynamical simulations, it also adds realistic components, such as sub-halos,

stellar components and the *BCG* (Brightest Central Galaxy). The cosmological parameters considered in the simulation are $H_0 = 70\frac{km}{s\ Mpc}$ and $\Omega_{0,M} = 0.3$. This cluster is the combination of two large scale mass distributions at $z = 0.5$, there is an angle of 21 deg between the two clumps, which have masses of $M_1 = 1.32 \times 10^{15} h^{-1} M_\odot$ and $M_2 = 8.8 \times 10^{14} h^{-1} M_\odot$.

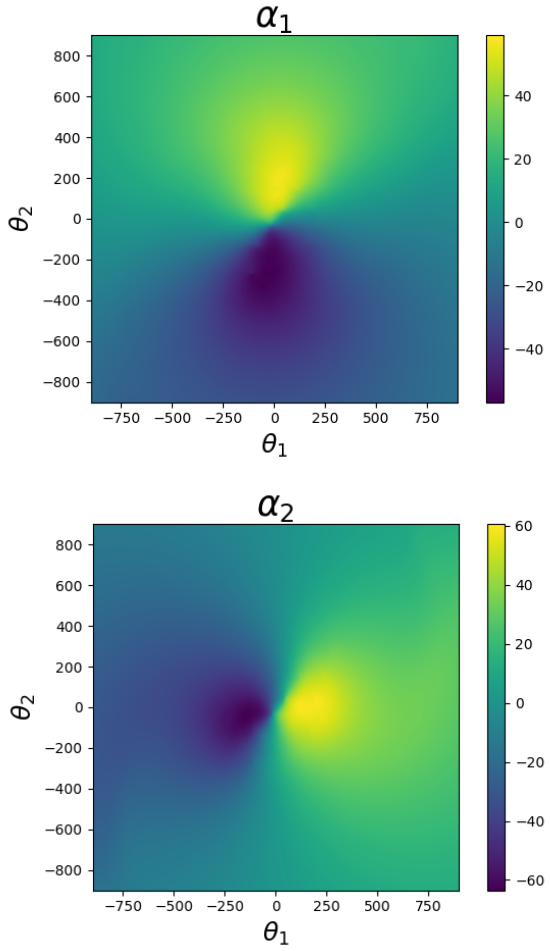

Figure 4.3: Two components of the deflection angle of Ares. The colorbar indicate the angle values in arc-seconds

The modeling of Ares is not trivial, because of the fact that it is composed by two different mass distributions. This makes it difficult to locate single values of both the cluster center and the Einstein radius. In fact, for $z_s = 2$, the critical lines split in two and each mass distribution is surrounded by its own critical line, as shown in Figure 4.5. These two critical ares yield two Einstein radii of $\theta_{E1} = 21.9''$ and $\theta_{E2} = 7.3''$ respectively. I tried to concentrate on the most massive distribution, i.e. the one with the biggest critical line, for both the identification of the

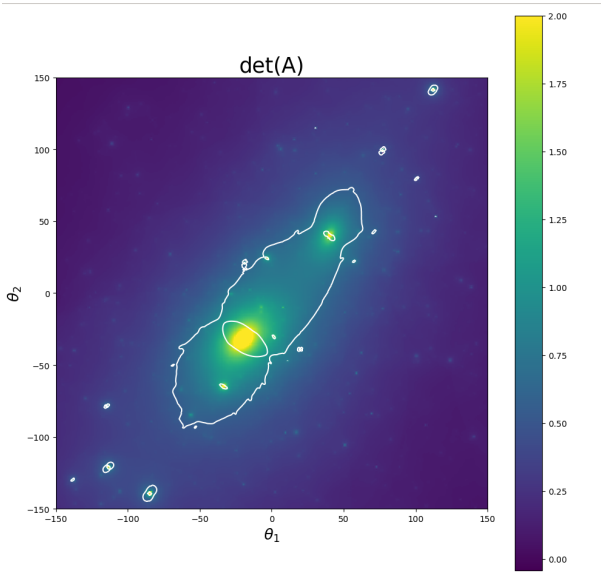

Figure 4.4: Lensing Jacobian maps of Ares. The white lines are the zero level contours of the Jacobian, i.e. the critical lines, for $z_s = 9$

cluster center and the estimate of its Einstein radius. The result is shown in Figure 4.6.

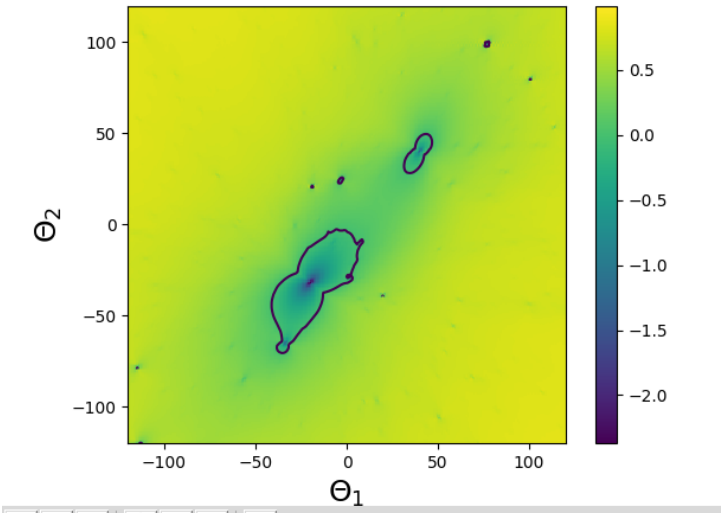

Figure 4.5: Map of $1 - K - \gamma$ for $z_s = 2$, with the tangential critical lines surrounding the two mass distributions

The best fit gives a $\chi^2_R \sim 1.9$ and these parameters yield a cluster mass of $M = 3.45^{+0.77}_{-0.75} \times 10^{15} M_\odot$ for Ares, which is compatible with the sum of the two mass distributions of $M = 3.14 \times 10^{15} M_\odot$.
However, there is obviously a problem moving towards the central part of the cluster. In fact, the second shear value does not seem to follow the

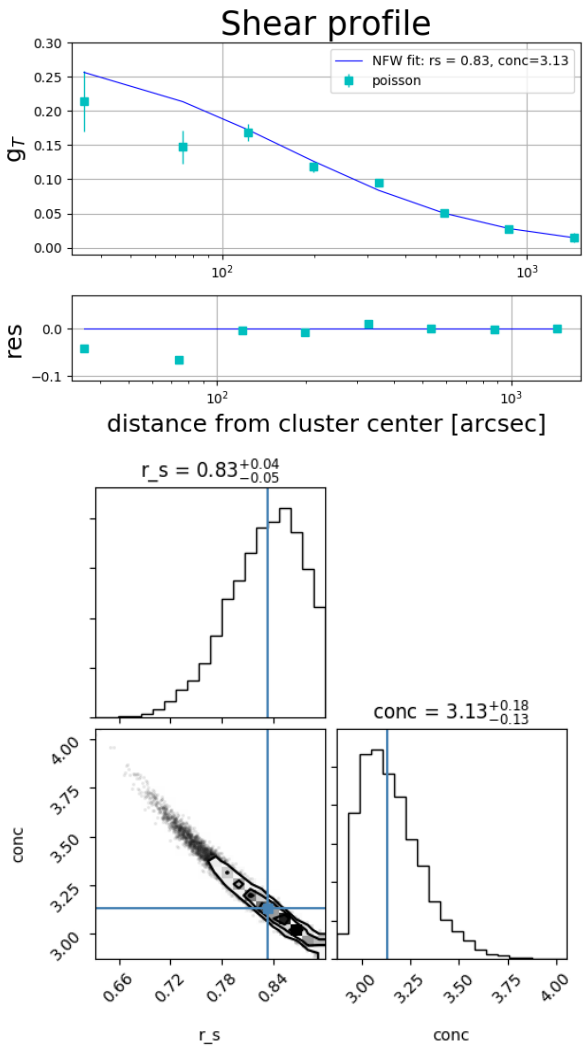

Figure 4.6: First panel: tangential shear profile obtained from KSB analysis of a simulated image with Ares as a deflector. Second panel: NFW parameters obtained from fitting the shear profile

typical trend suggested by the other data points, as the shear measure in the second radial bin is significantly lower respect to the NFW model. Let's try to understand what it is happening: the weak lensing fitting condition wants to fit a NFW profile with the given data points, while the strong lensing condition wants to fit a NFW profile of a single mass distribution with $\theta_E = 21.9''$, which is the more massive distribution. However, the shear signal derives from the analysis of the galaxies ellipticity, which is not only influenced by this single main mass distribution, there is also the smaller one, which causes the second main critical line with $\theta_E = 7.3''$ in Figure 4.5. Its presence causes an additional distortion, which ends up diluting the shear signal measured considering only the most massive

component. The peak of the two components are separated by $\sim 93''$, a value contained in the second radial bin (Figure 4.6). This aspect is also suggested by Figure 4.7, where it is clear also to the naked eye that the tangential orientation of galaxies distortions does not surround only the main mass component.

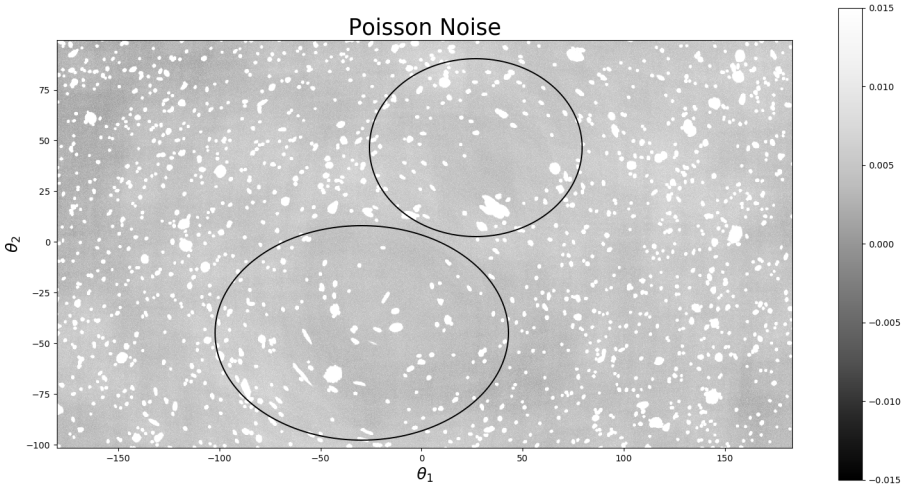

Figure 4.7: Central region of the mock observation with Ares as a deflector. The black circles are intended as a guide to evidence the orientation of the galaxies ellipticities. They follow a tangential distortion around the center of the mass component. In particular, it is clear that galaxies in upper right part of the image have a different distortion from the ones in the lower left part

It is not much different than considering also foreground sources in the ellipticity analysis, it dilutes the signal, but in this case the average is not being performed over a random set of ellipticity values, but to a set of sources with ellipticities distorted according to a second mass distribution. This fact makes it more difficult to estimate the mass of Ares especially in its central part and, in general, of a galaxy cluster with a clear bimodal mass distribution. This effect is expected to becomes less significant moving away from the cluster center, where the total gravitational field of the two mass distributions tends to the field of a single distribution with mass equal to the sum of the two components and ideally acts as a single mass field at infinite distance, which explains the fact that the mass obtained from this type of analysis is still compatible with the true mass of the cluster.

4.2.2 Hera

Hera is obtained directly from high-resolution N-body simulations of a dark matter halo, it was identified in a low resolution Λ_{CDM} simulation box of side 1 h^{-1} Gpc, with $\Omega_{0,M} = 0.24$, $\Omega_{0,B} = 0.04$ and $H_0 = 72\frac{km}{s\ Mpc}$. Its virial region is described by 10 million particles, its total mass is $M = 9.4 \times 10^{14} h^{-1} M_\odot$. It is located at $z = 0.507$.

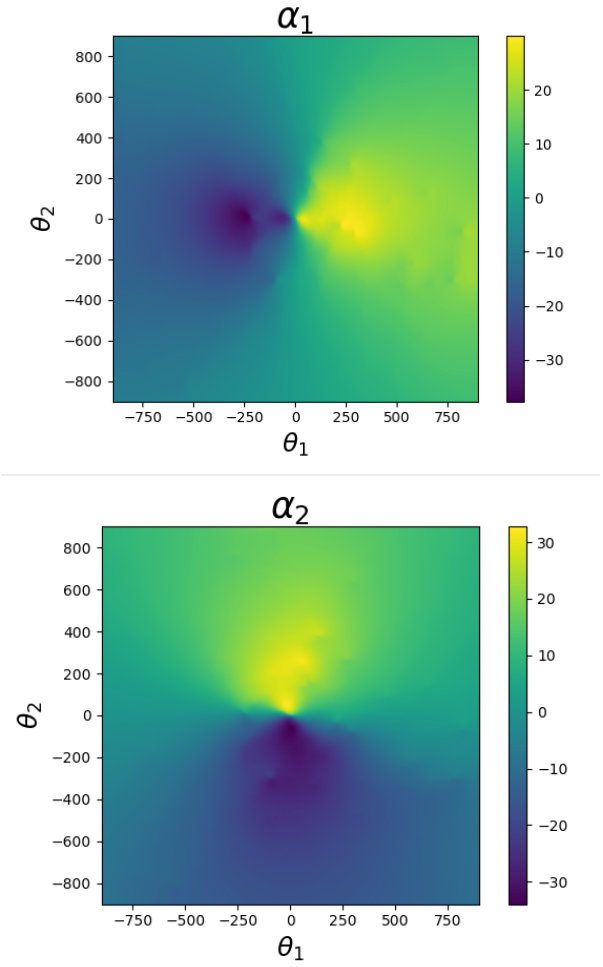

Figure 4.8: Two components of the deflection angle of Hera. The colorbar indicate the angle values in arc-seconds

The Einstein radius was calculated by means of the critical area, obtaining a value of $\theta_E = 15.0''$.

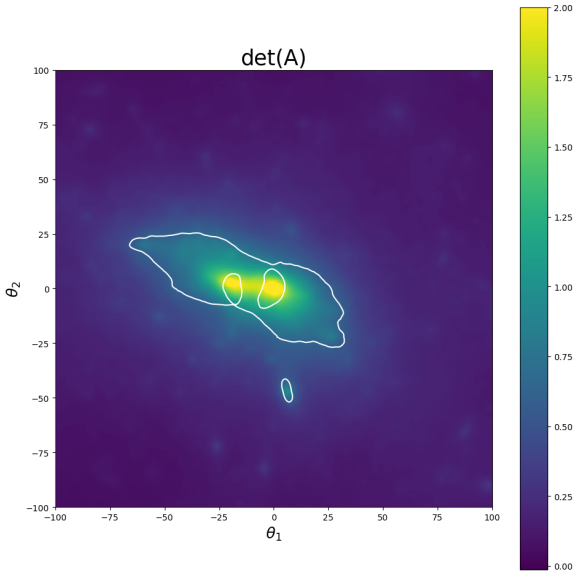

Figure 4.9: Lensing Jacobian map of Hera. The white line is the zero level contour of the Jacobian, i.e. the critical line, for $z_s = 9$

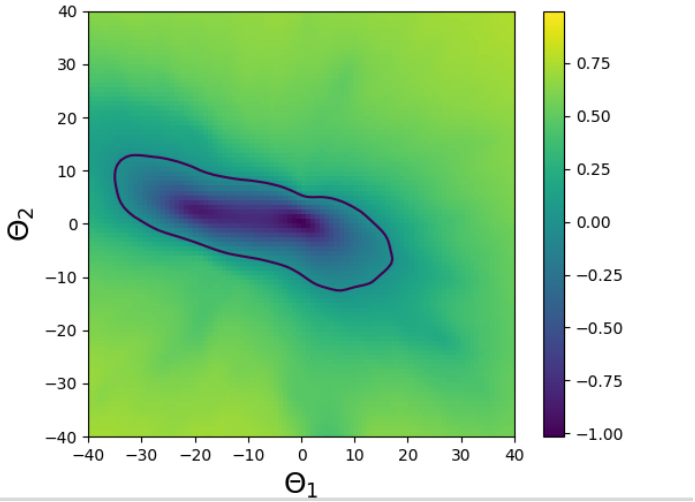

Figure 4.10: First panel: map of $1-K-\gamma$ for $z_s = 2$, with the tangential critical line

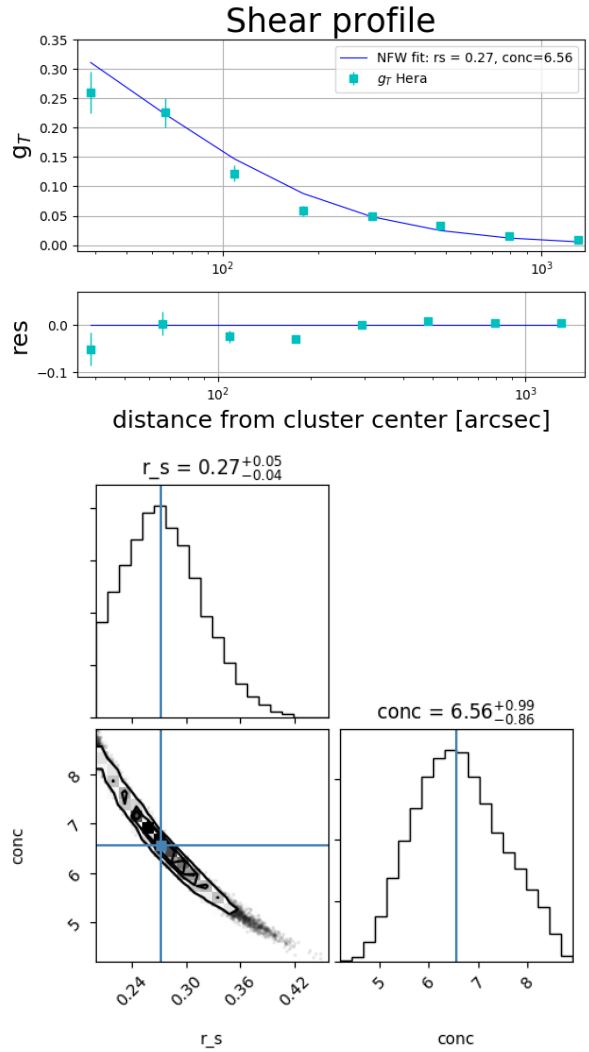

Figure 4.11: First panel: tangential shear profile obtained from KSB analysis of a simulated image using Hera as a deflector. Second panel: NFW parameters obtained from fitting the shear profile

The best fits gives a $\chi^2_R \sim 2.7$.

As in the case of Ares, Hera presents a bimodal mass distribution as well, as it is clear from its convergence map (Figure 4.12), but in this case the two distributions are much closer to each other ($\sim 23''$) respect to Ares. This distance is included in the first radial bin and could explain why that shear measurement is slightly smaller than the best fit NFW shear profile.

These values yield a mass of $M = 1.16^{+0.89}_{-0.63} \times 10^{15} M_\odot$ for Hera, which is compatible with its real mass of $M = 1.34 \times 10^{15} M_\odot$.

4.2.3 ICL

This section regards the results achieved analyzing the simulations obtained using Ares and Hera as deflectors with the addition of the Intra-Cluster light. As previously explained, the ICL has been simulated by means of the convergence maps, that are shown in Figure 4.12.

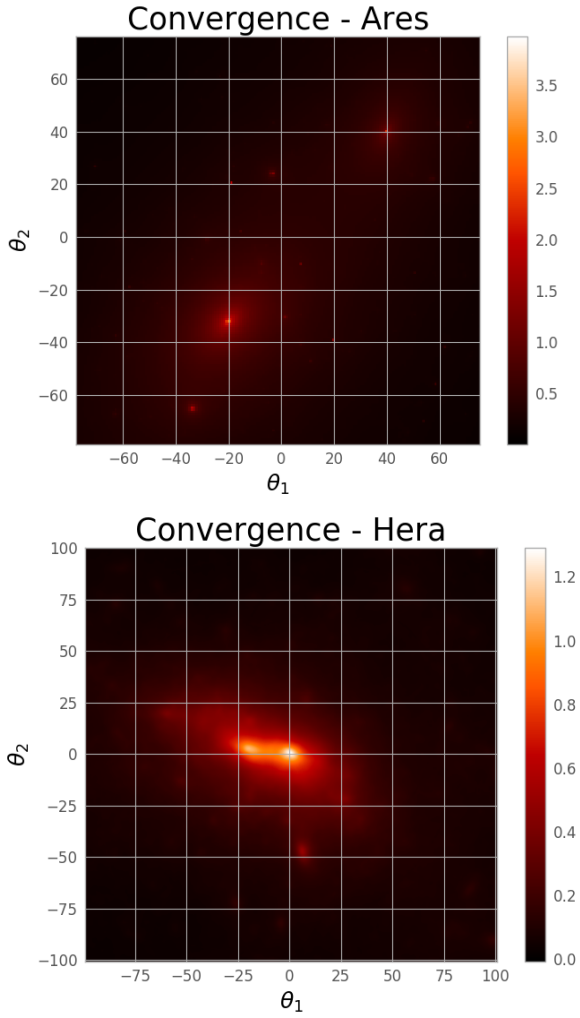

Figure 4.12: Convergence maps for $z_s = 2$ of Ares (first panel) and Hera (second panel)

The convergence maps have been multiplied by a factor of 0.005 and the result has been added to the mock observation. The outcome is shown in Figure 4.13.

The resulting shear profiles and mass estimates of these clusters are shown in Figure 4.14 and reported in Table 4.2.

The results are basically the same of the case without ICL: the analysis works fine for Hera, whose mass value is compatible with both the mass

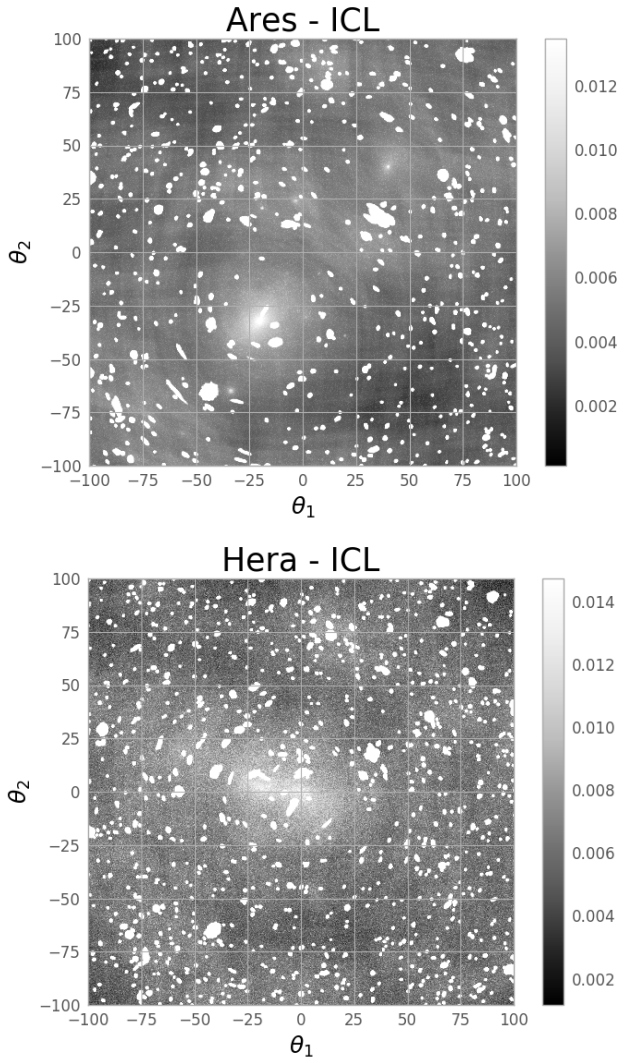

Figure 4.13: Mock observations using Ares (first panel) and Hera (second panel) as deflectors, with the addition of a simulated ICL. The colorbar indicates the photon count per second

obtained without the simulated ICL and its real value. In the case of Ares the compatibility between mass values is again positive, but the bimodality in its mass map spoils the KSB analysis in the second radial bin. The conclusion is that the simulated ICL is not a prevalent component in this work and does not affect this method of clusters mass estimate.

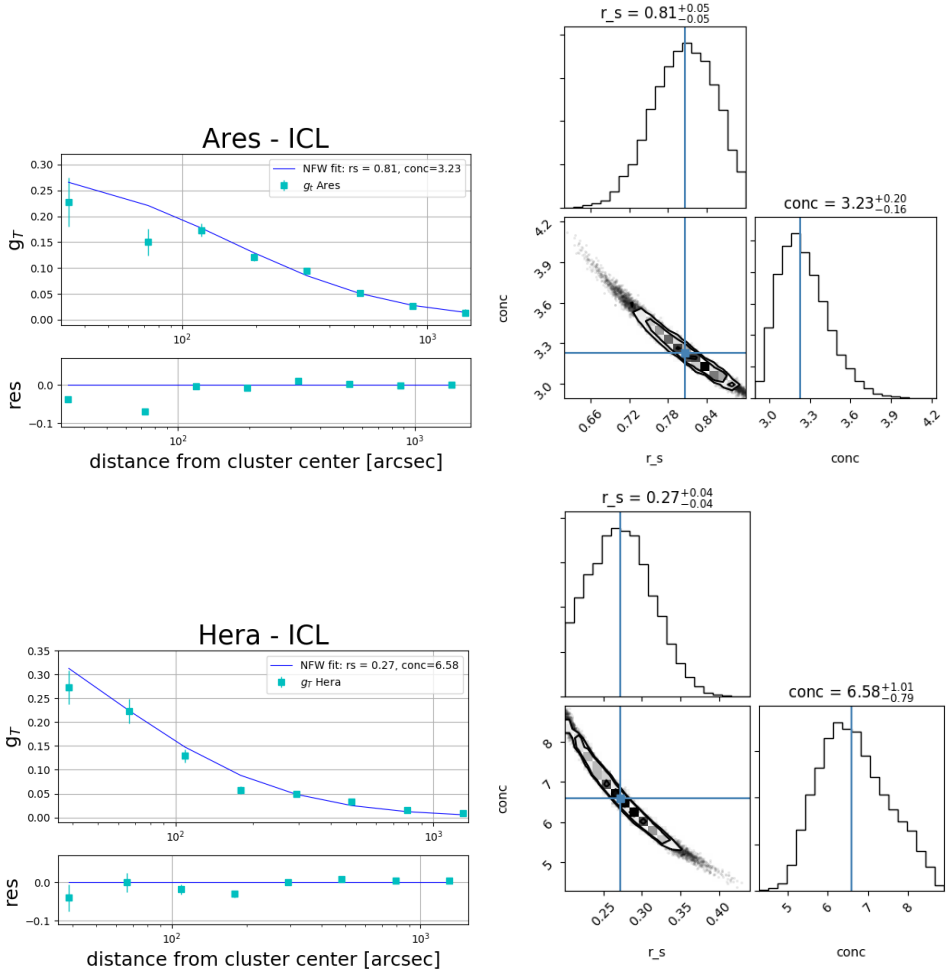

Figure 4.14: Shear profiles with a NFW fit and respective parameters scale radius r_s and concentration c

Cluster	**Mass** $[\frac{M_\odot}{10^{15}}]$	χ^2_R
Ares	$3.44^{+1.04}_{-0.71}$	1.8
Hera	$1.17^{+0.78}_{-0.62}$	2.6

Table 4.2: Mass values of Ares and Hera obtained from the analysis of simulations containing the intra-cluster light

Chapter 5

Conclusions

Gravitational lensing is one of the best ways to infer galaxy clusters total mass, considering the fact that light is bent by gravity, which does not distinguish baryonic and dark matter. Measuring different clusters masses at different redshifts allows to build a mass function and understand the evolution of these type of structures, which is crucial in order to put constrains on cosmological parameters and deduce our universe composition and evolution history.
One way to do it, is considering the distortion of the shapes of distant galaxies lensed by the galaxy cluster at issue. These galaxies are located far enough from the cluster center on the sky plane to be in a weak lensing regime, so they are not characterized by large gravitational arcs or multiple images, but their ellipticity is rather weakly distorted. The goal of this thesis was using this weak lensing effect in order to obtain the mass of the deflecting cluster.
In order to do this, I exploited the KSB method, which allows to estimate the shear contribution only due to the gravitational presence of the deflector on each galaxy, taking into consideration both seeing and instrumental effects. A statistical analysis on a large number of sources allows to compare this contribution to a given model and finally estimate the cluster mass.
I worked on mock images created with *SkyLens*, a code which allows to simulate observations with a variety of telescopes in different configurations. I concentrated on simulations performed using the galaxy cluster MACS J1206 as a deflector, particularly in the R_C band. This cluster has been extensively observed as part of the CLASH program and

robust models have already been produced, which allowed me to obtain its deflection angle maps with the software *LensTool*. I produced three types of images, according to different types of noise: in the first case, simulated galaxies were inserted into real observations of MACS J1206, in the second case I added a Poissonian noise with the same expected value of the photon count value in empty regions of the real observations; in the third case the noise is added directly by SkyLens.

The mock galaxies were detected and analyzed with *Sextractor* and their ellipticity was calculated from the surface brightness quadrupole moment of each source. The KSB method was applied in order to obtain the shear distortion only due to the deflector. This shear signal was rescaled for each galaxy to $z_s = 2$, the same considered to build the LensTool model, which allowed the comparison between the model and shear profiles obtained from the images. The analysis with real and simulated galaxies and poissonian noise are the ones that reproduce the model better (reduced χ^2 values of 0.79 and 0.74 respectively, against a value of 2.53 for the image with noise added directly by SkyLens), because the noise added by SkyLens suppresses the outer parts of the galaxies, causing an underestimation of the ellipticity of each source, which translates in a lower shear value.

The shear profiles have been fitted with profiles produced by a Navarro Frenk White (NFW) mass distribution, with the addition of a second condition on the total residual to minimize, which considers the cluster Einstein radius obtained from the area inside the main critical line. This allowed to obtain the best fit parameters scale radius r_s and concentration c that describe the mass density profile. The mass of the cluster is then inferred simply integrating the density profile. Mass values of MACS J1206 are compatible with other literature works.

Moreover, the same type of analysis has also been applied to simulations of observations using MACS J1206 as a deflector in the I_C and Z Subaru filters and also two simulated clusters: Ares and Hera, in the R_C Subaru band.

In the first case, the masses are compatible with values obtained from the analysis in the R_C band, but the filter Z estimate tends to underestimate the shear signal because it is the image with the lowest exposure time, i.e. the lowest signal to noise ratio, which makes it more difficult to estimate

the sources ellipticities and shear.
As for the simulated clusters, in the case of Hera, the analysis works well and the mass estimate is compatible with its real mass. Although the same can be stated for Ares, its modelling is not trivial because of its bimodal mass distribution, which causes a drop in the shear value obtained averaging values of galaxies mainly distorted by the secondary mass distribution. These clusters were also studied with the addition of a simulated Intra Cluster Light, which follows the projected cluster mass distribution. The conclusions are basically the same of the previous analysis, which means that, in this case, the ICL does not impact significantly the measurement of the shear.

Bibliography

[1] "Die Feldgleichungen der Gravitation", A. Einstein (1915), Preussische Akademie der Wissenschaften, Sitzungsberichte, 1915 (part 2), 844–847

[2] "On the Foundation of Relativistic Cosmology", H.P. Robertson (1929), Proc. Natl. Acad. Sci. USA, 1929 Nov 15; 15(11): 822–829

[3] "A Relation Between Distance and Radial Velocity Among Extra-Galactic Nebulae", E. Hubble (1929), M. Wilson Observatory, Carnegie Institution of Washington

[4] "The High-Z Supernova Search: Measuring Cosmic Deceleration and Global Curvature of the Universe Using Type Ia Supernovae", B.P. Schmidt et al. (1998), The Astrophysical Journal, 507: 46-63, 1998 November 1

[5] "Über die Krümmung des Raumes", A. Friedmann (1922), Zeitschrift für Physik, December 1922, Volume 10, Issue 1, pp 377–386

[6] "Inflationary universe: A possible solution to the horizon and flatness problems", A.H. Guth (1981), Phys. Rev. D 23, 347

[7] "Cosmology: the Origin and Evolution of Cosmic Structure"; P.Coles, F. Lucchin; Wiley (2002); Baffins Lane, Chichester, West Sussex PO19 1UD, England

[8] "The Stability of a Spherical Nebula", J.H. Jeans (1902), Philosophical Transactions of the Royal Society A. 199: 1–53

[9] "Die Rotverschiebung von extragalaktischen Nebeln", F. Zwicky (1933), Helv. Phys. Acts 6 110–127

[10] "Dark matter and cosmic structure", C.S. Frenk, S.D.M. White (2012), Annalen der Physik, October 1, 2012

[11] "Formation of Galaxy Clusters", V. Kravtsov, S. Borgani (2012); arXiv:1205.5556v1

[12] "The mass function on an X-ray flux-limited sample of galaxy cluster", T.Reiprich, H.Bohringer (2002), ApJ, 567, 716

[13] "The Distribution of Rich Clusters of Galaxies", Gorge O. Abell (1958), 1958 ApJS, 3, 21IA

[14] "Cosmology with clusters of galaxies", S.Borgani (2006), arXiv:astro-ph/0605575v1

[15] W.Press, P. Schechter (1974); ApJ, 187, 425

[16] Zwicky, F. 1951, PASP, 63, 61

[17] "On The Distribution of Mass and Luminosity in Elliptical Galaxies", G. de Vaucouleurs (1953), MNRAS.113.134

[18] "Intracluster light in clusters of galaxies at redshifts 0.4 ¡ z ¡ 0.8", L. Guennou et al., Astronomy and Astrophysics 537, A64 (2012)

[19] "Intra Cluster Light properties in the CLASH-VLT cluster MACSJ1206.2-0847", V.Presotto et al. (2014); arXiv:1403.4979v1 [astro-ph.CO] 19 Mar 2014

[20] "The Observation of Relic Radiation as a Test of the Nature of X-Ray radiation from the Clusters of Galaxies", R.A. Sunyaev, Y.B. Zeldovich (1972); Institute of applied Mathematics, Moscow

[21] "Cosmology with the Sunyaev-Zel'dovich effect", John E. Carlstrom, Gilbert P. Holder, Erik D. Reese (2002); Annu. Rev. Astron. Astrophys. 2002. 40:643–80

[22] "Lens-like Action of a Star by the Deviation of Light in the Gravitational Field", A. Einstein (1936), Science. 84 (2188): 506–7

[23] "Introduction to Gravitational Lensing, with Python Examples", M. Meneghetti (2017)

[24] "Opticks, or, a Treatise of the Reflections, Refractions, Inflections and Colours of Light", I. Newton (1704), Royal Society

[25] "On the Deflection of a Light Ray from its Rectilinear Motion", J.G. von Soldner (1801), Berliner Astronomisches Jahrbuch, 1804, pp. 161-172

[26] "A determination of the deflection of light by the sun's gravitational field, from observations made at the total eclipse of May 29, 1919", F.W. Dyson, A.S. Eddington and C. Davidson (1919), The Royal Society Publishing, 1 January 1920 Volume 220 Issue 571-581

[27] "Weak gravitational lensing", M.Bartelmann, P.Schneider (2001); Phys.Rep.340

[28] "Finite Source Effects in Microlensing: a precise, easy to implement, fast and numerical stable formalism"; C.H. Lee, A. Riffeser, S.Seitz, R. Bender (2009), arXiv:0901.1216v2 [astro-ph.GA] 1 Apr 2009

[29] "Microlensing Parallax for Observers in Heliocentric Motion", S. Calchi Novati, G. Scarpetta (2016); The Astrophysical Journal,824:109(15pp), 2016 June 20

[30] "Velocity Dispersions and Mass-to-Light Ratios for Elliptical Galaxies", S.M. Faber, R.E. Jackson (1976); the AstrophysicalJournal, 204; 668-683, 1976 March 15

[31] "CLASH-VLT: A Highly Precise Strong Lensing Model of the Galaxy Cluster RXC J2248.7-4431 (Abell S1063) and Prospects for Cosmography", G.B. Caminha et al. (2016), arXiv:1512.04555v1 [astro-ph.CO] 14 Dec 2015

[32] "The Sloan Digital Sky Survey: Technical Summary", D.G. York et al. (2000), arXiv:astro-ph/0006396v1 27 Jun 2000

[33] "The Sloan Lens ACS Survey", Adam S. Bolton, sdss2008.uchicago.edu/depot/bolton_a.pdf

[34] "The Cluster Lensing and Supernova Survey with Hubble: An Overview", M.Postman et al. (2012), arXiv:1106.3328v3 [astro-ph.CO] 3 Jan 2012

[35] "MACS: A quest for the most massive galaxy clusters in the universe", H. Ebeling, A.C. Edge, J.P. Henry (2001), arXiv:astro-ph/0009101v2 25 Apr 2001

[36] "The Cosmic Lens All-Sky Survey: I. Source selection and observations", S.T. Myers et al. (2002), arXiv:astro-ph/0211073v1 5 Nov 2002

[37] "Lens Models and Magnification Maps of the Six Hubble Frontier Fields Clusters", Traci L. Johnson et al. (2014), The Astrophysical Journal, 797:48 (31pp), 2014 December 10

[38] "A Universal Density Profile from Hierarchical Clustering", Julio F. Navarro, Carlos S. Frenk, Simon D.M. White (1996); arXiv:astro-ph/9611107v4 21 Oct 1997

[39] "Realistic simulations of gravitational lensing by galaxy clusters: extracting arc parameters from mock DUNE images", M. Meneghetti, P. Melchior, A. Grazian, G. De Lucia, K. Dolag, M. Bartelmann, C. Heymans, L. Moscardini, and M.Radovich; AeA 482, 403–418 (2008)

[40] "Image simulations for gravitational lensing with SkyLens", A. A. Plazas, M. Meneghetti, M. Maturi, J. Rhodes (2018); arXiv:1805.05481v2 [astro-ph.CO] 20 Oct 2018

[41] "The Euclid mission design", G.D. Racca et al. (2016), arXiv:1610.05508v1 [astro-ph.IM]

[42] "UVUDF: Ultraviolet Through Near-Infrared Catalog and Photometric Redshifts of Galaxies in the Hubble Ultra Deep Field", Marc Rafelski et al. (2015); arXiv:1505.01160v1 [astro-ph.CO] 5 May 2015

[43] "The HST Extreme Deep Field (XDF): Combining all ACS and WFC3/IR data on the HUDF region into the Deepest Field Ever", G.D. Illingworth et al. (2013), The Astrophysical Journal Supplement Series, 209:6 (13pp), 2013 November

[44] "Lensing and x-ray mass estimates of clusters (simulations)", E. Rasia et al. (2012), New J. Phys.14 055018

[45] "A Method for Weak Lensing Observations", Nick Kaiser, Gordon Squires, Tom Broadhurst (1994); arXiv:astro-ph/9411005v1 1 Nov 1994

[46] "A weak lensing analysis of the PLCK G100.2-30.4 cluster", M. Radovich, I. Formicola, M. Meneghetti, I. Bartalucci, H. Bourdin, P. Mazzotta, L. Moscardini, S. Ettori, M. Arnaud, G. W. Pratt, N. Aghanim, H. Dahle, M. Douspis, E. Pointecouteau, A. Grado (2015); AeA 579, A7 (2015)

[47] "Detection of weak lensing by a cluster of galaxies at z=0.83", G. A. Luppino and Nick Kaiser (1997)

[48] "Weak Lensing Analysis of Cl 1358+62 Using Hubble Space Telescope Observations", Henk Hoekstra, Marijin Franx, Konrad Kuijken, Gordon Squires (1998), THE ASTROPHYSICAL JOURNAL, 504 : 636-660, 1998 September 10

[49] "A weak lensing analysis of the Abell 383 cluster", Zhuoyi Huang, Mario Radovich, Aniello Grado, Emanuella Puddu, Anna Romano, Luca Limatola and Liping Fu (2011); arXiv:1102.1837v1

[50] "Selecting background galaxies in weak-lensing analysis of galaxy clusters", I. Formicola, M. Radovich, M. Meneghetti, P. Mazzotta, A. Grado and C. Giocoli (2014); MNRAS 458, 2776–2792 (2016)

[51] "Atlas de galaxias australes", J.L. Sersic (1968), Observatorio Astronomico, Cordoba (Argentina)

[52] "Multiscale cluster lens mass mapping - I. Strong lensing modelling", E. Jullo and J.P. Kneib (2009), Mon. Not. R. Astron. Soc.395,1319–1332 (2009)

[53] "Mass distribution in the core of MACS J1206 - Robust modeling from an exceptionally large sample of central multiple images", G.B. Carminha et al. (2017), arXiv:1707.00690v2 [astro-ph.GA] 4 Oct 2017

[54] "NewFeatures of SAOImage DS9", W.A. Joye and E. Mandel (2003); Astronomical Data Analysis Software and Systems XII ASP Conference Series, Vol. 295, 2003

[55] "SExtractor v2.13 User's manual", E.Bertin, Institut d'Astrophysique and Observatoire de Paris

[56] "Gravitational Lensing by NFW Halos", C.O. Wright and T.G. Brainerd, The Astrophysical Journal, 534 : 34-40, 2000 May 1

[57] "CLASH: Mass Distribution in and around MACS J1206.2-0847 From a Full Cluster Lensing Analysis", K. Umetsu et al. (2012), arXiv:1204.3630v2 [astro-ph.CO] 6 Jun 2012

[58] "A Simplex Method for Function Minimization", J.A. Nelder, R. Mead (1965), The Computer Journal, Volume 7, Issue 4, January 1965, Pages 308–313

[59] " Practical Markov Chain Monte Carlo", Charles J. Geyer (1992), Statistical Science, Vol. 7, No. 4 (Nov., 1992), pp. 473-483, Institute of Mathematical Statistics

[60] "emcee: The MCMC Hammer", D. Foreman-Mackey et al. (2013); arXiv:1202.3665v4 [astro-ph.IM] 25 Nov 2013

[61] "The Universal Einstein Radius Distribution from 10,000 SDSS Clusters", A. Zitrin et al. (2012); arXiv:1105.2295v2 [astro-ph.CO] 2 Apr 2012

[62] "A pratical guide to Data Analysis for Physical Science Students", L.Lyons, Cambridge University Press (1991)

[63] "The Frontier Fields lens modelling comparison project", M. Meneghetti et al. (2017); MNRAS 472, 3177–3216 (2017)

[64] "MOKA: a new tool for Strong Lensing Studies", Carlo Giocoli, Massimo Meneghetti, Matthias Bartelmann, Lauro Moscardini, Michele Boldrin (2011); arXiv:1109.0285v2 [astro-ph.CO] 16 Jan 2012